Fission Track Thermochronology: Thermal Characteristics of Fission Tracks in Zircon, and Cooling History Analysis of the Granitic Bodies around the Northern Alps, Central Japan

15th December 1996

Ryuji YAMADA

Acknowledgment

I wish to greatly acknowledge my supervisors, Emer. Prof. Susumu Nishimura and Dr. Takahiro Tagami, for their continuous encouragement and advice throughout this study. Drs. Masayuki Torii and Yoshitsugu Furukawa are acknowledged for providing a good environment for the research. I am grateful to the members of geochronology research group of Kyoto University, Dr. Noriko Hasebe, Dr. Masahumi Sudo, Tohru Nishiyama, Chica Inoue (Shimada), Keiko Sato, Tetsu Yoshioka, Atsushi Yamagiwa and Hisayo Tauchi. Many advises on the research and experiments were given by Tomoaki Sumii and Dr. Hisatoshi Ito, my reliable seniors. Thanks are due to; Dr. Satoru Harayama for valuable comments on Part III; Tohru Danhara and Hideki Iwano for suggestions on fission track experiments.

Finally, I sincerely thank my family for all their support, hoping the recovery of father's health.

CONTENTS

Outline of the Study

Thermochronology Using Fission Track Method

Thermochronologic studies using radiometric dating methods have been developed to reveal the various geological process in crust by reproducing thermal history of rock samples (e.g., Wagner et al., 1977; Harrison et al., 1979). The principle is based on the fact that the various systems start to retain their radiometric daughter products lower than their specific temperature, called closure temperature (Dodson, 1973). Of the radiometric dating techniques, fission track (FT) method has a remarkable feature that the track, which correspond to the daughter product of a radioactive parent atom, is observable under microscopes by means of chemical etching technique. FTs are gradually faded by heating after formation, and the resultant loss of FT resets the apparent FT ages. The partially faded tracks are observable and thus the length distribution of FTs offers a sensitive geological thermochronometry. Presently, FT method has been developed into a unique thermo–tectonic tool for reconstructing the temperature–time–paths of rocks in the low temperature region below 300°C, in particular by the introduction of track length analysis (e.g., Gleadow et al., 1983; Green et al., 1989a). FT analysis has been successfully applied to many of the world's young orogenic belts, such as the Himalaya of northern Pakistan (Zeitler, 1985), the European Alps (Hurford, 1986), the Transantarctic Mountains (Gleadow and Fitzgerald, 1987), and the New Zealand Alps (Kamp and Tippett, 1993).

The knowledge of the conditions under which FTs are stable or begin to fade, forms the vital base for the geological interpretation of FT ages. FT fading is referred as *annealing*, in terms of effect of both temperature and time on the track stability. The FT annealing of apatite and zircon, which are common mineral for FT method, are sensitive for the temperature range of ~ 100°C and ~ 250°C, respectively. The quantitative model for annealing kinetics of apatite has been developed on the basis of laboratory experiments and geological data (e.g., Laslett et al., 1987; Carlson, 1990; Crowley et al., 1991), and a detailed system of thermochronology has developed based on FT analysis of apatite (e.g., Gleadow et al., 1983; Green et al., 1989ab). Recently, modeling procedures have been developed for quantifying the thermal histories using apatite annealing kinetic models (e.g., Green et al., 1989b; Corrigan, 1991; Lutz and Omar, 1991; Gallagher, 1995). However, it has not been possible to develop a comparable system based on FT analysis of zircon, largely due to the lack of basic documentation of the procedures required to obtain reliable track length data.

This paper consist of a series of studies for establishing the basis of FT thermochronology system using zircon, and demonstrating the unique applicability to detailed

reconstruction of an orogenic history. In the Part I, I present a contribution to better understand the FT etching and annealing behavior of zircon. The carefully designed works described in this paper provide the important foundation. In the Part II, I establish a quantitative model for the annealing kinetics of FTs in zircon, under the experimental conditions proposed in the Part I. It should extent the field for the application of FT thermochronology system, such as a quantitative modeling of thermal histories in orogenic belts at a depth of ~ 10 km, because zircon FT system can provide unique information on the deeper crustal level than apatite FT system. In the Part III, FT thermochronology using mainly zircon is applied to the Northern Alps, Central Japan, in order to reveal its orogenic history. The timing of uplifting, uplift amount and rate can be quantitatively assessed, based on the information on the estimates of paleotemperature and paleo–geothermal gradient which are provided by the spatial FT age distribution and track length analysis. These estimates and the other geological constraints will reveal the orogenic history of the Northern Alps in detail.

Contribution of This Study

Part I: Confined fission-track length measurement of zircon; assessment of factors affecting the paleotemperature estimate

A series of laboratory annealing experiments were designed and carried out in order to understand the factors affecting observed confined track lengths in thermally annealed zircon. The variation of confined FT lengths according to both experimental and analytical conditions were determined on zircons from Nisatai Dacite. It was found that etching temperature, track etching criteria, measurement criteria of horizontal confined tracks (HCT's) and the orientation of HCT's significantly control the observed track lengths where the samples are highly annealed (i.e., > 600°C for 1 h annealing). The first three factors may be related to the presence of gap zones in an annealed track (Fig. 1), whilst the fourth is caused by anisotropic annealing and etching characteristics (Fig. 2). For reliable thermal history reconstruction, therefore, it should be the minimum requirement to document explicitly the experimental and analytical conditions of these factors in zircon fission-track analysis.

This part is published in the *Chemical Geology* (119, 293–306, Yamada, R., T. Tagami, and S. Nishimura) in 1995. I contributed to the initial experimental design, measurement, analysis, discussion, and manuscript writing. Co-authors made some modification on the discussion and the experimental scheme.

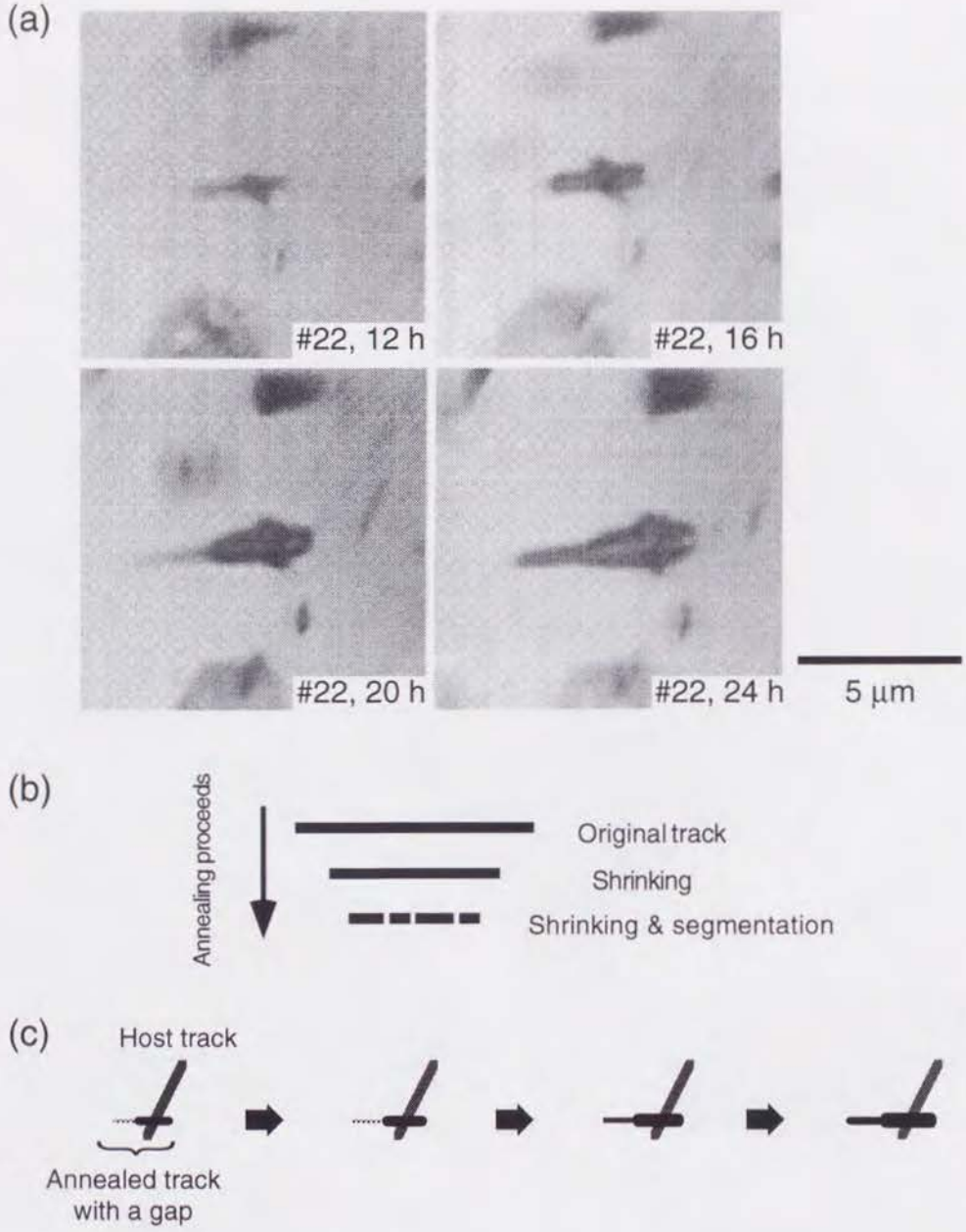

Fig. 1. (a) A set of photographs of a step–etched HCT in a zircon grain annealed at 698°C for 1 h, taken with a Nikon® Biophot microscope using transmitted light (200x dry objective and 10x tube factor). Etching time is indicated at the bottom of each photos. They show a combination of two portions with contrasting diameters, resulting a sudden increase in length.
(b) Schematic diagram of fission–track annealing process in zircon. As annealing proceeds, an original latent track shrinks gradually. Second, the track begins segmentation and gap zones appear along the original track part.
(c) Schematic process of the TINT etching with a relatively great gap. Four steps in this figure correspond to four photographs of (a).

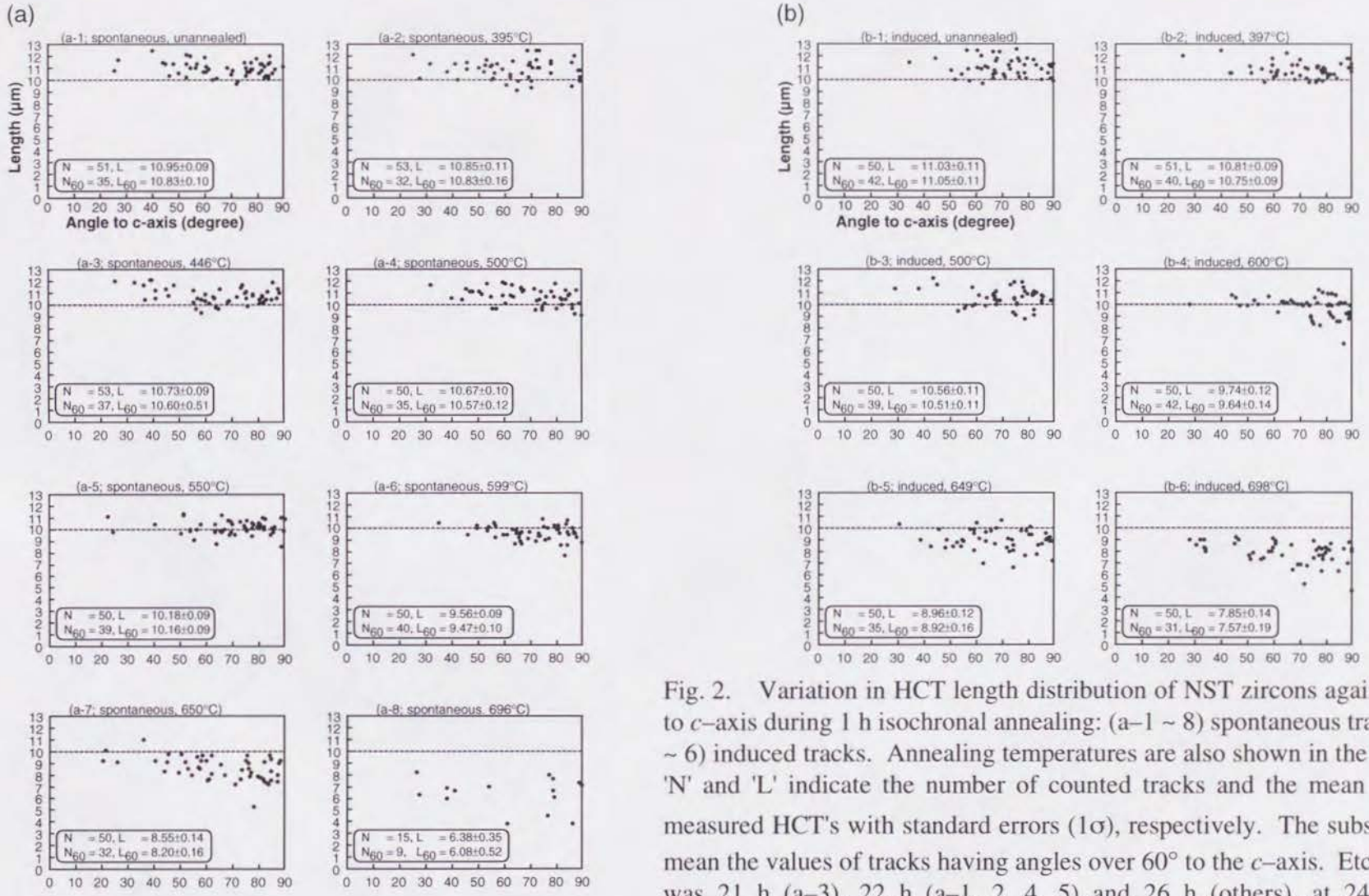

Fig. 2. Variation in HCT length distribution of NST zircons against angles to *c*–axis during 1 h isochronal annealing: (a–1 ~ 8) spontaneous tracks, (b–1 ~ 6) induced tracks. Annealing temperatures are also shown in the headings. 'N' and 'L' indicate the number of counted tracks and the mean length of measured HCT's with standard errors (1σ), respectively. The subscripts '60' mean the values of tracks having angles over 60° to the *c*–axis. Etching time was 21 h (a–3), 22 h (a–1, 2, 4, 5) and 26 h (others), at 248 ± 1°C, respectively. No HCT's were found for both spontaneous and induced samples annealed at 750°C. Note that tracks show highly anisotropic distributions and that tracks with greater angles to *c*–axis are slightly shorter at advanced stages of annealing.

Part II: Annealing kinetics of fission tracks in zircon: an experimental study

29 sets of laboratory annealing experiments of zircon FT has been carried out in heating conditions at 350 - 750°C for 10^{-1} - 10^{3} h (i.e., 4.5 min. - ~40 days), in order to establish a quantitative model for the annealing kinetics of FTs in zircon. Variation in the confined lengths of spontaneous fission tracks was determined using zircon grains from the Nisatai Dacite. The fading contours of normalized mean track length (r) on the Arrhenius diagram showed as sets of straight lines (Fig. 3). Fitting to the experimental results was attempted for some kind of annealing kinetic models, called the parallel and fanning models, in order to describe the decrease in r with increasing temperature or heating time (Fig. 3). The lowest temperature limit of the zircon partial annealing zone (ZPAZ) was defined as $r \sim 0.95$, and the highest as $r \sim 0.4$, which approximately corresponded to the total fading of surface tracks. Extrapolation of the results of the laboratory experiments to geological time scale gives estimated values of the ZPAZ: ~ 210–320°C (± 60°C, 2σ) on the parallel model and ~ 170–390°C (50°C, 2σ) on the fanning model for the heating duration of 10^{7} y. The temperatures of ZPAZ decrease ~20°C for a magnitude of longer annealing duration. Because the estimated closure temperature of zircon fission-track analysis approximately corresponds to the middle of ZPAZ, these results support previously estimated closure temperature of ~ 240°C (e.g., Hurford, 1986). In addition, the relationship between etching rate and normalized mean track length for various annealing experiments revealed that the removal of alpha–radiation damage occurs drastically at $r \sim 0.93$ (Fig. 4).

This part is published in the *Chemical Geology* (122, 249–258, Yamada, R., T. Tagami, S. Nishimura, and H, Ito) in 1995. I contributed to the initial experimental design, measurement, analysis, discussion, and manuscript writing. Co-authors made some modification on the discussion and the experimental scheme.

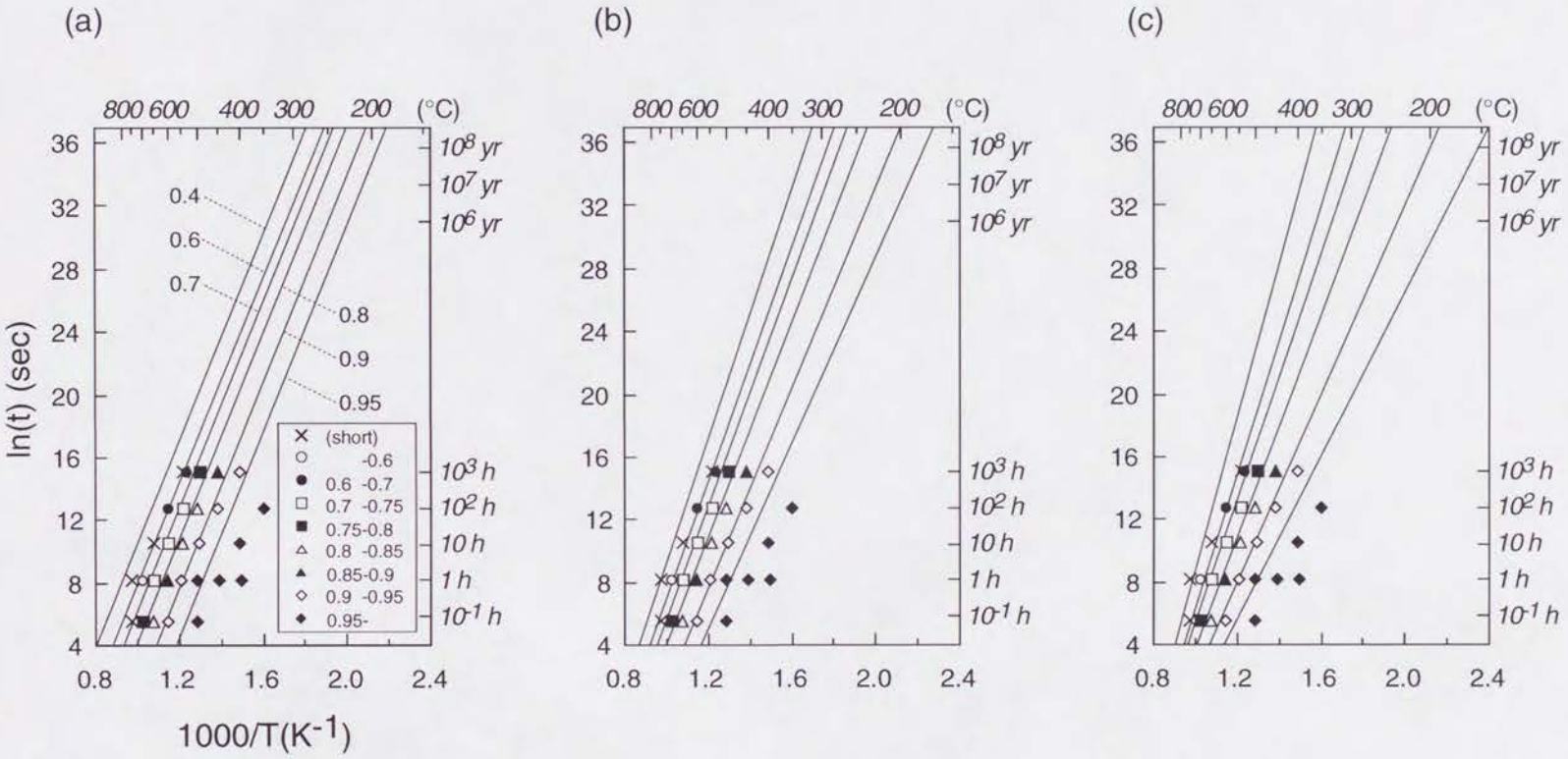

Fig. 3. Arrhenius plots of the experimental data using spontaneous FT, together with fitting lines extrapolated to geological time condition; (a) parallel model, (b) fanning model (critical temperature $T_0 = \infty$), (c) fanning model ($T_0 \neq \infty$). Each point corresponds to one annealing experiment run. Different degrees of length reduction (r) are shown with different symbols. Cross symbols indicate time and temperature conditions where tracks were short so that no horizontal confined tracks could be found. Values of r for each fading contours are indicated in (a), ranging from 0.4 to 0.95.

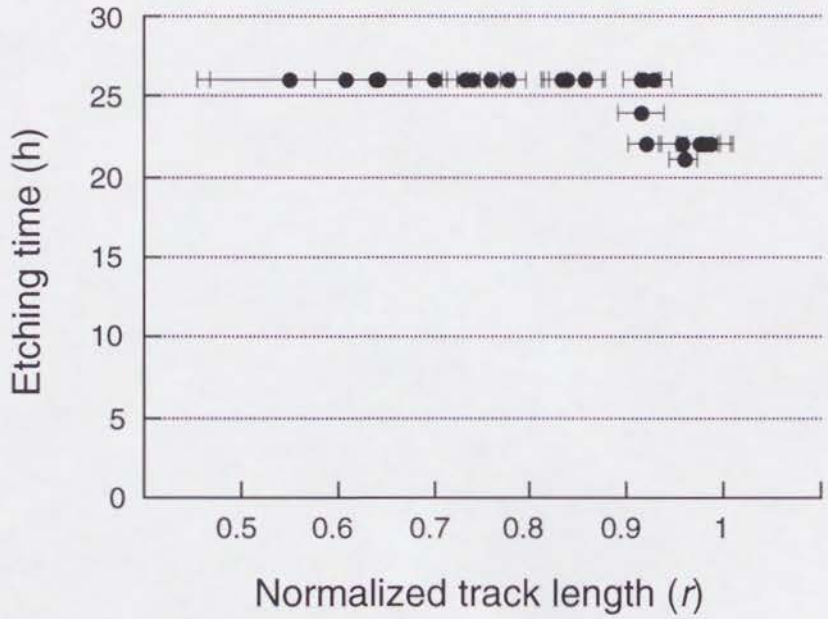

Fig. 4. Relationship between etching time and normalized track length (r). Each point represents one annealing experiment. Note the significant change in etching time at $r \sim 0.93$, reflecting the loss of accumulated α-radiation damage. *Error bars* represent 2σ.

Part III: Orogenic history of the Northern Alps, Central Japan, inferred from fission track thermochronology

The Northern Alps in the Central Japan is located to the west of Itoigawa–Shizuoka Tectonic Line, which is considered as the Eurasian–North American plate boundary. I measured 51 fission track (FT) ages and eight FT length distributions of zircons and three FT ages of apatites, separated from granitic rocks occurring in the middle of the Northern Alps (Fig. 5). Zircon FT age distributions were clearly divided into marginal "older" (> 50 Ma) and central "younger" (< 10 Ma) groups, and all of apatite yielded zero ages. For samples with "younger" ages along an eastward transect, the apparent zircon FT age reduces from 4.2 to 1.6 Ma westward (Fig. 6). The variation in ages and the track length patterns suggests tilted uplifting based on estimated paleodepth of the samples in terms of zircon partial annealing zone when the cooling started. On the other hand, zircon samples were collected at the various altitude ranging from 800 to 2100 m in the middle of the "younger" part. Their apparent FT ages reduce from 6.9 to 0.7 Ma as their altitude declines from 2100 m to 1100 m, whilst ages are almost uniform around 1 Ma at < 1100 m. This fact as well as the characteristic track length distribution pattern of these samples indicated that (i) this area have rapidly uplifted at around 1 Ma and (ii) the estimated geothermal gradient was significantly higher at ~ 1 Ma (~ 70 °C/km) than that of surrounding area at present (~ 40 °C/km) (Fig. 7). Consequently, it was suggested that the uplifting with tilting (~4 Ma) was accompanied with the heat source of 700–800 °C at the bottom of the upper crust, according to the modeling result of the variation of mountain height and underground temperature distribution in terms of uplift rate, uplift duration and the consequent denudation. This stage of uplift may have caused the high geothermal gradient of 70 °C/km at 1 Ma, and the rise of brittle–ductile boundary. In addition, the results of quantitative thermal history analysis for seven zircon samples suggested two events of the cooling rate change.

The uplift history in the Northern Alps region since 4 Ma can, therefore, be divided into two stages in terms of uplift timing and area as follows:

Stage I; uplifting of the whole region of the Northern Alps started 4 Ma, lasted until 1 Ma.

Stage II; uplifting of narrow zone, central part of the Northern Alps, started and completed at around 1 Ma.

For the Stage I, magmatic intrusion to the upper crust may have caused the domal uplifting, which was inferred by the tilted uplifting eastward. This magmatism was probably related to the simultaneous volcanic activity in the Central Japan. The Stage II uplifting of ductile zone, which had been raised at Stage II, may have been caused by horizontal compression by transition of the Eurasian–North American plate boundary.

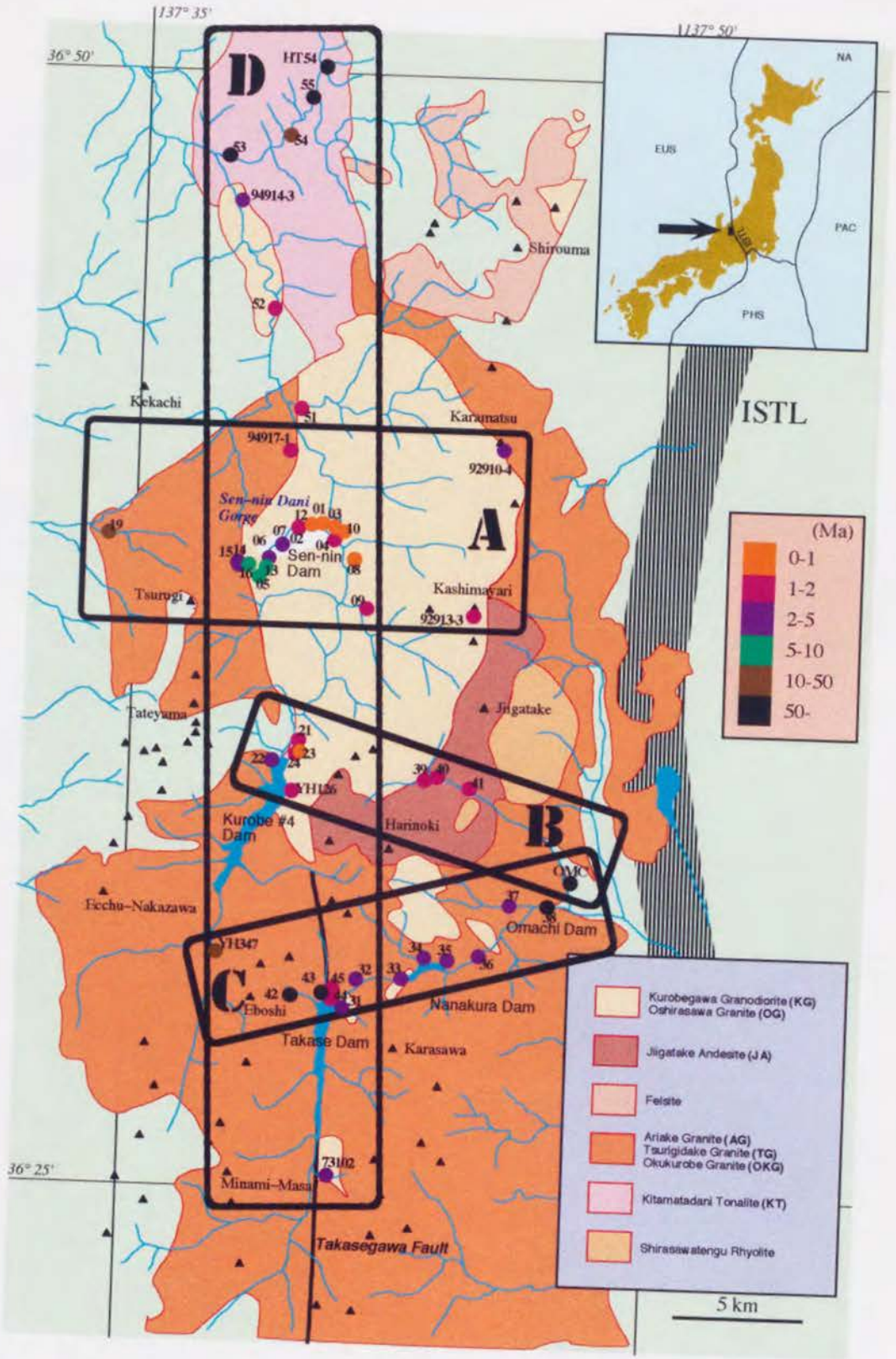

Fig. 5. Simplified geological map of study area and zircon FT age distribution with sampling localities. Geological map is modified after Uchiumi et al. (1995) and Yamada et al. (1989). The extent of the four sampling transects is also shown (A–D). Ages are represented by different symbols as indicated in the legend. Solid triangles indicate summits with the levels > 2500 m.

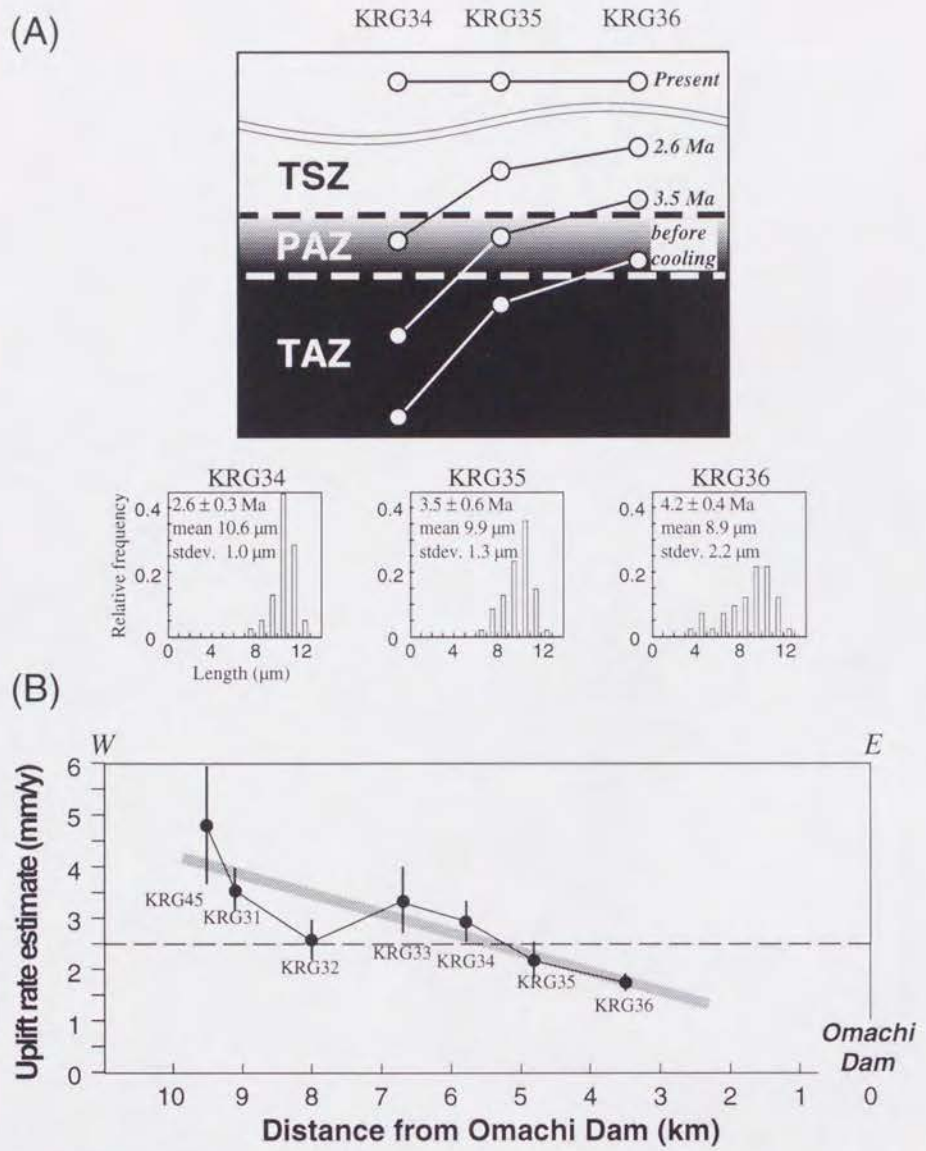

Fig. 6. (A) Schematic diagram of past position of samples of KRG34, KRG35 and KRG36 in terms of partial annealing zone (PAZ), together with the track length histograms. Apparent age (1σ), mean track length and the standard deviation (1σ) were given. The histogram of KRG36 with many shorter tracks indicates that this sample should have suffered the temperature within the bounds of PAZ before uplifting. The skewed pattern of KRG34 and KRG35 indicate that these samples were located in TAZ before uplifting and passed PAZ at a certain rate after uplift started. (B) First order estimates of uplift rate of samples with "younger" ages along Transect C where initial geothermal gradient was assumed 40 °C/km. Uplift rates of each samples were obtained by dividing the depths which correspond to the middle of PAZ of zircon by their apparent ages, indicating the minimum estimates. Horizontal axis is the distance from the Omachi Dam. A shaded line was drown to approximate the relation between uplift rate and the distance, suggesting the tilted uplift eastward. The tilting axis can be given by the extrapolation of this line to uplift rate = 0 mm/y, which corresponds roughly the location of Omachi Dam, where the boundary between "younger" and "older" age samples was recognized in the neighborhood. *Errors* are 1σ.

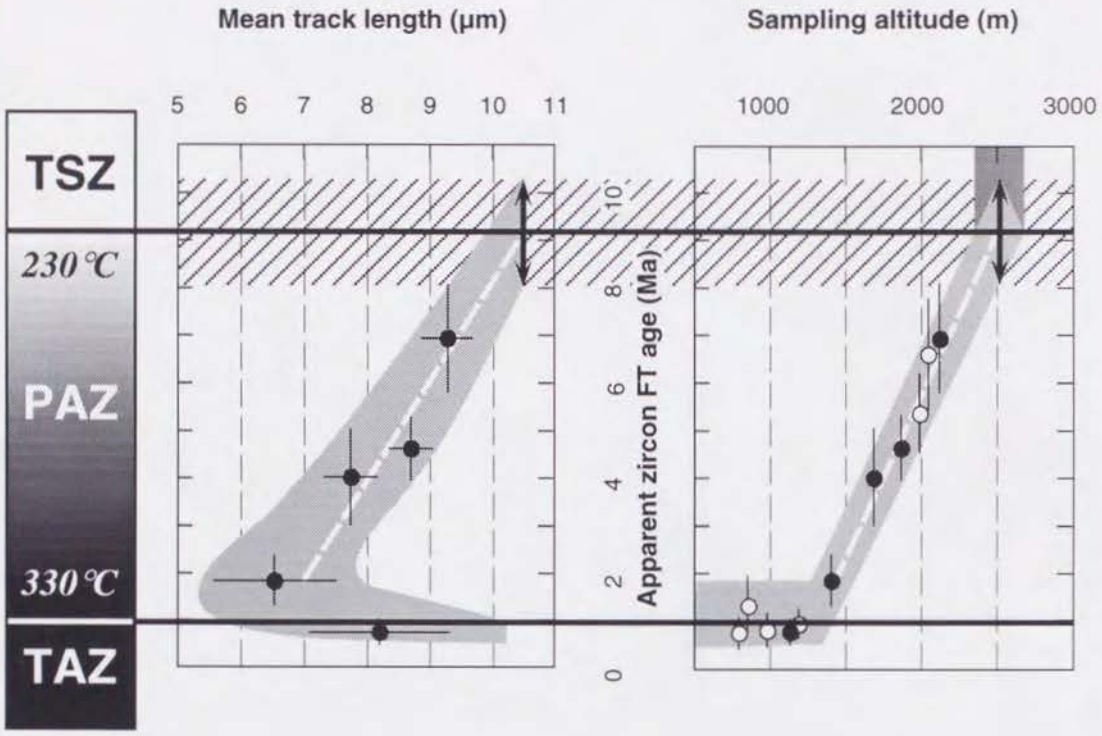

Fig. 7. The relationship among mean track length, sampling altitude, apparent zircon FT age, and fossil zircon partial annealing zone for the samples along the Sen–nin dani Gorge. The left panel shows the temperature scale in terms of the partial annealing zone. TSZ = total stability zone; PAZ = partial annealing zone; TAZ = total annealing zone. Solid circles in the right and central panels are the same data as those in the middle panel. Open circles are of data without length measurements. The bottom of PAZ was estimated to correspond to the apparent ages of 1 Ma. The top of PAZ was estimated as 9.1 ± 1.1 Ma (1σ; striped zone) by extrapolating the regression line for the four older samples (white dotted line in the middle panel; correlation coefficient = 0.96) to the mean track length of 10.5 μm. The sampling altitude corresponding to the top of PAZ can be obtained as 2500 ± 200 m by extrapolating the regression line for the data of samples collected at > 1100 m (white dotted line in the right panel; correlation coefficient = 0.98) to the corresponding apparent age zone. *Errors* are 2σ.

References

Carlson, W.D., Mechanisms and kinetics of apatite fission–track annealing, *Am. Mineral., 75,* 1120–1139, 1990.

Corrigan, J., Inversion of apatite fission track data for thermal history information, *J. Geophys. Res., 96,* 10,347–10,360, 1991.

Crowley, K.D., M. Cameron, and R.L. Schaeffer, Experimental studies of annealing of etched fission tracks in fluorapatite, *Geochim. Cosmochim. Acta, 55,* 1449–1465, 1991.

Dodson, M.H., Closure temperature in cooling geochronological and petrological systems, *Contrib.. Mineral. Petrol., 40,* 259–274, 1973.

Gallagher, K., Evolving temperature histories from apatite fission–track data, *Earth Planet. Sci. Lett., 136,* 421–435, 1995.

Gleadow, A.J.W., I.R. Duddy, and J.F. Lovering, Fission track analysis: a new tool for the evaluation of thermal histories and hydrocarbon potential, *Aust. Petrol. Explor. Assoc. J., 23,* 93–102, 1983.

Gleadow, A.J.W. and P.G. Fitzgerald, Uplift history and structure of the Transantarctic Mountains: new evidence from fission track dating of basement apatites in the Dry Valleys area, southern Victoria Land, *Earth Planet. Sci. Lett., 82,* 1–14, 1987.

Green, P.F., I.R. Duddy, A.J.W. Gleadow, and J.F. Lovering, Apatite fission–track analysis as a paleotemperature indicator for hydrocarbon exploration, in *Thermal history of sedimentary basins. Methods and case histories,* edited by N.D. Naeser and T.H. McCulloh, pp. 181–195, Springer–Verlag, New York, 1989a.

Green, P.F., I.R. Duddy, G.M. Laslett, K.A. Hegarty, A.J.W. Gleadow, and J.F. Lovering, Thermal annealing of fission tracks in apatite, 4, Quantitative modeling techniques and extension to geological timescales, *Chem. Geol., 79,* 155–182, 1989b.

Harrison, T.M., R.L. Armstrong, C.W. Naeser, and J.E. Harakal, Geochronology and thermal history of the Coast Plutonic Complex, near Prince Rupert, British Columbia. Can, *J. Earth Sci., 16,* 400–410, 1979.

Hurford, A.J., Cooling and uplift patterns in the Lepontine Alps south central Switzerland and an age of vertical movement on the Insbruc fault line, *Contrib. Mineral. Petrol., 92,* 413–427, 1986.

Kamp, P.J.J., and J. M. Tippett, Dynamics of Pacific plate crust in the South Island (New Zealand) zone of oblique continent–continent convergence, *J. Geophys. Res., 98,* 16,105–16,118, 1993.

Laslett, G.M., P.F. Green, I.R. Duddy, and A.J.W. Gleadow, Thermal annealing of fission tracks in apatite, 2, A quantitative analysis, *Chem. Geol., 65,* 1–13, 1987.

Lutz, T.M., and G. Omar, An inverse method of modeling thermal histories from fission track data, *Earth Planet. Sci. Lett., 104,* 181–195, 1991.

Uchiumi, S., S. Harayama, and K. Uto, K–Ar dating on age–unknown rocks in the 1:200,000 quadrangle, Toyama, *Bull. Geol. Surv. Jpn, 46,* 375–381, 1995.

Wagner, G.A., G.M. Reimer, and E. Jäger, The cooling ages derived by apatite fission track, mica Rb–Sr, and K–Ar dating: The uplift and cooling history of the Central Alps., *Mem. Inst. Geol. Mineral., Univ. Padova, 30,* 1–27, 1977.

Yamada, N., T. Nozawa, S. Harayama, F. Takizawa, and H. Kato, 1:200,000 Geological Map of Takayama,. Geol. Surv. Jpn., Tsukuba, 1989.

Yamada, R., T. Tagami, and S. Nishimura, Confined fission–track length measurement of zircon: assessment of factors affecting the paleotemperature estimate, *Chem. Geol., 119,* 293–306, 1995a.

Yamada, R., T. Tagami, S. Nishimura, and H. Ito, Annealing kinetics of fission tracks in zircon: an experimental study, *Chem. Geol., 122,* 249–258, 1995b.

Zeitler, P.K., Cooling history of the NW Himalaya, Pakistan, *Tectonics, 4,* 127–151, 1985.

主論文1

Part I: Confined Fission-Track Length Measurement of Zircon; Assessment of Factors Affecting the Paleotemperature Estimate

Ryuji YAMADA, Takahiro TAGAMI and Susumu NISHIMURA

Department of Geology and Mineralogy, Faculty of Science, Kyoto University, Kyoto 606-01, Japan

CHEMICAL GEOLOGY (Isotope Geoscience), 119: 293–306.

(Submitted January 11, 1994: revised and accepted September 6, 1994)

Abstract

We carried out a series of laboratory annealing experiments in order to understand the factors affecting observed confined track lengths in thermally annealed zircon. The variation of confined fission track lengths according to both experimental and analytical conditions was determined on zircons from Nisatai Dacite. It was found that etching temperature, track etching criteria, measurement criteria of horizontal confined tracks (HCT's) and the orientation of HCT's significantly control the observed track lengths where the samples are highly annealed (i.e., > 600°C for 1 h annealing). The first three factors may be related to the presence of gap zones in an annealed track, whilst the fourth is caused by anisotropic annealing and etching characteristics. For reliable thermal history reconstruction, therefore, it should be the minimum requirement to document explicitly the experimental and analytical conditions of these factors in zircon fission–track analysis.

1. Introduction

In thermal history reconstruction of rocks by fission–track thermochronology, confined track length analysis provides valuable information about the patterns of thermal history (Gleadow et al., 1983, 1986ab; Corrigan, 1991) and leaded to quantitative modeling (Green, 1989ab; Corrigan, 1991). It is known, however, that observed fission–track lengths in minerals are controlled by various factors, such as sample's chemistry, annealing anisotropy and experimental conditions (e.g., Laslett et al., 1982, 1984; Green et al., 1986, 1989b; Donelick, 1991 for apatite: Tagami et al., 1990; Yamada et al., 1993 for zircon). Hence the assessment of these factors is of primary importance to reliably interpret fission–track length data in thermal history analysis. In considering the deviation of observed lengths from true ones in a sample, the most essential and largest source of error should be the length–biased sampling (Laslett et al., 1982). For conventional fission–track analysis using chemical etching technique, however, this bias is unavoidable and approximately kept constant for a specific mineral. In addition to this, more importantly, we use the observed length values for reconstructing thermal history throughout (Green et al., 1989a; Corrigan, 1991). Therefore, various factors differentially affecting the observed lengths should be assessed precisely. Considering the length measurement procedure, possible factors are as follows. (1) Sample factor: Rock samples have various chemical compositions of major elements. The difference of Cl content is highly important for annealing characteristics of apatite (e.g., Green et al., 1989b); whilst for zircon, the replacement of Zr with Hf should be considered as a single factor to control annealing characteristics of zircon. Also the degree of accumulated radiation damage differs between samples, caused by their age (radiated duration) and uranium contents. The effects of the presence of α–decay damage on annealing characteristics were dealt with by Kasuya and Naeser (1988). (2) Anisotropic annealing: Fission track annealing of apatite is reported to proceed anisotropically (e.g., Green et al., 1986; Donelick 1991) and track lengths significantly differ with the crystallographic orientations. For zircon, the anisotropy has been little studied in detail with few exceptions (e.g., Tagami et al., 1990). (3) Observation factor: Chemical etching procedure is needed for the conventional track observation under optical microscopes since latent fission tracks have widths of ~ 10 Å and are invisible under them (e.g., Paul and Fitzgerald, 1992). For zircon, this procedure may substantially control observed track length because the track revelation rate differs with etchant and temperature (e.g., Gleadow, 1976) and shows remarkable anisotropy (e.g., Gleadow, 1981, Yamada et al., 1993). In addition, confined track lengths were conventionally measured with the help of tracks–in–tracks and/or tracks–in–cleavage (TINT's and TINCLE's, respectively; Lal et al., 1969; Laslett et al., 1982), which may show some systematic difference in observed lengths (e.g., Laslett et al., 1984).

Of these factors, those considered to substantially affect measured track lengths in zircon were investigated in this paper: that is, anisotropy of fission track annealing, the difference between TINT's and TINCLE's, chemical composition, etching temperature and etching criteria. During the assessment of those experimental criteria, some important features of the track annealing behavior in zircon, described previously (e.g., Tagami et al., 1990), were made clear and thus better understood.

2. Sample Preparation and Experimental System

The zircon samples used in this study, called here as NST, were separated from a dacitic welded tuff of the Nisatai Dacite, occurring in the northern part of the Kitakami mountain range, northeast Japan. The NST has a K–Ar biotite age of 21.0 ± 0.3 (2σ) Ma and a spontaneous track density of ~ $3 \cdot 10^6$ cm^{-2} (Tagami et al., 1994). The zircon crystals are euhedral and clear so that their crystallographic *c*–axes are readily determinable, and thus suitable for the aim of this study. In addition, their spontaneous tracks are not geologically annealed after formation, confirmed by the concordance between the spontaneous and induced track lengths (10.83 ± 0.10 (1σ) μm and 11.05 ± 0.11 μm, respectively).

After mineral separation using conventional heavy liquid and magnetic separation techniques, some amounts of zircon grains were heated at 1009 ± 2°C for 2 h in order to remove all spontaneous tracks therein. Then, they were irradiated for 30 min. at the Thermal Column Pneumatic Tube (Tc–Pn) facility of Kyoto University Research Reactor (KUR) to produce induced tracks in the grains, resulting in an induced track density of ~ $6*10^6$ cm^{-2}. A small portion of the samples was kept for measuring the initial spontaneous and induced track lengths, and the remaining samples were employed for track annealing. The duration, temperatures and detailed analytical procedures are described in following sections. About 150–300 zircon grains were mounted in each polytetrafluorethylene–perfluoroalkoxyethlene (PFA) teflon sheet and their external prismatic surfaces were polished to expose internal surfaces. Spontaneous and induced tracks used for analysis were etched in NaOH–KOH eutectic etchant (Gleadow et al., 1976) at 248 ± 1°C or 221 ± 2°C (for comparison only, see the Section 3–3), until the width of the surface tracks perpendicular to *c*–axes became 2 μm (2 μm criterion) or 1 μm (1 μm criterion; for comparison only, see the Section 3–5).

The tracks used for length measurement were horizontal confined tracks (HCT's; Laslett et al., 1982) throughout the study, containing track–in–tracks and track–in–cleavages (TINT's and TINCLE's, respectively; Lal et al., 1969; Laslett et al., 1982). HCT's with widths of 1 ± 0.5 μm were selectively measured to minimize the overetching factor (i.e., the rate of track length increase to track width increase during etching, after reaching the plateau stage of track revelation subsequent to initial rapid etching stage of tracks; cf. Yamada et al., 1993). The lengths of HCT's were measured using a digitizing tablet interfaced with the Hamamatsu® C2500 Image Processing System, combined with a Nikon® Biophot microscope. For a 100x dry objective and 10x eyepieces, which result in a true measured magnification of 925x, the precision of measured track length is ~ ± 0.1 μm (1σ). For scanning all grains in the sheets, samples were analysed with the help of a Sapporo® Micro Scanner automatic scanning stage installed to Biophot microscope. The orientations of HCT's were measured in angles to the crystallographic *c*–axis with a precision of ~ ± 1° using C2500 system. The track length and

orientation data of each measurement were recorded together with the video image of the measured track on the video copy printed by the Mitsubishi® Video Copy Processor SCT–P75 interfaced with the Hamamatsu® C2500.

3. Assessment of Various Factors

3–1. Anisotropy of Fission Track Annealing

To investigate the effects of various kinds of anisotropy, such as annealing and overetching, measured HCT lengths were plotted against their crystallographic direction using the data of spontaneous and induced tracks annealed for 1 h at about 400–700°C (Fig. 1). As the annealing temperature becomes higher, the length of the spontaneous HCT's decreases gradually and yields a rather negative correlation to the angle to the *c*–axis. In addition, the number of observed HCT's is consistently anisotropic during annealing, revealing more tracks for greater angles to *c*–axis.

Considering the overetching factor, analysis of HCT length with greater angle to the *c*–axis is desirable (Yamada et al., 1993; see also Hasebe at al., 1993). Thus the ratios between mean HCT lengths over 60° to the *c*–axis ($L_{(60)}$) and that of all directions ($L_{(all)}$), i.e., $L_{(60)}/L_{(all)}$, were plotted against the length reduction ratio L/L_0 (Fig. 2). It shows a positive trend with all data which have the ratio smaller than 1, except for one point . This fact indicates that track lengths are slightly anisotropic in the initial stage of annealing due to the inherent anisotropy of latent track length and/or anisotropic overetching factor, and that the anisotropy substantially increases as the annealing proceeds. Since the mean HCT length of whole orientations largely depends on the tendency of the HCT appearance, which differs between samples (Hasebe et al., 1993), it is important to specify the crystallographic orientation for reliable HCT length analysis, especially in highly annealed stages. Hence we recommend to measure and analyse HCT's with the angles, for example, over 60° to the *c*–axis. This criterion is based on four constraints: (1) For > 60°, the effect of overetching factor is negligibly small for HCT measurement (Yamada et al., 1993). (2) For > 60°, the number of observed HCT's is approximately uniform for various induced track samples, presenting extremely anisotropic state (Hasebe et al., 1993). (3) For > 60°, the HCT length reduction patterns are approximately the same for spontaneous tracks (Fig. 1a). (4) For higher angles to *c*–axis, HCT lengths are more readily shortened during annealing, offering more sensitive thermochronologic parameters. Note that using this criterion, the reduction in number of analysable HCT's is generally small (Fig. 1; see also Hasebe et al., 1993). This 60° criterion should accordingly be adopted hereafter for the analyses of spontaneous HCT length.

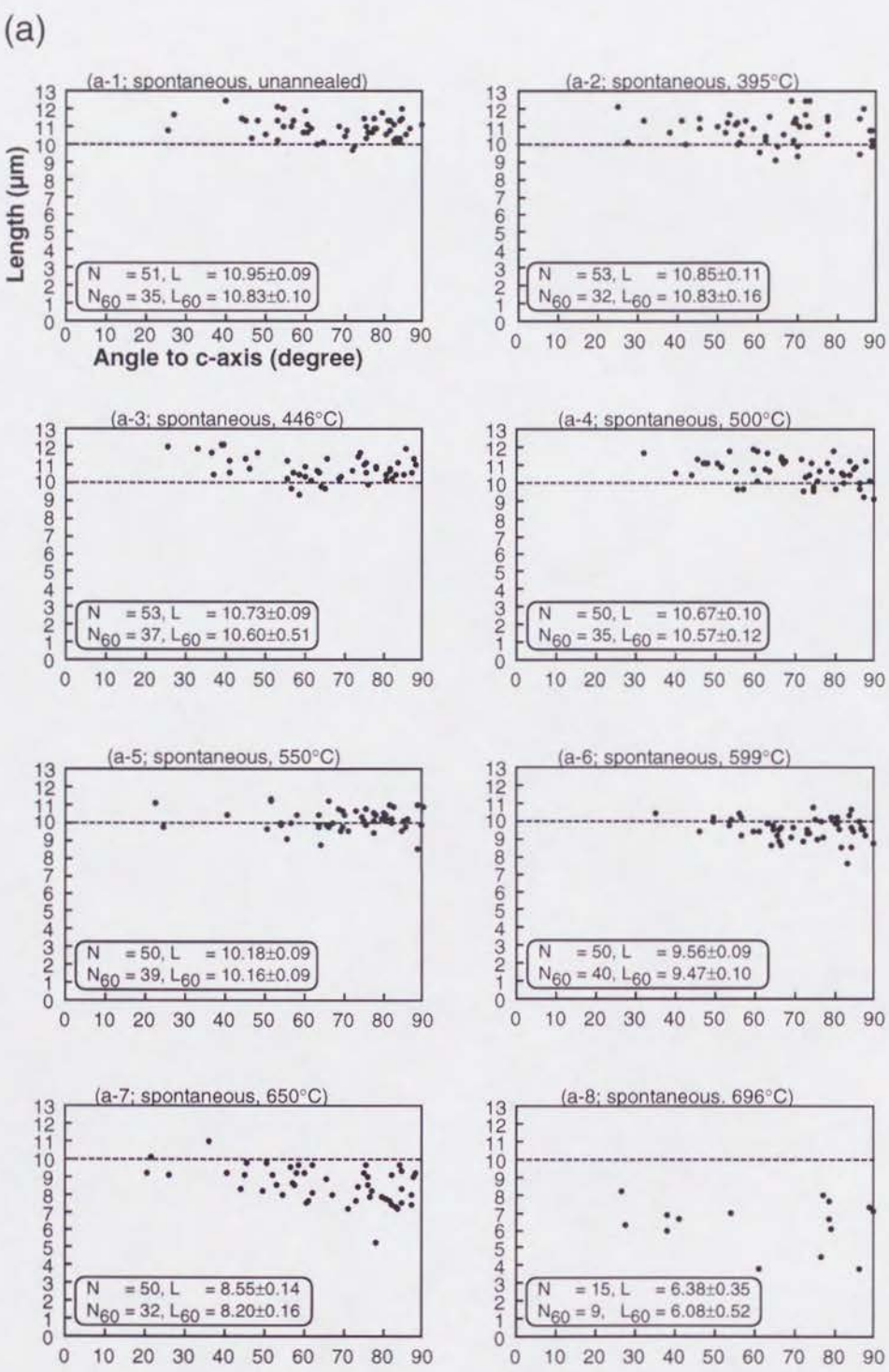

Fig. 1. (For caption see next page.)

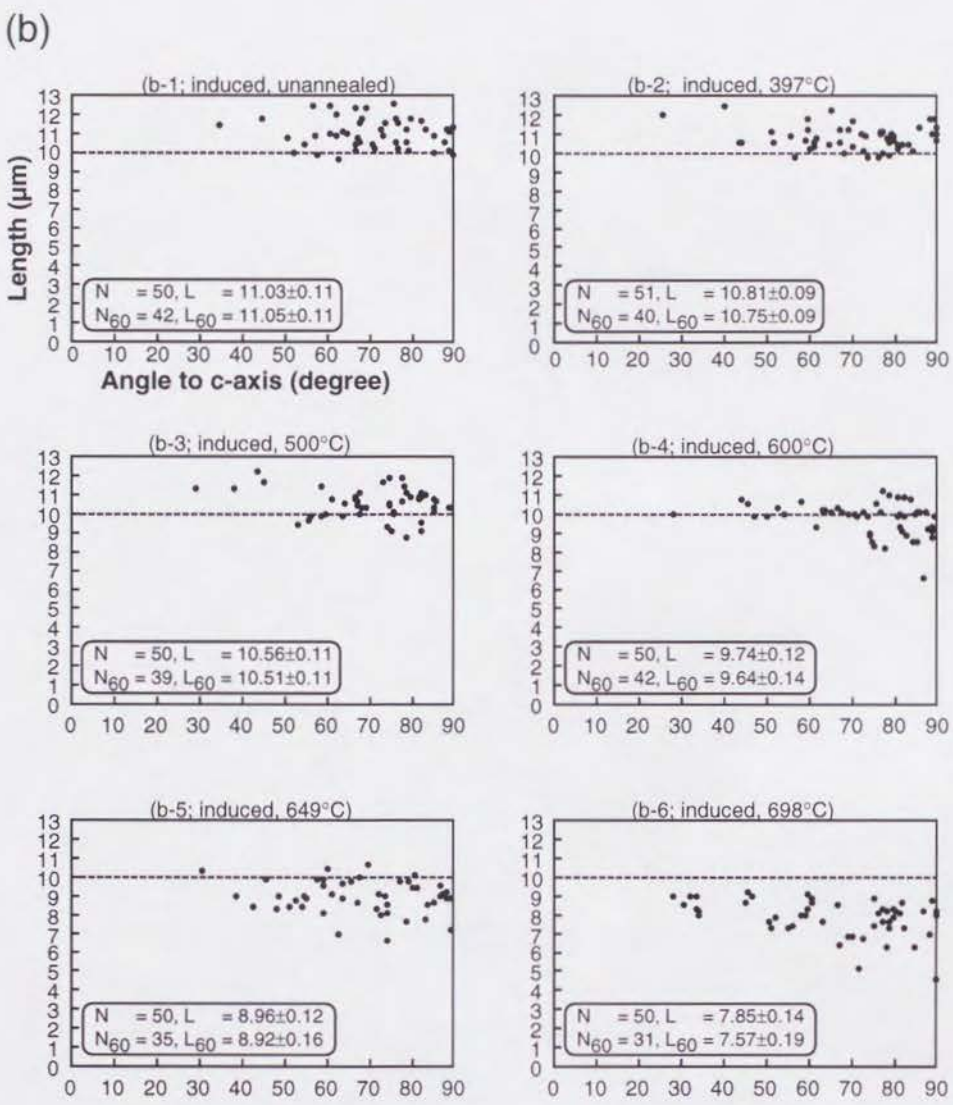

Fig. 1. Variation in HCT length distribution of NST zircons against angles to *c*–axis during 1 h isochronal annealing: (a–1 ~ 8) spontaneous tracks, (b–1~ 6) induced tracks. Annealing temperatures are also shown in the headings. 'N' and 'L' indicate the number of counted tracks and the mean length of measured HCT's with standard errors (1σ), respectively. The subscripts '60' mean the values of tracks having angles over 60° to the *c*–axis. Etching time was 21 h (a-3), 22 h (a-1, 2, 4, 5) and 26 h (others), at 248 ± 1°C, respectively. No HCT's were found for both spontaneous and induced samples annealed at 750°C. Note that tracks show highly anisotropic distributions and that tracks with greater angles to *c*–axis are slightly shorter at advanced stages of annealing.

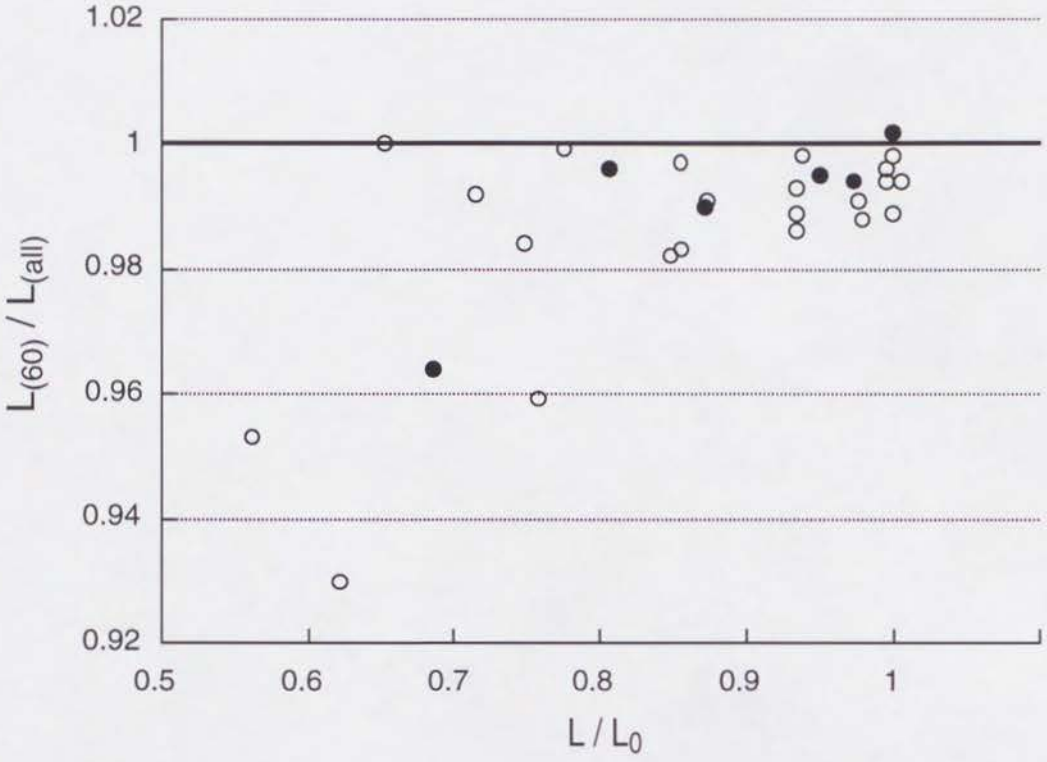

Fig. 2. Ratios of the mean HCT length for > 60° to *c*–axis ($L_{(60)}$) and that for all directions ($L_{(all)}$), plotted against the degree of track annealing L/L_0 (L_0 = mean HCT length for an unannealed sample; L = mean HCT length for annealed sample). Plotted data are from a set of annealing experiments performed in various time–temperature conditions. There is no significant difference in trends between spontaneous (*open circles*) and induced (*solid circles*) HCT's.

3–2. TINT's vs. TINCLE's

Two types of HCT's are conventionally used for length measurement, i.e., TINT's and TINCLE's. Because they are enlarged by the etchant that passed through host features of different geometry, they may have different biases in observing HCT's. To examine the difference of the mean length between TINT's and TINCLE's, the mean length ratios of TINCLE's and all HCT's, $L_{(TINCLE)}/L_{(all)}$, were plotted on Fig. 3. In the case of NST zircons, numbers of TINT's were found to be consistently greater by about an order of magnitude than that of TINCLE's. Data sets containing at least five TINCLE's with over 60° to *c*–axis were thus chosen for comparison from a series of annealing experiments performed in various temperature–time conditions. This plot shows that mean lengths of TINCLE's are not significantly different from those of TINT's except one data set. The plot also suggests no variation of $L_{(TINCLE)}/L_{(all)}$ against the degree of annealing.

The results mentioned above suggest that the bias due to the measurement of TINCLE's is not significant for mean HCT length calculation. In addition, the possible bias for the single exception (spontaneous tracks annealed for 11 h, at 548°C, containing five TINCLE's) needs a correction of only 0.7% in the mean length value by excluding five TINCLE's data. TINCLE's should be useful for highly annealed samples in order to increase the number of HCT's because TINT's are difficult to detect therein due to the shortening of host tracks. Therefore, both TINT's and TINCLE's shall be used hereafter. Nevertheless it is noted that the HCT length difference between the two may be enhanced by measuring HCT's in all directions.

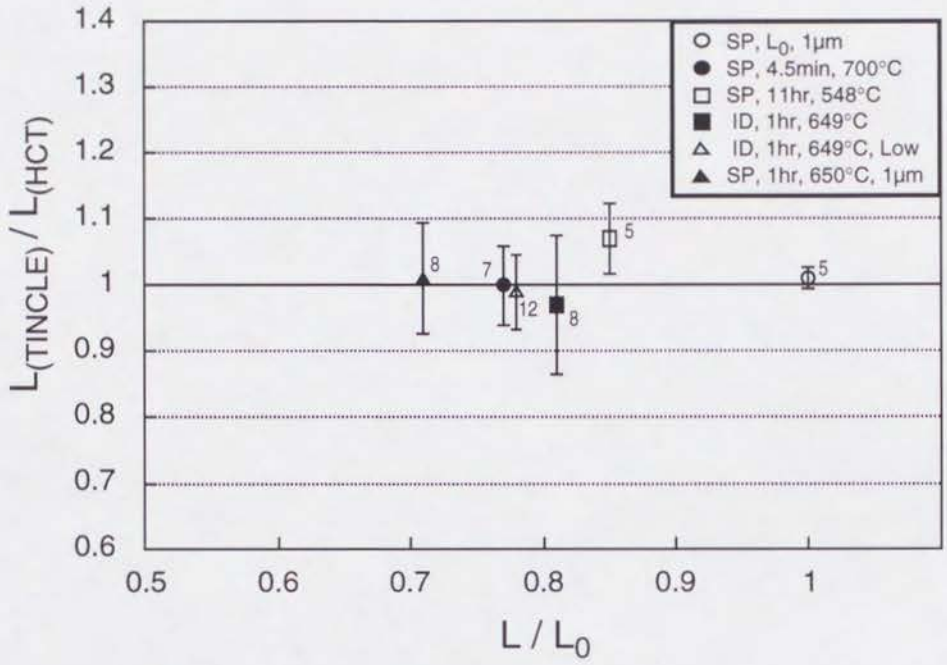

Fig. 3. Ratios of the mean length of TINCLE's ($L_{(TINCLE)}$) and that of all HCT's ($L_{(HCT)}$), plotted against the ratio of track length reduction, L/L_0. Numbers beside symbols indicate the numbers of measured TINCLE's. Here the samples containing more than five TINCLE's were plotted. In the legends of symbols, *SP* and *ID* denote spontaneous and induced tracks, respectively; L_0 unannealed tracks; *Low* = low etching temperature (see 3-3); *1 μm* = 1 μm etching criteria (see 3–5): the annealing duration and temperature are also shown. *Error bars* represent ± 2σ of standard error.

3–3. Chemical Composition

As will be shown in the Section 4, significant differences are found in length reduction patterns between the present results and previous data using KT06 zircon (e.g., Tagami et al., 1990). It is possible that this is caused by the difference in the chemical composition, which is the major cause to control annealing characteristics in apatite (Green et al., 1986). Since the mineral zircon seldom has a solid solution, it is expected that the difference in major element components should not control annealing characteristics. However, 2–4 % of zirconium contained in natural zircon is replaced by the other actinides, of which Hf is the most important (Deer et al., 1982), and this could cause the difference between Tagami et al. (1990) and this study. In order to investigate this possibility, the chemical compositions of the two samples were preliminary analysed and compared quantitatively by the Kevex–Delta IV electron microprobe analyser (Hirajima and Banno, 1991), noting mainly Zr and Hf contents.

We analysed four zircon crystals; two grains for each (KT06 and NST). The ratios of Hf/Zr (mol) are plotted in Fig. 4. These values approximately correspond to the replacement ratio of Zr into Hf. The spatial chemical difference in each grain can be estimated from the electron–probe spotted points named A and B, whilst the difference between grains for each sample from A and C. Fig. 4 shows that the variations in Hf/Zr ratio are consistently small, compared to previous results of electron microprobe analyses of granitic rocks (0.004–0.042 of Hf/(Zr + Hf) ratio; Suzuki and Yogo, 1986). The differences in each grain are evaluated as ~ 0.002 (KT06) and < 0.001 (NST), and that between grains are ~ 0.003 (KT06) and ~ 0.002 (NST). The difference of Hf/Zr ratio between two samples is ~ 0.002. Our result indicates that no significant differences in Hf/Zr ratio were found between the grains for each sample and as well as between the two samples, implying little differential influence on their track annealing behaviors. It therefore suggests that other experimental factors, as will be discussed in the Section 3–4 and 3–5, should result in the difference in HCT length reduction patterns between the two mentioned above. In conjunction with the previous results (Kasuya and Naeser, 1988), it is speculated that the sample factor does not play an important role in zircon annealing, although further extensive studies are strongly needed.

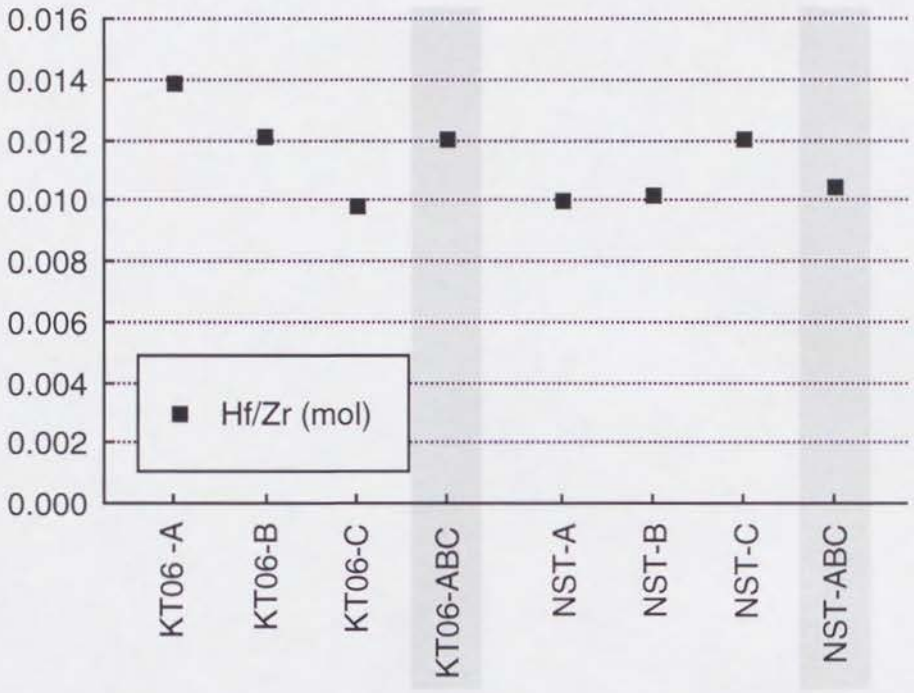

Fig. 4. Hf/Zr ratios of zircon grains of KT06 and NST samples, using electron microprobe analyser. In code names aligned along the horizontal axis, *–A*, *–B* and *–C* correspond to each electron–probe spotted point on the analysed grains, respectively. *–ABC* indicates a mean value of *A*, *B* and *C* data (meshed). As for KT06, the slight zoning of uranium content has been observed by density distribution of surface fission tracks after etching.

3–4. Etching Temperature

In etching latent tracks with NaOH–KOH eutectic solution (Gleadow, 1981) to be observable under an optical microscope, the temperature of etchant controls etching time until surface tracks are enlarged to a certain size. For NST zircon used throughout this study, 26 h etching was necessary until the width of induced tracks perpendicular to *c*–axis became 2 μm at 248 ± 1°C, and 120 h at 221 ± 2°C (Hasebe et al., 1993). This fact suggests that the etching temperature substantially affects track revelation rates and may control the etching efficiency and observed track lengths as well.

In order to investigate the effect of etching temperature, we compared the measured mean length of spontaneous and induced HCT's annealed for 1 h at about 600, 650 and 700°C, as plotted in Fig. 5. For both spontaneous and induced HCT's, results of lower temperature etching show rather smaller values than those of higher temperature. This suggests that etching at higher temperature would make the observed track length slightly longer than that at lower temperature even when the same etchant and criteria were adopted. The difference in spontaneous HCT lengths in the most advanced stage of annealing (~ 700°C) is ~ 0.7 μm. As will be discussed in the following section (*3–6. Significance of gap zones*), this fact may be related to the existence of gaps in an annealed HCT.

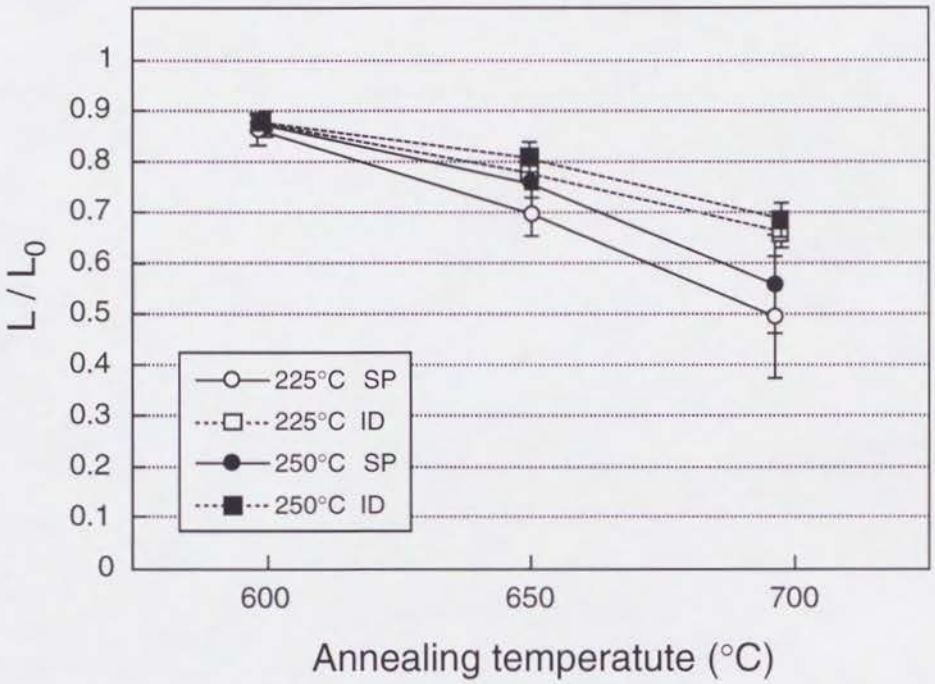

Fig. 5. HCT length reduction measured at different etching temperature. Spontaneous (*circles*) and induced (*squares*) samples were annealed at ~ 600 – 700 °C for 1 h and etched at 248 ± 1°C (*solid symbols*) and at 221 ± 2°C (*open symbols*), respectively. Etching time was 26 h (at 248 ± 1°C) and 120 h (at 221 ± 2°C), respectively. *Error bars* represent ± 2σ.

3–5. Etching Criteria

Since the etching procedure inevitably affects the measured track length, etching criteria must be carefully decided for reliable analysis. Zircon has an anisotropic etching characteristic (Yamada et al., 1993; see also Gleadow 1981; Sumii et al., 1987): a bulk etching rate is greater for the orientation parallel to the crystallographic *c*–axis compared to that perpendicular to it. Thus tracks parallel to the *c*–axis need longer etch time to be sufficiently widened and visible. As an index for degree of etching in such an anisotropic medium, it is convenient to use the width of surface tracks which are perpendicular to the *c*–axis, representing the maximum diameter of tracks (Tagami et al., 1990; Hasebe et al., 1993). Note this index can be applied to any samples with various track densities and even to those partially annealed.

To examine the influence of etching state on observed lengths, track length reductions during annealing were compared between 1 μm and 2 μm etching criteria (Fig. 6), using spontaneous HCT's annealed for 1 h, at 599, 650 and 696°C. For annealing at 599°C, the measured mean length of HCT's are indistinguishable between the two criteria. However, when the temperature is elevated up to 650°C and 696°C, mean lengths measured with 1 μm criterion are shorter (Fig. 6). The difference in spontaneous HCT lengths in the most advanced stage of annealing (~ 700°C) is ~ 1.0 μm. This feature means that longer etch tends to make the HCT longer, although the adopted criterion to measure HCT's is consistently 1 ± 0.5 μm width.

To investigate the relationship between observed HCT length and etching time, the step–etch experiment was executed, using induced HCT's annealed for 1 h at 698°C (this aliquot was used because it can yield a great number of shortened HCT's than spontaneous ones, as shown in Fig. 1). Etching was performed in 4 h intervals at 248 ± 1°C. As a result, lengths of several HCT's were measured successively for at least three steps, as plotted in Fig. 7. Two of them (#13 and #22) yielded remarkable increases in length from 8 to 12 and 20 to 24 h etching, respectively, whilst others showed slight changes.

The photographs of two typical HCT's during step–etch are presented in Fig. 8: #11 track yielded a normal growth pattern (a), whereas #22 yielded a sudden increase in length (b). In the latter case, a very thin part of a track end appears after etched for 20 h. At next stage, 24 h etching, this part has been further enlarged so that the whole range of the HCT passed the measurement criteria, i.e., 1 ± 0.5 μm width. Here we note that such features are not exceptional but also found in other grains (Fig. 8(c)). These results suggest that the mean HCT length in the earlier etching stage (etching time = 12–16 h) would be estimated shorter than that in the later stage (20–24 h). It is noticeable that the maximum width of surface tracks is ~ 1 μm in the earlier stage, since this aliquot needs 26 h to satisfy a 2 μm criterion. Difference in mean

lengths between the two etching criteria and the increase in standard deviation with the decreasing L/L_0 (Fig. 10) should be attributable to this sudden extension of annealed HCT's. Similar observation has been previously reported on HCT's in annealed apatites (Green et al., 1986).

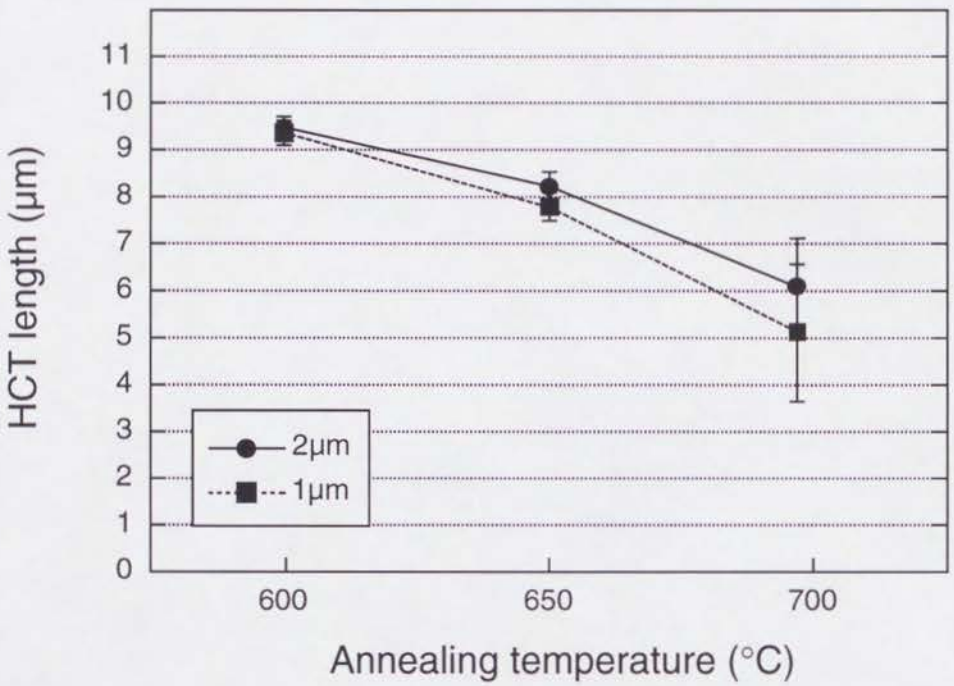

Fig. 6. Mean length reductions observed for spontaneous HCT's, adopting two different etching criteria; 2 µm (*circles*) and 1 µm (*squares*) widths (see text). Samples were annealed at ~ 600–700 °C for 1 h and etched at 248 ± 1°C. Etching time was 26 h (2 µm) and 13 h (1 µm), respectively. *Error bars* represent ± 2σ.

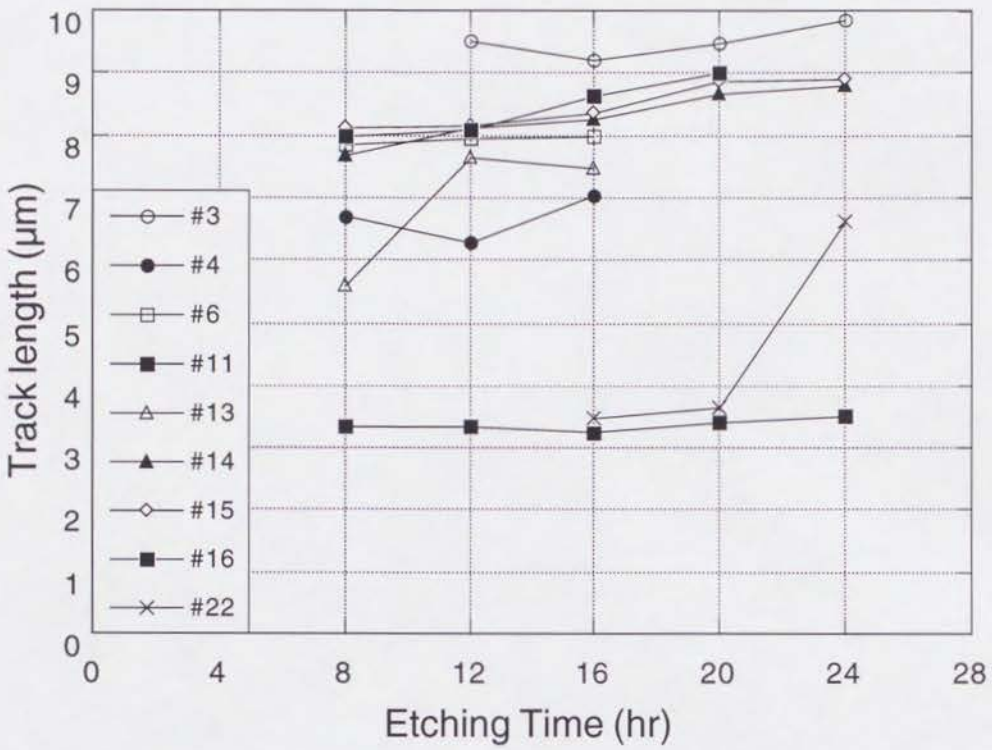

Fig. 7. HCT length growth patterns during step–etch. Each *symbol* represents an individual HCT measured. Standard errors for each measurement are ~ ± 0.1 μm, smaller than plotted symbols. Note the remarkable sudden increase in length for two samples; #13 from 8 to 12 h and #22 from 20 to 24 h.

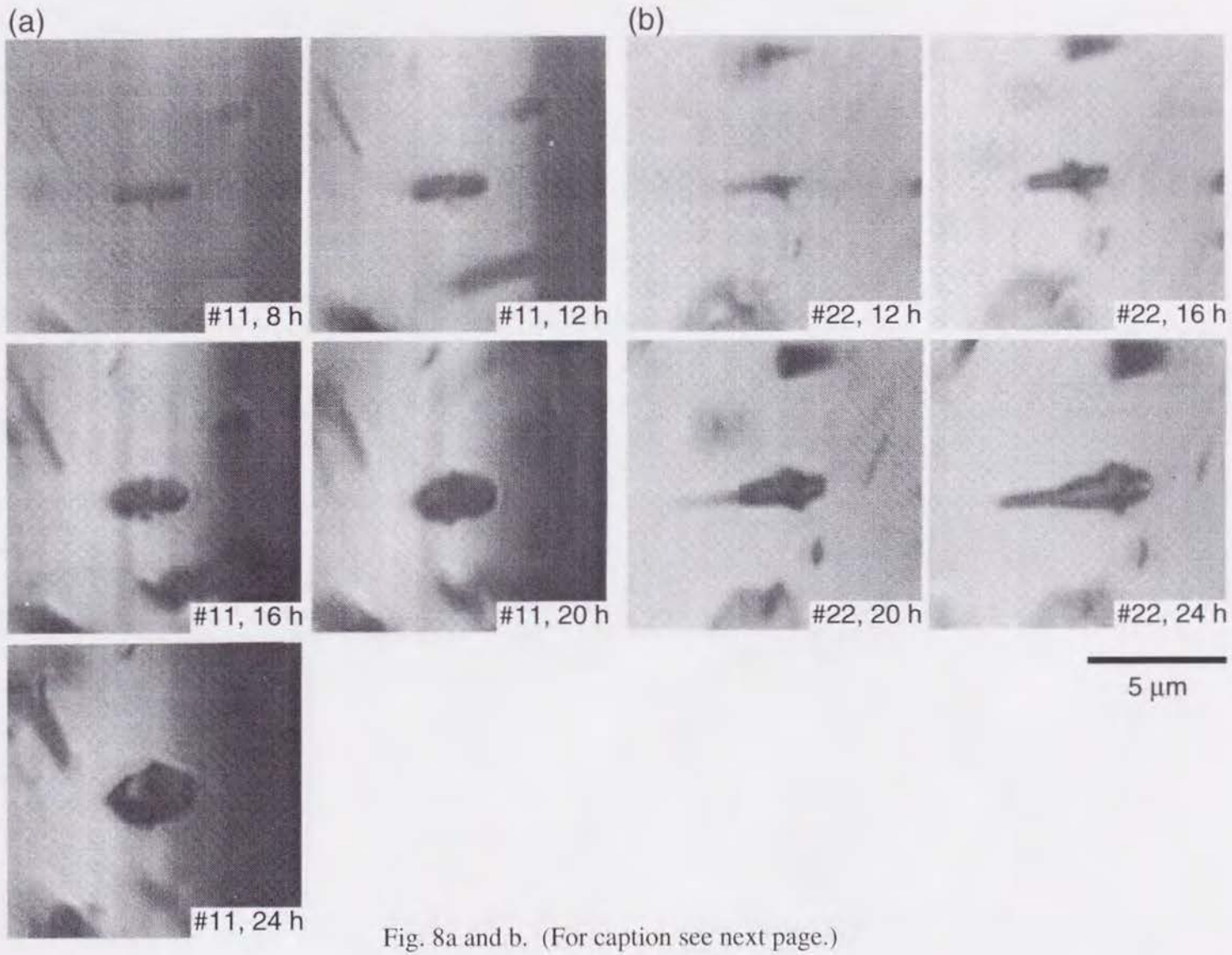

Fig. 8a and b. (For caption see next page.)

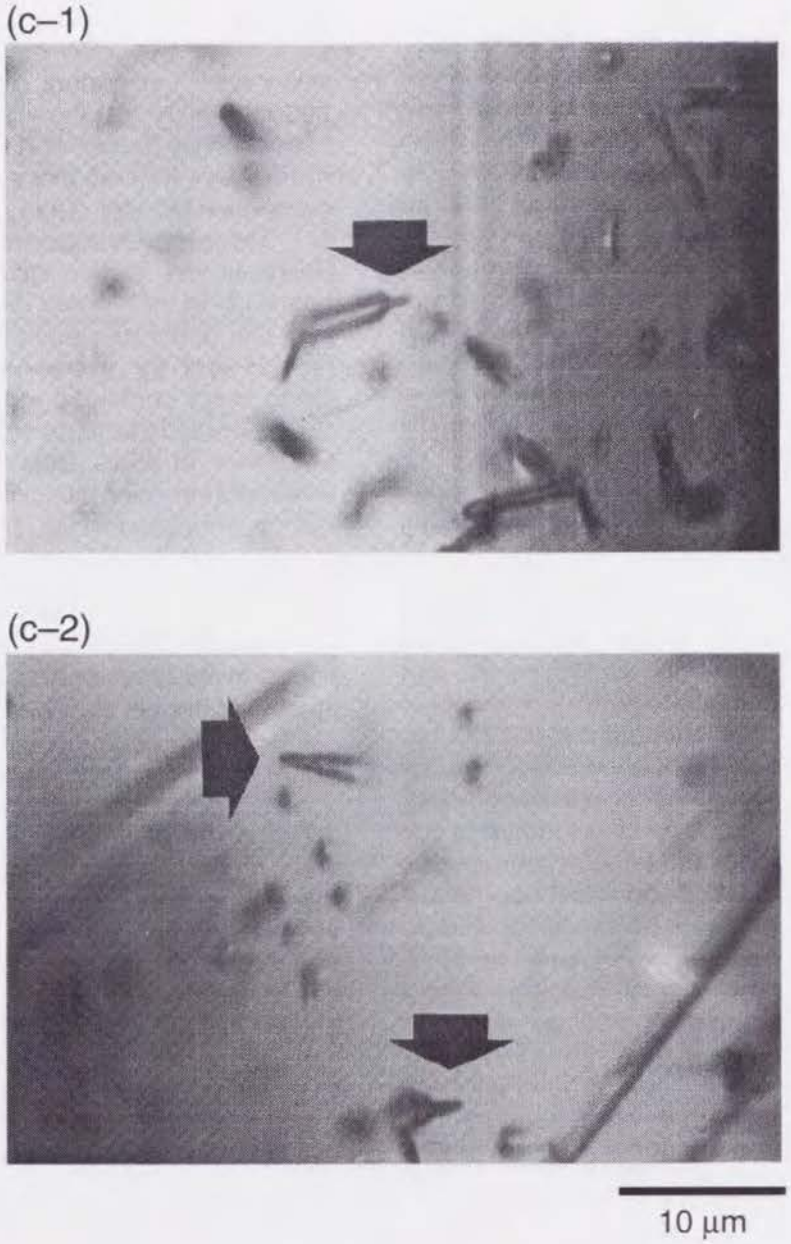

Fig. 8. Photographs of step–etched HCT's that were annealed at 698 °C for 1 h, taken with a Nikon® Biophot microscope using transmitted light (200x dry objective and 10x tube factor). Track numbers and etching time corresponding to Fig. 7 are presented below each photograph: (a) #11 from 8 to 24 h, showing a normal growth pattern, whereas (b) #22 from 12 to 24 h, a sudden increase in length resulting in a combination of two portions with contrasting diameters. Photographs c–1 and c–2 show surface tracks with a thin part at each end (indicated by *arrows*), resembling to the characteristic feature in (b). Etching temperature was 248 ± 1°C.

3–6. Significance of Gap Zones

Paul and Fitzgerald (1992) presented a schematic model of partially annealed tracks in apatite by TEM (transmission electron microscope) observation (Fig. 9(a)). They found the presence of gap zones along an annealed latent track length and interpreted that small gap zones are likely obliterated by chemical etching to form a continuous etched track, and only large gap zones may be preserved as 'non–etchable gaps' reported by Green et al. (1986). By combining their model and the experimental results mentioned above, the fission track annealing process in zircon is estimated as follows (Fig. 9(b)): first, an unannealed latent track is annealed from both ends according to elevated temperature and/or extended heating. Under an optical microscope, this stage is observed as the apparent shrinking of the etchable range of tracks. Accordingly, measured HCT lengths are approximately the same between the two measuring criteria (Fig. 6; corresponding to the annealing condition of <~ 600°C, for 1 h). Second, as the track annealing proceeds, the recovery occurs at various portions of the track already shortened, probably with some preferential recovery from both ends considering track formation process (Fleischer et al., 1975). As a result, rather short segments survive with various ranges of gap zones formed. This stage is characterized by a sudden increase in the number of short tracks, which results in the different HCT length between the two criteria (Fig. 6; > ~ 600°C, 1 h) accompanied by the increase in the standard deviation of track length distribution (Fig. 10). Finally, both number and range of gap zones increase further and survived segments accordingly become too short to be detected. Based on this model, Fig. 9(c) illustrates a schematic process of the TINT etching with a relatively great gap. At the first stage, a survived segment of a TINT is etched by encountering with a host track during etching, from which etchant is supplied. As the etching proceeds, the segment previously etched is further enlarged and eventually meets the other unetched segment that also survived during annealing. Subsequently, the segments are attacked as a whole to form a TINT consisting of two portions of contrasting diameters. This schematic etching process reasonably explains the observation shown in Fig. 8(b).

The presence of gap zones in highly annealed zircons also raises the necessity to set measurement criteria of HCT's, e.g., the 1 ± 0.5 μm width adopted in this study. Besides the influence of overetching factor (Yamada et al., 1993), HCT length is significantly increased by breaking through gap zones during prolonged etching. Therefore, it is required for precise analysis to selectively measure HCT's having similar etching state. For such purpose, we consider that the best parameter to measure degree of etching is the width of HCT's. Considering the reduction in number of measurable HCT's, criterion of 1 ± 0.5 μm width is of practical use for routine analysis with the help of micrometer attached to an eyepiece of microscope.

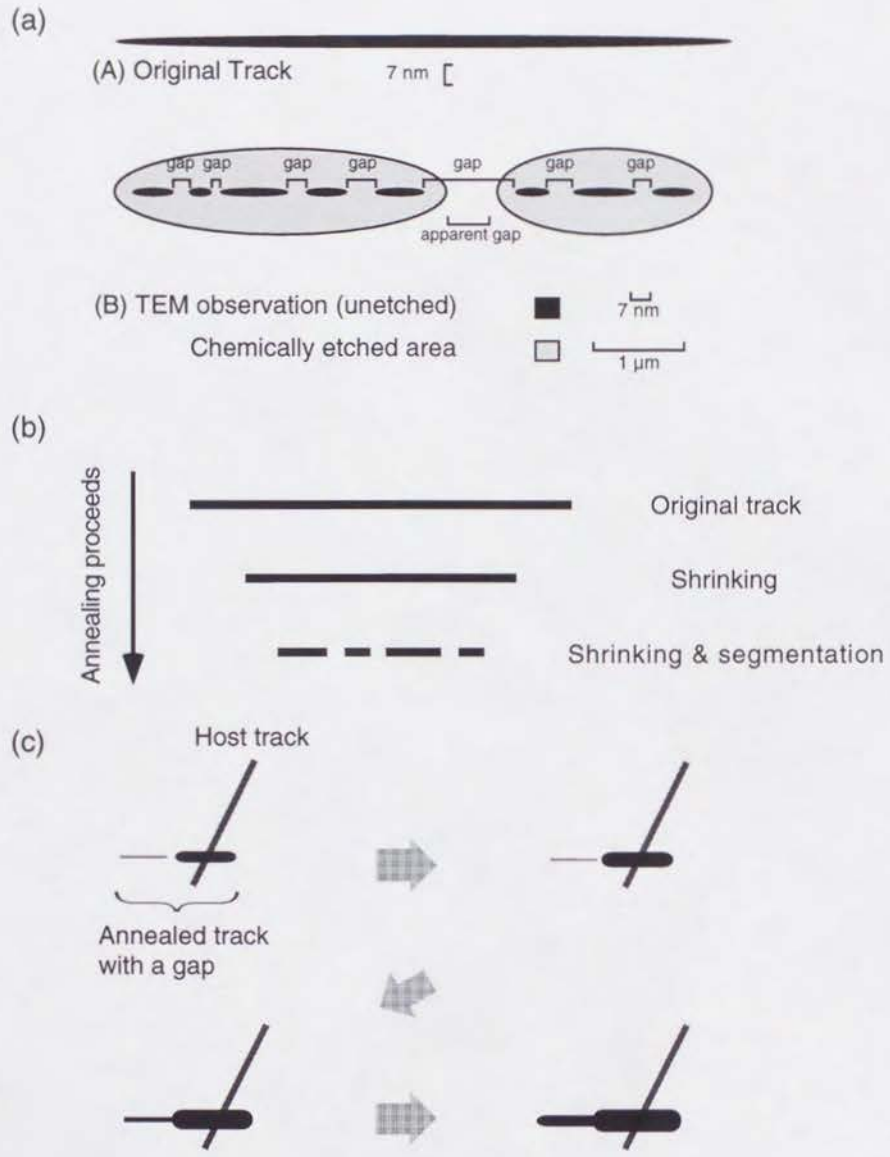

Fig. 9. (a) Magnified schema of (A) unannealed and (B) partially annealed tracks by TEM observation (after Paul and Fitzgerald, 1992; modified). Gap zones present in a partially annealed track; small gaps (~ 10 nm) are easily etched and invisible under an optical microscope, whilst a larger gap (~ 1 μm) survives during chemical etching and observed as an apparent gap. Note the appropriate *scale bar* associated with each method of observation.
(b) Schematic diagram of fission–track annealing process in zircon. As annealing proceeds, an original latent track shrinks gradually. Second, the track begins segmentation and gap zones appear along the original track part.
(c) Schematic process of the TINT etching with a relatively great gap. Four steps in this figure correspond to four photographs of #22 (see Fig. 8(b)).

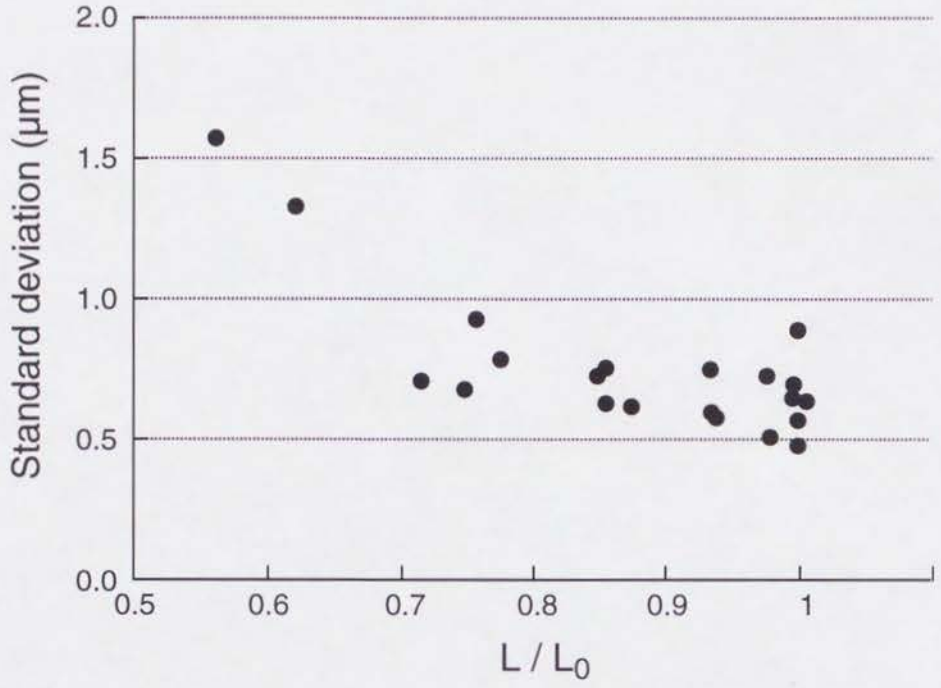

Fig. 10. Standard deviation of HCT length distributions plotted against degrees of length reduction (L/L_0), taken from a set of annealing experiments in various time–temperature conditions. Each data point represents one annealing experiment. Note the general increase in standard deviation for L/L_0 below ~ 0.8.

It is noted that the etching temperature factor (see the Section 3–3) may also be related to the existence of such gaps in annealed zircon. This factor emerges where the annealing has highly proceeded, i.e., > 600°C for 1 h annealing. These conditions approximately coincide with that for the emergence of etching criteria factor, which should be the reflection of gap zones. Since such thermally recovered portions in a latent track would have faster etching rates than bulk regions (comparable to the slow etching region of Yamada et al., (1993)), the variation in the gap etching rate between different etching temperatures could explain the difference in observed HCT lengths.

4. Conclusive Remarks

Based on the assessment of factors documented in previous sections, it is found that following four factors affect the observed track length in zircon: namely, (1) anisotropy of track annealing and etching, (2) etching temperature, (3) track etching state and (4) width of measured HCT's. With considering the factor (1), the HCT's for a specific azimuth angle higher to *c*–axis should be used for analysis (see the Section 3–1). This is particularly important for both laboratory annealing experiments and borehole sample analysis because as temperature increases in these settings, angular distribution of HCT's significantly changes in accordance to the loss of accumulated damage derived from α–decay (Gleadow, 1981; Tagami et al., 1990). As a result of this, HCT's with higher angles to *c*–axis are selectively measured at an advanced stage of annealing, yielding apparent shortening of tracks. Although the cut–off angle is not necessarily definitive due to the transitional natures of both anisotropic etching and annealing of tracks, the angles over 60° to *c*–axis would be appropriate in regards of their patterns (Fig.1; see also Yamada et al., 1993; Hasebe et al., 1994).

Since the factor (2) significantly controls the measured HCT lengths in highly annealed zircon, it is needed to etch tracks at a specific temperature for a series of analysis. Alternatively, the influence of this factor could be corrected for with the help of Fig. 5. We prefer to etch sample at 248 ± 1°C for routine track length analysis. This temperature condition, close to the upper limit for PFA Teflon® sheets, provides a substantially shorter duration (~ 20%) to etch surface tracks than the conventional temperatures (e.g., 220°C; Gleadow et al., 1976).

The factor (3) is not effective where the factor (4) is treated rigorously. HCT's of exactly the same width can be selectively measured to analyse tracks of identical etching state. Alternatively, we can correct for the dependency of observed lengths on etch time by measuring the widths of HCT's as well. These procedures, however, are not suitable for routine experiments because they require either very large number of grains or laborious analysis, respectively. It should be more practical to set a looser measurement criterion on the HCT's width, e.g., 1 ± 0.5 μm, and also to control the etching state by the width of surface tracks (see the Section 3–5). Here it is noteworthy that the number of HCT's tends to increase as etching proceeds, particularly for intensively annealed zircons with high etching anisotropy due to the loss of accumulated α–decay damage. Thus the etching of zircon with 2 μm criterion yields more HCT's than that with the 1 μm criterion (Hasebe et al., 1994). In these regards, we adopt 1 ± 0.5 μm and 2 μm criteria for width of HCT's to be measured and width of surface tracks as an etching index, respectively, although these are not necessarily definitive values.

Finally, it should be noted that the effects of these factors are actually confirmed by

comparing the present results with the previously reported experiments with slightly different criteria or conditions. Thus the HCT length reduction pattern of spontaneous tracks in the present study was compared with that of Tagami et al. (1990), using the KT06 zircon, as shown in Fig. 11. Although the two results show similar patterns below ~ 600°C, their increasing departure is observed as temperature further elevates. Based on the similar chemical compositions of the two samples, the different factors between the two are etching temperature and criteria: 248°C and 2 μm in this study, whereas 221°C and 1 μm in Tagami et al. (1990). The combined effects of these two factors (Fig. 4 and 5) can reasonably explain the difference in Fig. 11. Note, however, that the mean HCT's lengths of KT06 were calculated for whole directions and thus may be slightly larger even after the correction than those for 60–90 azimuth angles. In addition, the sudden decrease in L/L_0 of KT06 between 450°C and 500°C might be resulted from the change of anisotropy in track angular distribution due to the loss of α–decay damage (see Tagami et al., 1990).

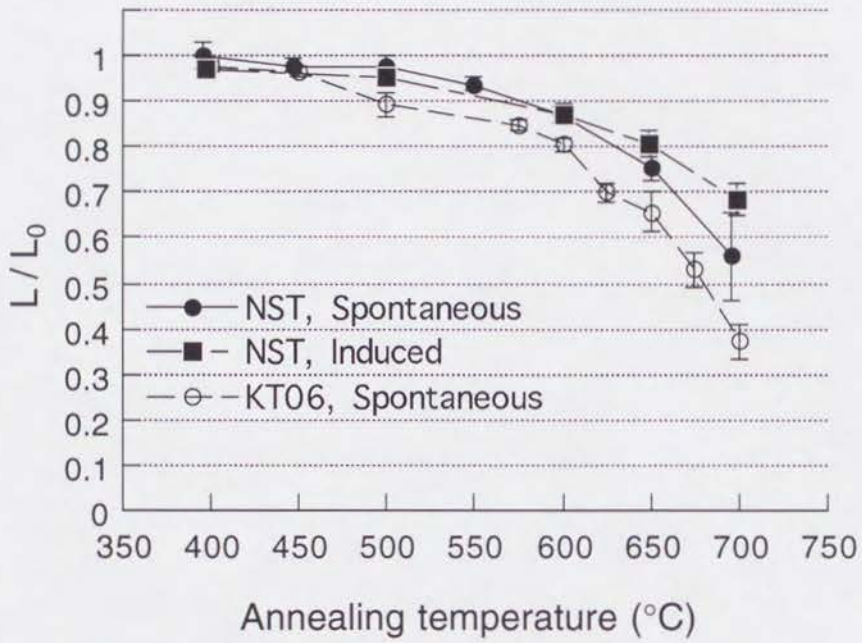

Fig. 11. Variation of spontaneous (*solid circles*) and induced (*solid squares*) track length in NST (this study), and variation of spontaneous track length in KT06 zircon (Tagami et al., 1990; *open circles*), during 1 h isochronal annealing. Lengths are normalized using the initial length of tracks (L_0) in unannealed samples. Etching criteria used are 2 μm (NST) and 1 μm (KT06), and etching temperatures were 248 ± 1°C (NST) and 221 ± 2°C (KT06), respectively. The mean lengths of NST are calculated using HCT's > 60° to crystallographic *c*–axis, whereas KT06 are of whole directions. Note the greater difference in spontaneous track length reductions between NST and KT06 where tracks are highly annealed. Error bars represent ± 2σ.

Acknowledgment

We thankfully acknowledge Prof. Andrew J.W. Gleadow and an anonymous person for reviewing the manuscript. We are grateful to Dr. Noriko Hasebe for thoughtful and helpful discussions on several points in the paper. Thanks are due to Prof. Takaaki Matsuda for suggesting the Nisatai Dacite sample, and Tetsu Yoshioka for helpful experimental assists. We also appreciate Rieko Arai and Ricardo Franco Nieto for improvements of the manuscript.

References

Corrigan, J., 1991. Inversion of apatite fission track data for thermal history information. J. Geophys. Research, 96: 10347–10360.

Deer, W. A., Howie, R. A. and Zussman, J., 1982. Rock–forming Minerals, Second edition, Volume 1A, Orthosilicates. Longman, London and New York., 418–442.

Donelick, R.A., 1991. Crystallographic orientation dependence of mean etchable fission track length in apatite: An empirical model and experimental observation. American Mineralogist. 76: 83–91.

Fleischer, R.L., Price, P.B. and Walker, R.M., 1975. Nuclear Tracks in Solids. University of California Press, Berkeley, Calif., 605 pp.

Gleadow, A.J.W., Hurford, A.J., and Quaife, R.D., 1976. Fission track dating of zircon: Improved etching techniques. Earth Planet. Sci. Lett., 33: 273–276.

Gleadow, A.J.W., 1981. Fission track dating methods: what are the real alternatives? Nucl. Tracks, 5: 3–14 .

Gleadow, A.J.W., Duddy, I.R. and Lovering, J.F., 1983. Fission track analysis: a new tool for the evaluation of thermal histories and hydrocarbon potential. Aust. Petrol. Explor. Assoc., 23: 93–102.

Gleadow, A.J.W., Duddy, I.R., Green, P.F. and Lovering, J.F., 1986a. Confined fission track lengths in apatite: a diagnostic tool for thermal history analysis. Contrib. Mineral. Petrol., 94: 405–415.

Gleadow, A.J.W., Duddy, I.R., Green, P.F. and Hegarty, K.A., 1986b. Fission track lengths in the apatite annealing zone and the interpretation of mixed ages. Earth Planet. Sci. Lett., 78: 245–254.

Green, P.F., Duddy, I.R., Gleadow, A.J.W., Tingate, P.R., and Laslett, G.M., 1986. Thermal annealing of fission tracks in apatite. 1. A Qualitative description. Chem. Geol., (Isot. Geosci. Sect.) 59: 237–253.

Green, P.F., Duddy, I.R., Laslett, G.M., Hegarty, K.A., Gleadow, A.J.W., and Lovering, J.F., 1989a. Thermal annealing of fission tracks in apatite. 4. Quantitative modeling techniques and extension to geological time scales. Chem. Geol. Isot. Geosci. Sec., 79: 155–182.

Green, P.F., Duddy, I. R., Gleadow, A.J.W., and Lovering, J.F., 1989b. Apatite fission–track analysis as a paleotemperature indicator for hydrocarbon exploration. In: N.D. Naeser and T.H. McCulloch (Editors), Thermal History of sedimentary Basins–

Methods and Case Histories. Springer, New York, NY., 181–195.

Hasebe, N., Tagami, T. and Nishimura, S., 1994. Towards zircon fission–track thermochronology: Reference framework for confined track length measurement. Chem. Geol., 110: 169–178.

Hirajima, T. and Banno, S., 1991. Electron–microprobe analysis of rock forming minerals with Kevex–Delta IV (Quantum Detector). Hitachi. Sci. Inst. News, 31: 3418–3423.

Kasuya, M and Naeser, C.W., 1988. The effect of α–damage of fission track annealing in zircon. Nucl. Tracks Radiat. Meas., 14" 477–480.

Lal, D., Rajan, R.S. and Tamhane, A.S., 1969. Chemical composition of nuclei of $Z > 22$ in cosmic rays using meteoritic minerals as detectors. Nature (London), 221: 33–37.

Laslett, G.M., Kendall, W.S., Gleadow, A.J.W. and Duddy, I. R., 1982. Bias in measurement of fission–track length distributions. Nucl. Tracks, 6:79–85.

Laslett, G.M. and Gleadow, A.J.W., 1984. The relationship between fission track length and track density in apatite. Nucl. Tracks, 9: 29–38 .

Paul, T.A. and Fitzgerald, P.G., 1992. Transmission electron microscopic investigation of fission tracks in fluorapatite. American Mineralogist. 77: 336–344.

Sumii, T., Tagami, T. and Nishimura, S., 1987. Anisotropic etching character of spontaneous fission tracks in zircon. Nucl. Tracks Radiat. Meas., 13: 275–277.

Suzuki, K. and Yogo, S., 1986. Microprobe analyses of zircons in some granitic rocks with special reference to the distribution of uranium. Bull. Nagoya Univ. Museum., 2: 27–53.

Tagami, T., Ito, H., and Nishimura, S., 1990. Thermal annealing characteristics of spontaneous fission tracks in zircon. Chem. Geol. Isot. Geosci. Sec. 80: 159–169.

Tagami, T., Uto, K., Matsuda, T., Hasebe, N. and Matsumoto, A., 1995. K–Ar biotite and fission–track zircon age of the Nisatai Dacite, Iwate Prefecture, Japan: A candidate for an age standard. Geochem. J. 29: 207–211.

Yamada, R., Tagami, T. and Nishimura, S., 1993. Assessment of overetching factor for confined fission–track length measurement in zircon. Chem. Geol. 104: 251–259.

Part II: Annealing Kinetics of Fission Track in Zircon: An Experimental Study

[1]Ryuji YAMADA, [1]Takahiro TAGAMI, [1]Susumu NISHIMURA and [2]Hisatoshi ITO

[1]*Department of Geology and Mineralogy, Faculty of Science, Kyoto University, Kyoto 606–01, Japan*

[2]*Central Research Institute of Electric Power Industry, 1646 Abiko 270–11, Japan*

CHEMICAL GEOLOGY (Isotope Geoscience), 122: 249–258.

(Submitted April 5, 1994: revised and accepted January 12, 1995)

Abstract

A series of laboratory annealing experiments of zircon fission–track has been carried out in heating conditions at 350–750°C for 10^{-1}–10^{3} h (i.e., 4.5 min.– ~ 40 days). Variation in the confined lengths of spontaneous fission tracks was determined using zircon grains from the Nisatai Dacite. The fading contours of normalized mean track length (r) on the Arrhenius diagram showed as sets of straight lines. We performed a series of model fittings, called the parallel and fanning models, in order to describe the decrease in r with increasing temperature or heating time. The lowest temperature limit of the zircon partial annealing zone (ZPAZ) was defined as $r \sim 0.95$, and the highest as $r \sim 0.4$, which approximately corresponded to the total fading of surface tracks. Extrapolation of the results of the laboratory experiments to geological time scale gives estimated values of the ZPAZ: ~ 210–320°C (± 60°C, 2σ) on the parallel model and ~ 170–390°C (± 50°C, 2σ) on the fanning model for the heating duration of 10 m.y. The temperatures of ZPAZ decrease ~ 20°C for a magnitude of longer annealing duration. Since the estimated closure temperature of zircon fission–track analysis approximately corresponds to the middle of ZPAZ, these results support previously estimated closure temperature of ~ 240°C. By varying etching time, it was revealed that the removal of alpha–radiation damage occurs drastically at $r \sim 0.93$.

1. Introduction

The latent fission tracks (FTs) in minerals are annealed with increasing temperature, and the analysis of fossil FTs accumulated for geologic periods provides useful information of a rock's thermal history. Quantitative analysis of track fading on a geological time scale enables the reliable estimation of thermal histories. The fading of FTs is characterized on the reduction of both track density and length; especially the lengths of horizontal confined tracks (HCT's; Laslett et al., 1982) offer an accurate parameter with minimum experimental biases. On the basis of both laboratory and geological annealing data, quantitative analysis of the thermal history has been achieved using observed apatite fission track (FT) parameters (e.g., Green et al., 1989).

In the case of zircon, however, potential difficulties have been recognized on laboratory FT annealing experiments. Gleadow (1978) found that accumulated alpha–radiation damage in the mineral is reduced during annealing. This annealing process accordingly increases the anisotropy in the procedure of track etching and can result in an apparent reduction of track etching efficiency. Tagami et al. (1990) successfully corrected the effects of varying etching anisotropy on observed track density during annealing with measuring angular distribution of etched tracks. Additionally, the effect of overetching is anisotropic and variable for different crystallographic directions according to highly anisotropic etching characteristics. Yamada et al. (1993) precisely assessed this effect for reliable track length analysis. A reference framework of HCT length measurement in zircon was established focusing on the angular distribution of length and number of HCT's (Hasebe et al., 1993). It is known that various factors control the observed and measured lengths of annealed FTs (Laslett et al., 1982, 1984; Tagami et al., 1990). Yamada et al. (1995) assessed the factors affecting the paleotemperature estimate, and recommended the realistic experimental criteria for routine HCT length measurements.

In order to estimate quantitatively the thermal histories using zircon FT length analysis, we here report data sets of Arrhenius–plot experiments in laboratory. Based on the experimental criteria proposed by Yamada et al. (1995), track annealing experiments were carried out at 350 –750°C for 10^{-1}–10^{3} h (i.e., 4.5 min.– ~ 40 days). The data were fitted by mathematical models that describe the reduction of etched length as a function of time and temperature. We used both the parallel and fanning models (e.g., Laslett et al., 1987) for calculation, and estimated the temperatures of zircon partial annealing zone (ZPAZ) for geological time scale on the order of 10^{6}–10^{8} yr.

2. Sample and Experimental Methods

Zircon samples used in this study, named NST, were separated from a dacitic welded tuff of the Nisatai Dacite, occurring in the northern part of Kitakami mountain range, northeast Japan. The NST has been dated as K–Ar biotite age of 20.6 ± 0.5 (1σ) Ma and counted as its spontaneous track density of ~ $4 \cdot 10^6$ cm^{-2} (Tagami et al., 1995). The zircon crystals are euhedral and clear so that their crystallographic *c*–axes are readily determinable, and the variation of their uranium content is small. Their spontaneous tracks are not geologically annealed after their deposition, as confirmed by the concordance between the spontaneous and induced track lengths (11.05 ± 0.08 (1σ) μm and 11.03 ± 0.10 μm, respectively; see Table 1).

After mineral separation using conventional heavy liquid and magnetic separation techniques, some of the zircon grains were heated at 1009 ± 2°C for 2 h in order to remove all spontaneous tracks therein. They were irradiated for 30 min. at the Thermal Column Pneumatic Tube (Tc–Pn) facility of Kyoto University Research Reactor (KUR–1). This produced an induced track density of ~ $6 \cdot 10^6$ cm^{-2}. Annealing experiments were performed for 10^{-1}–10^3 h (i.e., 4.5 min.– ~ 40 days) at temperatures ranging from 350 to 750°C (Table 1). About 150 ~ 300 zircon grains were mounted in polytetrafluorethylene–perfluoroalkoxyethlene (PFA) Teflon® sheets and their external prismatic surfaces were ground and polished. Spontaneous and induced tracks used for analysis were etched in NaOH–KOH eutectic etchant (Gleadow et al., 1976) at 250 ± 1°C until the surface tracks perpendicular to *c*–axes attained the width of 2 μm (Yamada et al., 1995).

Track lengths were measured for horizontal confined tracks (HCT's; Laslett et al., 1982) throughout this study, containing both track–in–tracks and track–in–cleavages (TINT's and TINCLE's, respectively; Lal et al., 1969). HCT's with widths of 1 ± 0.5 μm were selectively measured to minimize the overetching effect (cf. Yamada et al., 1993). The lengths of HCT's were measured using a digitizing tablet interfaced with the Hamamatsu® C2500 Image Processing System, combined with a Nikon® Biophot microscope. For a 100x dry objective and 10x eyepieces, which result in a true measured magnification of 925x, the systematical errors for the measurement of track length is ~ 0.1 μm. All grains in a mount were scanned with the help of a Sapporo® Micro Scanner automatic scanning stage installed to Biophot microscope. The orientations of HCT's were measured as angles to the crystallographic *c*–axis with a precision of ~ ± 1° using C2500 system. Length and orientation data of individual tracks, together with their figures, were recorded on the video copies printed by the Mitsubishi® Video Copy Processor SCT–P75 interfaced with the Hamamatsu® C2500.

3. FT Annealing and the Arrhenius Plot

The analytical data of laboratory annealing experiments performed in various time–temperature conditions are listed in Table 1. Fig. 1 shows the relationship between annealing temperature and confined track length of isochronal annealing experiments using spontaneous (~ 10^{-1}–10^{3} h) and induced (1 h) tracks of samples. There is no significant difference in how length reduction occurs among heating temperatures or between spontaneous and induced tracks: with the elevation of annealing temperature, the mean track length is first gradually reduced, then drastically.

Track length distribution patterns of 1 h isochronal annealing experiments are shown in Fig. 2. All diagrams for annealing below 599°C show unimodal and narrow patterns (a–f), whilst those for 650°C and 696°C show broader patterns (g, h). It might be considered that this widening of distributions accompanied with the sudden increase in standard deviation (see Yamada et al., 1995; Fig. 10: This plot is reproducible by plotting *sd* versus *r* in Table 1 with some additional data) is due to anisotropy in the length distribution. However, the data of the cited plot are of tracks with the angles to the *c*–axis >60°, and thus the effect of the anisotropy in the length distribution is almost eliminated. Since the sudden increase in standard deviation is recognized even after reducing the effect of anisotropy, this widening of distributions is explainable with the existence of the gap zones along the length of tracks found at highly annealed stages (Yamada et al., 1995). The gap zones may also cause curvilinear characters at higher annealing temperature recognized in the plot of Fig. 1.

Results for spontaneous HCT's annealing in Table 1 are shown on an Arrhenius plot in Fig. 3. HCT's with the angles to the crystallographic *c*–axis >60° are selectively used for analysis hereafter, considering the various orientation factors which affect the track length measurement (Yamada et al., 1993, 1995). The normalized track length (*r*) values in a certain range are represented by the same symbol. They present linear trends with a positive correlation in the plot. In order to extrapolate the results of laboratory annealing experiments to the geological time scale, two types of model fitting have traditionally been performed on an Arrhenius plot to determine the functional form for the FT annealing process, called 'parallel model' and 'fanning model' (e.g., Laslett et al., 1987). Furthermore, there are some detailed treatments dividing the functional forms into 'linear' and 'curvilinear' models, according to the description of temperature function: They indicate that the fading contours in the Arrhenius plot are 'linear' and 'curvilinear' in shape, respectively (e.g., Laslett et al., 1987; Crowley et al., 1991). Here we adopted 'linear model', which is commonly used for the discussion of Arrhenius law.

Table 1. Analytical data of FT annealing experiments of NST zircon. In the row of '*t*', S_0 and I_0 indicate unannealed samples. Mean lengths of tracks >60° (L) of S_0 and I_0 are determined as L_s and L_i, respectively (underlined). Values in [] are the maximum length of surface tracks, which are roughly estimated with the micrometer attached with an eyepiece of the microscope.

t	*T*	t_e	N_{all}	*N*	L_{all}	*L*	*sd*	*se*	*r*
Spontaneous									
S_0	*	22	107	65	11.14	<u>11.05</u>	0.65	0.08	*
4.5 min.	500	22	51	34	10.85	10.78	0.65	0.11	0.98
	600	26	50	38	10.25	10.11	0.60	0.10	0.92
	650	26	50	37	9.29	9.26	0.63	0.10	0.84
	700	26	50	36	8.41	8.40	0.79	0.13	0.76
	750	26	2	2	7.07	7.07	0.27	0.19	0.64
1 h	395	22	53	32	10.85	10.83	0.89	0.16	0.98
	446	21	53	37	10.73	10.60	0.51	0.08	0.96
	500	22	50	35	10.67	10.57	0.73	0.12	0.96
	550	22	50	39	10.18	10.16	0.58	0.09	0.92
	599	26	50	40	9.56	9.47	0.62	0.10	0.86
	650	26	50	32	8.55	8.20	0.93	0.16	0.74
	696	26	15	9	6.38	6.08	1.57	0.52	0.55
	748	26	0	0	[~ 4]	–	–	–	–
11 h	397	22	50	28	10.96	10.89	0.64	0.12	0.99
	499	26	50	30	10.20	10.13	0.60	0.11	0.92
	548	26	50	35	9.42	9.26	0.76	0.13	0.84
	598	26	40	30	7.80	7.74	0.71	0.13	0.70
	649	26	0	0	[~ 6]	–	–	–	–
100 h	350	22	50	35	10.83	10.79	0.70	0.12	0.98
	449	24	51	32	10.23	10.12	0.75	0.13	0.92
	501	26	50	36	9.37	9.20	0.73	0.12	0.83
	549	26	50	27	8.23	8.10	0.68	0.13	0.73
	599	26	6	3	7.24	6.73	1.33	0.77	0.61
1000 h	398	26	48	33	10.46	10.27	0.55	0.10	0.93
	450	26	51	42	9.58	9.48	0.71	0.11	0.86
	498	26	51	41	8.61	8.59	0.72	0.11	0.78
	535	26	12	10	7.14	7.11	1.16	0.37	0.64
	546	26	0	0	[~ 6]	–	–	–	–
Induced									
I_0	*	26	59	48	11.04	<u>11.03</u>	0.72	0.10	*
1 h	397	26	51	40	10.81	10.75	0.57	0.09	0.97
	500	26	50	39	10.56	10.51	0.71	0.11	0.95
	600	26	50	42	9.74	9.64	0.89	0.14	0.87
	649	26	50	35	8.96	8.92	0.94	0.16	0.81
	698	26	50	31	7.85	7.57	1.04	0.19	0.69
	748	26	0	0	[~ 4]	–	–	–	–
	795	26	0	0	[~ 0]	–	–	–	–

t=annealing duration; *T*=annealing temperature (°C); t_e=etching time (h); N_{all}=number of all measured tracks; *N*=number of measured tracks >60° to crystallographic *c*–axis; L_{all}=mean length of all measured tracks (μm); *L*=mean length of tracks >60° (μm); *sd*=standard deviation for the length distribution of tracks >60° (μm); *se*=standard error of *L* (μm); *r*=normalized value of *L* by L_s (spontaneous tracks) and L_i (induced), respectively.

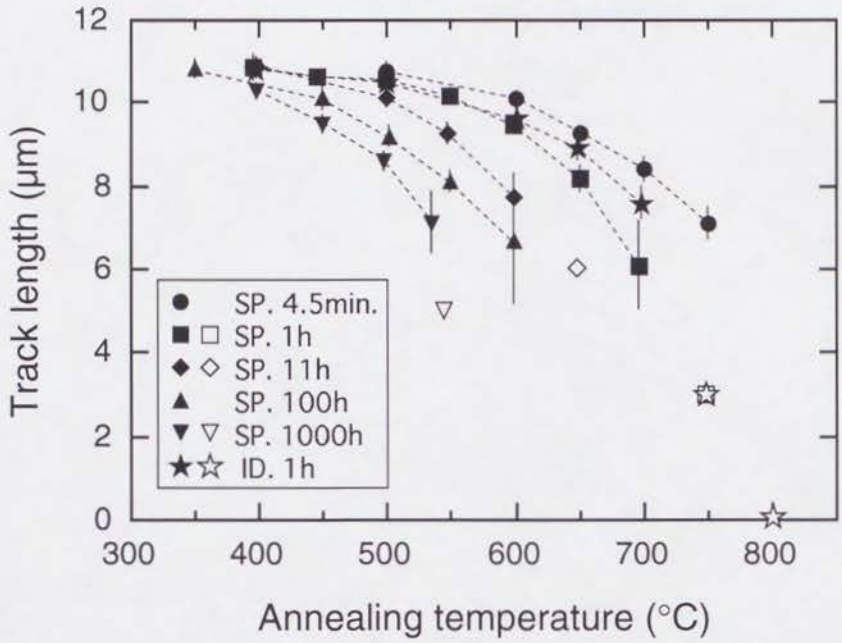

Fig. 1. Length reduction characters of horizontal confined tracks (HCT) against annealing temperatures for spontaneous and induced tracks. Solid symbols represent runs used for analysis, and open symbols represent runs not used for analysis, which are unreliable or roughly estimated value (see the Section 3.1 and Table 1). 'SP.' and 'ID.' in the legend column indicate spontaneous and induced samples, respectively. *Error bars* represent 2σ.

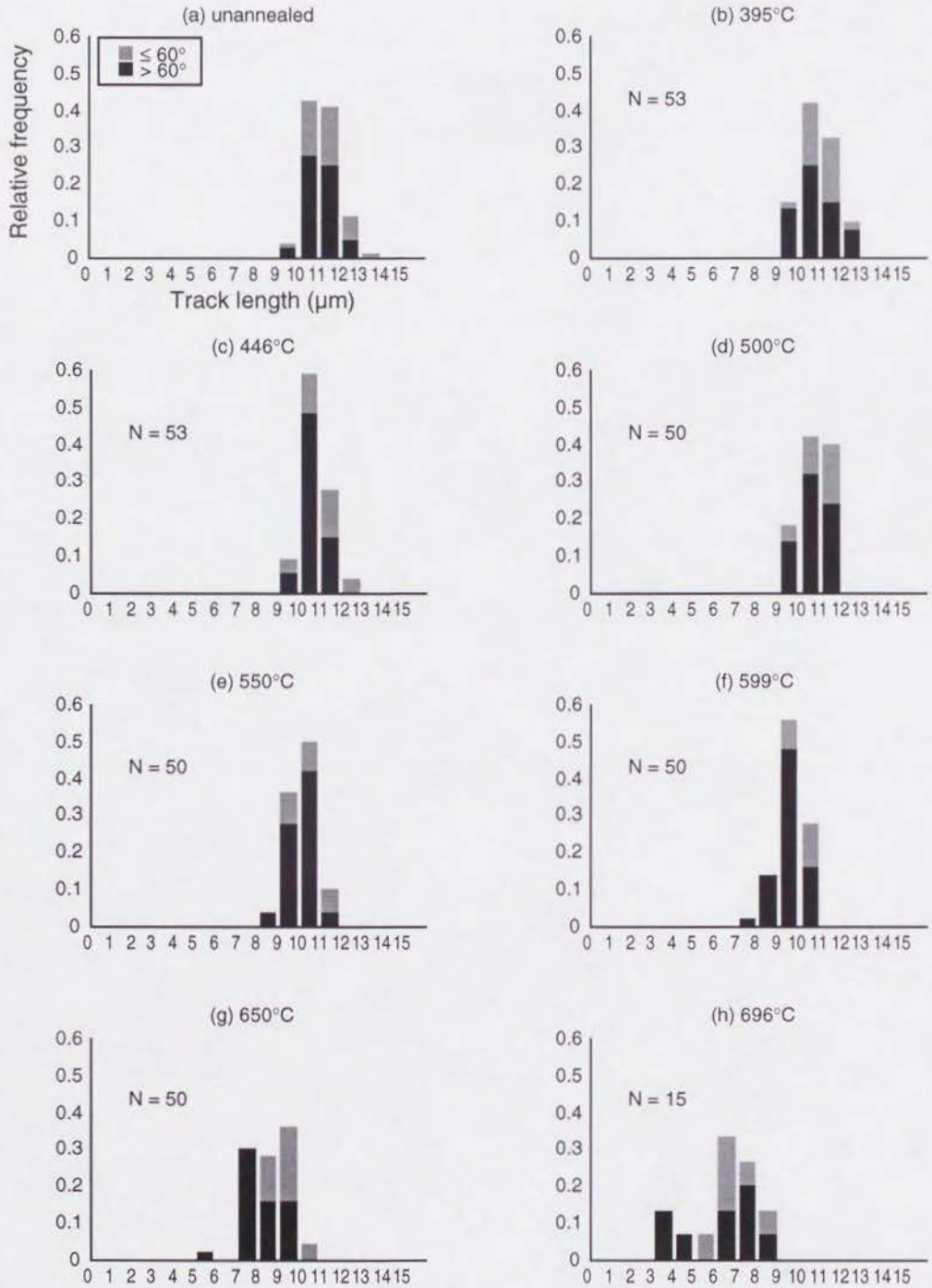

Fig. 2. Track length distribution patterns of 1 h isochronal annealing experiments with various temperatures. Vertical axes indicate the relative frequencies of the number of tracks summed in each 1 μm interval. In these diagrams, solid parts of the bars are of tracks with angles to the crystallographic *c*–axis > 60°, and hatched are of those ≤ 60°.

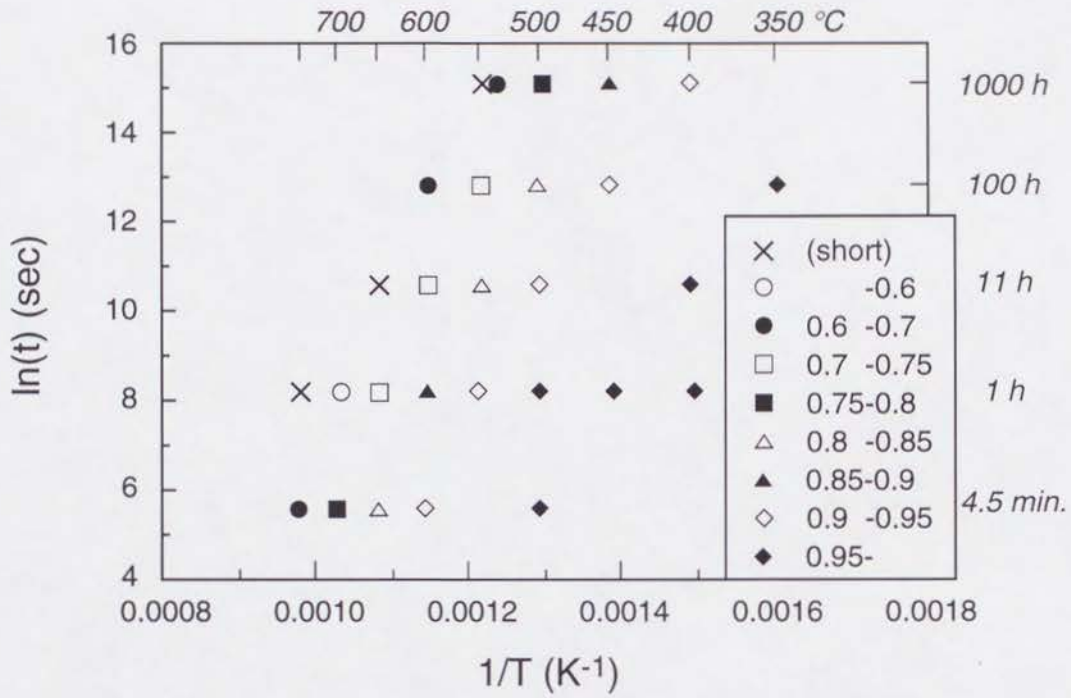

Fig. 3. Arrhenius plot of the experimental data (see Table 1), using spontaneous FTs. Each point corresponds to one annealing experiment. Different degrees of length reduction (r) are shown with different symbols. Cross symbols indicate time and temperature conditions where tracks were short so that no HCT's could be found.

3–1. Parallel Model Fitting

Fitting procedures adopted were fundamentally after the model calculation of FT annealing in apatite (Laslett et al., 1987; Crowley et al., 1991).

As a first step to determine the functional form for the FT annealing process, we suppose the parallel Arrhenius plot with straight–line contours. Parallel lines on an Arrhenius plot is expressed as follows;

$$\ln(t) = A(r) + B / T \tag{1}$$

where t = annealing time, T = annealing temperature (K), $A(r)$ = intercept of the lines (at $1/T = 0$), which is a function of the most reliable values of normalized mean length r, and B is the slope, which is constant. The intercept $A(r)$ is subject to the following constraints: (1) $A(r)$ decreases monotonically with increasing r, and (2) $A(r = 1) \rightarrow -\infty$ when $t \rightarrow 0$, $T \rightarrow 0$. It should be noted that $r = 0$ for finite values of t and T provided they are large enough, in practice.

The fully parameterized parallel model has the form

$$g(r\,;\,a, b) = c_1 + c_2\,A(r) + \varepsilon = c_1 + c_2\,(\ln(t) - B / T) + \varepsilon \tag{2}$$

or

$$g(r\,;\,a, b) = C_0 + C_1 \ln(t) + C_2 / T + \varepsilon \tag{3}$$

where $C_0 = c_1$, $C_1 = c_2$, $C_2 = -c_2 B$ and $g(r\,;\,a, b)$ is a transform containing r and two parameters a and b, and ε represents the errors or residuals. ε is assumed to be normally distributed with mean $\mu = 0$ and constant variance σ^2. This assumption can be checked by residual plots for each model (Fig. 5). We adopted the Box and Cox (1964) type transformation for $g(r\,;\,a, b)$:

$$g(r\,;\,a, b) = (((1 - r^{\,b}) / b)^a - 1) / a \tag{4}$$

where $0 < r < 1$. For the fitting procedure, the maximum likelihood method was used (Box and Cox, 1964). Parameters were obtained by maximizing the log–likelihood function:

$$L^* = -N \ln(ss) / 2 + \sum_{j=1}^{N} \ln |\, g'(r_i\,;\,a, b)| \tag{5}$$

where N is the number of data points, $|\,|$ denotes absolute value, ' denotes differentiation with respect to r, and the variance ss,

$$ss = (1 / N) \sum_{j=1}^{N} [\,\hat{g}(r_i) - g(r_i)]^2 \tag{6}$$

is the residual sums of square divided by the number of data points. We chose all the data set in Table 1 for fitting calculation, except one data set (i.e., 4.5 min., 750°C; this exceptional one

was neglected for the analyses since its standard deviation is extraordinarily small for the number of measured tracks). Therefore, $N = 24$. In the model of Eq. 3, parameters and uncertainties (2 standard errors) were evaluated for data sets in Table 1 as follows;

$$a = -0.059,\ b = -0.678,\ C_0 = 6.306(478),\ C_1 = 0.2757(522)$$
$$\text{and } C_2 = -8988(352) \tag{7}$$

and thus

$$B = -C_2 / C_1 = 32600(6300). \tag{8}$$

3–2. Fanning Model Fitting

Green et al. (1988) claim that fission track annealing in apatite cannot be described by first–order kinetics and a 'slightly fanning' Arrhenius plot gives a significantly better fit than the parallel model. On a fanning Arrhenius plot, the slopes of contour lines change with the variation of activation energy E with degree of annealing. In such case, the Eq. 1 becomes:

$$\ln(t) = A(r) + B(r) / T, \tag{9}$$

where both the slope $B(r)$ and intercept $A(r)$ are function of r. To simplify this equation, we make a first–order assumption that $A(r)$ is a negative linear function of $B(r)$:

$$A(r) = c_3 - c_4 B(r), \tag{10}$$

where c_3 and c_4 are constants, by analogy with the 'compensation law' for diffusion (e.g., Winchell, 1969; Hart, 1981). This produces the fading contours meeting at a single point on the Arrhenius plot, as assumed in previous works (e.g., Laslett et al. 1987). Combining Eq. 9 and Eq. 10 yields

$$\ln(t) = A^* + B(r) [(1 / T) - (1 / T_0)], \tag{11}$$

where $A^* = c_3$ and $1/T_0 = c_4$. T_0 is called as 'critical temperature', which is the temperature of the 'crossover point' of fading contours (e.g., Winchell, 1969; Crowley et al., 1991). Solving Eq. 11 for $B(r)$ gives

$$B(r) = (\ln(t) - A^*) / [(1 / T) - (1 / T_0)] \tag{12}$$

There arise some constraints for the slope $B(r)$ as follows: (1) $B(r)$ decreases monotonically with increasing r, and (2) $B(r=1) \rightarrow 0$ when $\ln(t) \rightarrow A^*$, $T \rightarrow 0$. The fully parameterized model is given by

$$g(r\,;\, a, b) = c_1 + c_2 B(r) = c_1 + c_2 \{(\ln(t) - A^*) / [(1 / T) - (1 / T_0)]\} + \varepsilon \tag{13}$$

or

$$g(r\,;\, a, b) = C_0 + (C_1 \ln(t) + C_2) / [(1 / T) - C_3] + \varepsilon \tag{14}$$

where $C_0 = c_1$, $C_1 = c_2$, $C_2 = -c_2 A^*$ and $C_3 = 1 / T_0$.

Assuming an infinite critical temperature ($T_0 = \infty$), Eq. 14 is arranged to

$$g(r\,;\, a, b) = C_0 + C_1 T \ln(t) + C_2 T + \varepsilon \tag{15}$$

The number of parameters to be estimated is reduced from six to five, and thus the equation is simplified. This equation corresponds to the 'fanning model' of Laslett et al, (1987). In the model of Eq. 15, the parameters and uncertainties were evaluated as follows;

$$a = 0.140,\ b = 0.371,\ C_0 = -8.871(250),\ C_1 = 0.0002163(363),$$

$$\text{and } C_2 = 0.006625(338) \qquad (16)$$

In the case of $T_0 \neq \infty$, Eq. 14 was adopted for fitting calculation. The parameters and uncertainties were evaluated as follows;

$$a = 0.245,\ b = -0.267,\ C_0 = -4.554(198),\ C_1 = 0.00009330(1429),$$

$$C_2 = 0.0008482(1362) \text{ and } C_3 = 0.0006382(563) \qquad (17)$$

An estimate of critical temperature can be obtained from the parameter C_3 in Eq. 17

$$\hat{T}_0 = 1294°C\ (1167°C / 1456°C) \qquad (18)$$

Crowley et al. (1991) obtained the estimates of the critical temperatures as $523°C \leq \hat{T}_0 \leq 957°C$, for the case of fission track annealing in fluorapatite and Sr–fluorapatite.

The Arrhenius plot with fitting lines of fanning model for the case of Eq. 15 and Eq. 14 are shown in Fig. 4(b) and (c) using the obtained parameters. Residual plots for each fit to the parallel and fanning models are shown in Fig. 5, and also the maximum likelihoods and coefficients of determination (R^2) are shown in Table 2. R^2 is calculated as 1–(RSSQ / TSSQ), where RSSQ is the residual sums of squares and TSSQ is the total sums of squares for the untransformed variable r. The residual plots indicate that parameters obtained for these fitting models satisfy the assumption of the errors to be normally distributed with mean $\mu = 0$ and constant variance σ^2. According to maximum likelihoods, coefficients of determination and residual plots, experimental data are best described by the fanning model ($T_0 \neq 0$; Eq. 14), among these three models.

Considering the existence of gap zones along tracks found in rather highly annealed stage (e.g., Paul and Fitzgerald, 1992; Yamada et al., 1995), it might not be reasonable to describe monotonously the reduction of etchable and observable track length using a single crossover point. Further ameliorating model, which is constructed considering the physical phenomena of track segmentation during thermal annealing, would possibly yield better fitting of the experimental data and allow the reliable extrapolation of ZPAZ estimates in geological conditions.

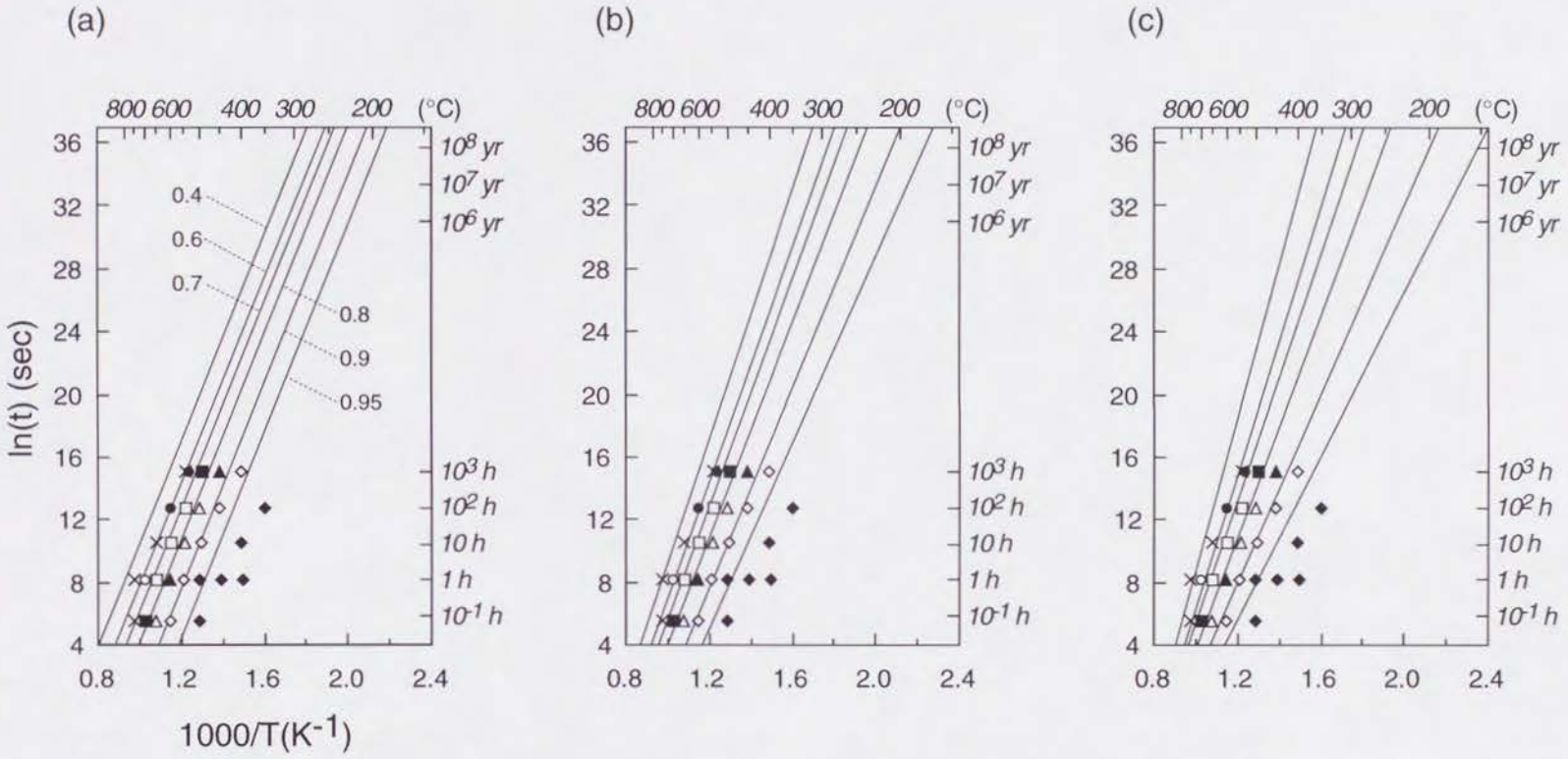

Fig. 4. Arrhenius plots with fitting lines extrapolated to geological time condition; (a) parallel model, (b) fanning model ($T_0 = \infty$), (c) fanning model ($T_0 \neq \infty$). They are obtained by adopting the pairs of the equation and parameters of (a); (3, 7), (b); (15, 16) and (c); (14, 17), respectively (see text). Values of normalized mean length (r) for each fading contours are indicated in (a), ranging from 0.4 to 0.95. *Symbols* are the same as those in Fig. 3.

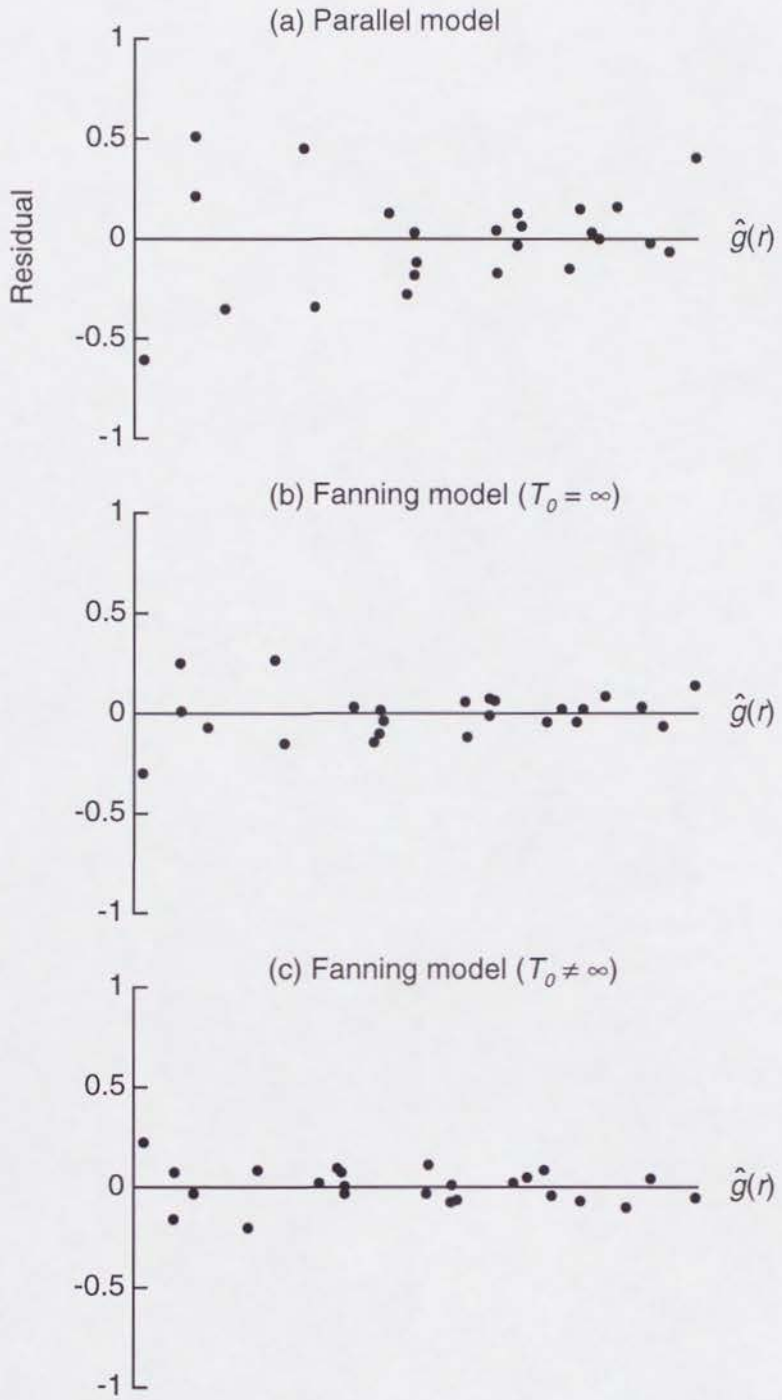

Fig. 5. Residual plots for the best fitting equations for each model (ε in Eqs. 3, 15, and 14). Each point represents one annealing experiment. (a) parallel model, (b) fanning model ($T_0 = \infty$), (c) fanning model ($T_0 \neq \infty$).

4. The Estimation of ZPAZ

The geologic temperature ranges of ZPAZ were calculated by extrapolating model equations to geological time scale with parameters derived from annealing experiments on spontaneous FTs. The assumption of such extrapolations is that the track annealing process is the same physical phenomena both in laboratory and natural conditions. Although the time–temperature extrapolation is not yet completely justified since the accumulated alpha–radiation damage (cf., Section 5) or other factors than those studied in the laboratory can also play a role, this assumption can be supported by two factors: (1) The validity of such extrapolation was previously confirmed for annealing in apatite by the concordance between the prediction from laboratory results and the observation in natural borehole samples (e.g., Green et al., 1989). (2) In a recent FT study on the thermal influence of the granitic intrusion on country sediments (Tagami et al., 1996), the track length reduction pattern was found to be similar to that in laboratory heating (Fig. 2). In addition, the presence of gap zones in tracks of zircon (Yamada et al., 1995) were recognized in the highly annealed stage of geologic heating. These facts suggest that the same physical processes of annealing are active regardless of the annealing rate.

We here define the lowest temperature limit of ZPAZ as $r \sim 0.95$, since the track length reduction at 5% level (~ 0.5 μm) may be detectable using the widespread track length measurement systems. The highest is defined as $r \sim 0.4$, which approximately corresponds to the total fading of surface tracks (e.g., 1 h, 748°C). On the Arrhenius diagram of Fig 4, the range of ZPAZ are shown between the contour lines corresponding to $r \sim 0.95$ and 0.4. ZPAZ are accordingly calculated by extrapolating with the parallel and fanning model equations (Eq. 3, 15 and 14, respectively) to the geological time scale, as listed in Table 2. Our data set yield estimates of ZPAZ for the heating duration of 10^7 y: ~ 207–315°C with parallel model, ~ 192–350°C with fanning model ($T_0 = \infty$), and ~ 170–393°C with fanning model ($T_0 \neq \infty$). The uncertainties of estimated temperatures are ~ 50–70°C for each experiment (2 standard errors). The temperatures of ZPAZ decrease ~ 20°C for a magnitude of longer heating duration. Of these three estimates of ZPAZ range, the most plausible one is 170–393°C with fanning model ($T_0 \neq \infty$) according to the likelihoods and/or coefficients of determination. It should be noted that these temperatures are variable due to the definition of ZPAZ range. The closure temperature (T_c) of zircon fission–track analysis shows a significant discrepancy among literature: from ~ 175°C (e.g., Harrison et al., 1979) to ~ 240°C (e.g., Hurford, 1986). Because T_c approximately corresponds to the middle of ZPAZ, the present results support the higher value.

In the Arrhenius plot, the slope B is normally described in terms of an activation energy, given by E/k, where k is Boltzmann's constant. For the case of parallel model, the apparent activation energy was obtained as 2.81 eV, using parameters of Eq. 6. This derived value is

Table 2. Results of the Model Fitting Calculations.

Arrhenius model		Parallel model	Fanning model ($T_0 = \infty$)	Fanning model ($T_0 \neq \infty$)
Model equation		$g(r\,;a,b) = C_0+C_1\,ln(t)+C_2/T$	$g(r\,;a,b) = C_0+C_1\,T\,ln(t)+C_2T$	$g(r\,;a,b) = C_0+(C_1\,ln(t)+C_2)\,/\,[(1/T)-C_3]$
Maximum likelihood		93.3	98.8	101.4
Coefficients of determination (R^2)		0.911	0.980	0.988
Bottom of ZPAZ (2σ)				(°C)
H.D. =	10^6 y	223.5(50.3)	209.1(46.4)	187.9(49.6)
	10^7 y	206.7(49.9)	191.7(45.8)	170.0(48.6)
	10^8 y	191.0(49.6)	175.6(45.2)	153.4(47.7)
Top of ZPAZ (2σ)				
H.D. =	10^6 y	341.0(76.0)	373.0(59.9)	414.5(57.2)
	10^7 y	315.5(73.4)	349.8(59.3)	393.1(56.5)
	10^8 y	292.0(71.8)	328.1(58.6)	373.0(55.9)

(H.D.; heating duration)

concordant with these previously reported, i.e., ~ 2.5 eV (Fleischer et al., 1965) and 1.7 ~ 2.9 eV (Nishida and Takashima, 1975): the former was calculated by reduction of track density, and the latter was by that of track length.

5. Removal of α–radiation Damage

Natural zircon crystals are more or less suffered metamictization mainly from the accumulation of alpha–recoil damages from uranium atoms therein. This accumulating radiation damage has a major effect on the fission track etching properties of the mineral: decrease in etching time and reduction of etching anisotropy (Gleadow, 1978, 1981). According to Tagami et al. (1990), the accumulated alpha–radiation damage is completely removed between 450 and 500°C.

The relationship between r and etching time to pass the 2 μm etching criteria in this study is shown in Fig. 6. The etching time changes significantly at $r \sim 0.93$ with a consistent trend for the various annealing experiments. This suggests that the removal of accumulated alpha–radiation damage may be correlated to the degree of annealing, and data sets with $r < \sim 0.93$ would not be affected by alpha–damage. It should be noted that the temperatures of alpha–damage removal is clearly different between the result in this study (i.e., 550–600°C, 1 h annealing) and that of Tagami et al. (1990) (i.e., 450–500°C, 1 h), implying the temperature of alpha–damage removal is dependent of some sample characteristics. Since the change in etching time was drastic, not gradual for various annealing runs, the activation energy of alpha–damage removal might be similar to that of fission track annealing.

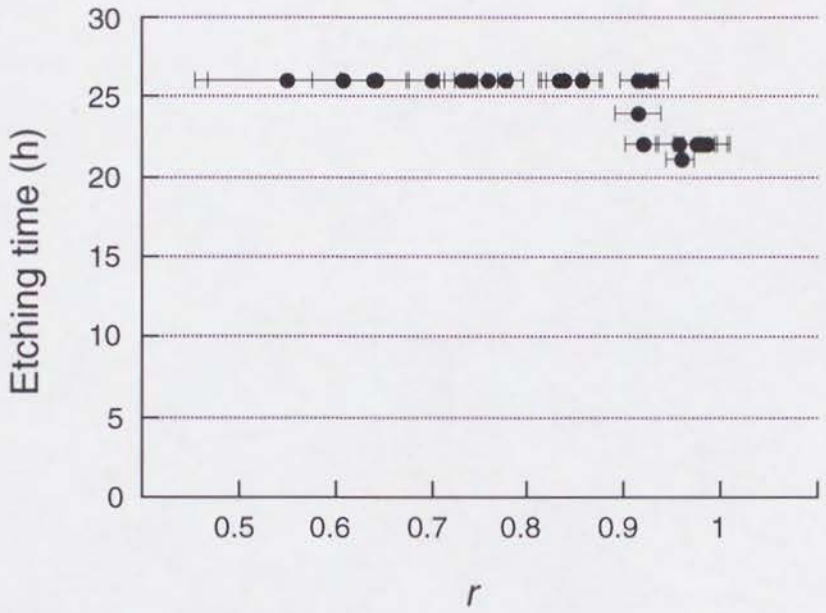

Fig. 6. Relationship between etching time and normalized track length (r). Each point represents one annealing experiment. Note the significant change in etching time at $r \sim 0.93$, reflecting the loss of accumulated alpha-radiation damage. *Error bars* represent 2σ.

Acknowledgment

We are grateful to Drs. Gunter A. Wagner, Paul F. Green, Geoff M. Laslett, and an anonymous person for reviewing the manuscript. We thank Dr. Noriko Hasebe for valuable advice on the experiments. We also appreciate Rieko Arai for improvements of the manuscript. Thanks are due to Dr. Takaaki Matsuda for suggesting the Nisatai Dacite sample, and to Tetsu Yoshioka for experimental assistance. This work has been performed using facilities of the Research Reactor Institute, Kyoto University.

References

Box, G. E. P. and Cox, D. R., 1964. An analysis of transformations. J. Roy. Stat. Soc., Ser. B 26: 211–252.

Burchart, J., Butkiewicz, T., Dakowski, M. and Galazka–Friedman, J., 1979. Fission track retention in minerals as a function of heating time during isothermal experiments: A discussion. Nucl. Tracks, 3: 109–117.

Crowley, K.D., Cameron, M., Schaefer, R.L., 1991. Experimental studies of annealing of etched fission tracks in fluorapatite. Geochim. Cosmochim. Acta, 55: 1449–1465.

Fleischer, R. L., Price, P. B. and Walker, R. M., 1965. Effects of temperature, pressure and ionization of the formation and stability of fission tracks in minerals and glasses. J. Geophys. Res., 70: 1497–1582.

Gleadow, A.J.W., 1978. Anisotropic and variable track etching characteristics in natural sphenes. Nucl. Tracks, 2: 105–117.

Gleadow, A.J.W., 1981. Fission track dating methods: what are the real alternatives? Nucl. Tracks, 5: 3–14.

Gleadow, A.J.W., Hurford, A.J. and Quaife, R.D., 1976. Fission track dating of zircon: Improved etching techniques. Earth Planet. Sci. Lett., 33: 273–276.

Green, P.F., Duddy, I.R. and Laslett, G.M., 1988. Can fission track annealing in apatite be described by first–order kinetics? Earth Planet. Sci Lett., 87: 216–228.

Green, P.F., Duddy, I.R., Gleadow, A.J.W. and Lovering, J.F., 1989. Apatite fission–track analysis as a paleotemperature indicator for hydrocarbon exploration. In: N.D. Naeser and T.H. McCulloch (Editors), Thermal History of sedimentary Basins–Methods and Case Histories. Springer, New York, NY., 181–195.

Hart, S.R, 1981. Diffusion compensation in natural silicates. Geochim. Cosmochim. Acta, 45: 279–291.

Harrison, T.M., Armstrong, R.L., Naeser, C.W. and Harakal, J.E., 1979, Geochronology and thermal history of the Coast Plutonic Complex, near Prince Rupert, British Columbia. Can. J. Earth Sci., 16: 400–410.

Hasebe, N., Tagami, T. and Nishimura, S., 1994. Towards zircon fission–track thermochronology: Reference framework for confined track length measurement. Chem. Geol., 110: 169–178.

Hurford, A.J., 1986, Cooling and uplift patterns in the Lepontine Alps South Central Switzerland and an age of vertical movement on the Insubric fault line. Contrib. Mineral

Petrol., 92: 413–427.

Lal, D., Rajan, R.S. and Tamhane, A.S., 1969. Chemical composition of nuclei of Z>22 in cosmic rays using meteoritic minerals as detectors. Nature (London), 221: 33–37.

Laslett, G.M., Kendall, W.S., Gleadow, A.J.W. and Duddy, I. R., 1982. Bias in measurement of fission–track length distributions. Nucl. Tracks, 6:79–85.

Laslett, G.M. and Gleadow, A.J.W., 1984. The relationship between fission track length and track density in apatite. Nucl. Tracks, 9: 29–38.

Laslett, G.M., Green, P.F., Duddy, I.R. and Gleadow, A.J.W., 1987. Thermal annealing of fission tracks in apatite: 2. A quantitative analysis. Chem. Geol. (Isot. Geosci Sect.), 65: 1–13.

Nishida, T. and Takashima, Y., 1975. Annealing of fission tracks in zircons. Earth Planet. Sci Lett., 27: 257–264.

Paul, T.A. and Fitzgerald, P.G., 1992. Transmission electron microscopic investigation of fission tracks in fluorapatite. American Mineralogist. 77: 336–344.

Tagami, T., Ito, H., and Nishimura, S., 1990. Thermal annealing characteristics of spontaneous fission tracks in zircon. Chem. Geol. Isot. Geosci. Sec. 80: 159–169.

Tagami, T., Uto, K., Matsuda, T., Hasebe, N. and Matsumoto, A., 1995. K–Ar biotite and fission–track zircon age of the Nisatai Dacite, Iwate Prefecture, Japan: A candidate for an age standard. Geochem. J. 29: 207–211.

Tagami, T., Shimada, C., and Nishimura, S., 1996. Natural long–term annealing and fossil partial annealing zone around a granitic pluton. J. Geophys. Research, 101: 8245–8255.

Winchell P., 1969. The compensation law for diffusion in silicates. High Temp. Sci. 1:200–215.

Yamada, R., Tagami, T. and Nishimura, S., 1993. Assessment of overetching factor for confined fission–track length measurement in zircon. Chem. Geol. 104: 251–259.

Yamada, R., Tagami, T. and Nishimura, S., 1995. Confined fission–track length measurement of zircon; assessment of factors affecting the paleotemperature estimate. Chem. Geol. 119: 293–306.

Part III: Orogenic History of the Northern Alps, Central Japan, Inferred from Fission Track Thermochronology

Abstract

The Northern Alps in the Central Japan is located in the west of Itoigawa–Shizuoka Tectonic Line (ISTL), which is considered as the Eurasian–North American plate boundary. I measured 51 fission track (FT) ages and eight FT length distributions of zircons and three FT ages of apatites, separated from acidic rocks occurring in the middle of the Northern Alps. Zircon FT age distributions are clearly divided into marginal "older" (> 50 Ma) and central "younger" (< 10 Ma) groups, and all of apatite yielded zero ages. At the middle of the younger part, zircon samples were collected at the various altitude ranging from 800 to 2100 m. Their apparent FT ages reduce from 6.9 to 0.7 Ma as their altitude declines from 2100 m to 1100 m; whilst ages are almost uniform of around 1 Ma at < 1100 m. This fact and the characteristic track length distribution pattern of these samples indicates that this area have rapidly uplifted at around 1 Ma and the estimated geothermal gradient is significantly higher then (~70 °C/km) than that of surrounding area (~40 °C/km). On the other hand, for samples along an eastward transect, apparent zircon FT age becomes younger from 4.2 to 1.6 Ma westward. The variation in ages and the track length patterns suggests the tilted uplifting based on estimated paleodepth of the samples in terms of zircon partial annealing zone when the uplifting started. Consequently, it is suggested that the uplifting in this period is accompanied with the heat source of 700–800 °C at the bottom of the upper crust, according to the modeling result of the variation of mountain height and underground temperature distribution in terms of uplift rate, uplift duration and the consequent denudation. This stage of uplift may have caused the high geothermal gradient of 70 °C/km at 1 Ma, and the rise of brittle–ductile boundary. In addition, the results of quantitative thermal history analysis for seven zircon samples suggests two events of the cooling rate change.

The difference in uplift timing and area implies two stages of uplifting in the Northern Alps region since 4 Ma; Stage I: uplifting of the whole region of the Northern Alps started 4 Ma, lasted until 1 Ma; Stage II: uplifting of narrow zone, central part of the Northern Alps, started and completed at around 1 Ma. For the Stage I, magmatic intrusion to the upper crust may have caused the domal uplifting, which was inferred by the tilted uplifting eastward. This magmatism was probably related to the simultaneous volcanic activity in the Central Japan. The Stage II uplifting of ductile zone, which had been raised at Stage II, may have been caused by horizontal compression by transition of the Eurasian–North American plate boundary.

1. Introduction

The Northern Alps in the Central Japan is a typical alpine mountain range located on the west of the Itoigawa–Shizuoka Tectonic Line (ISTL), which is considered as the Eurasian–North American plate boundary (e.g., Nakamura, 1983; Kobayashi, 1983). Nakamura (1983) and Seno (1985) considered that the Eurasian–North American plate boundary have jumped from central Hokkaido to the eastern margin of the Japan Sea and along the ISTL, and this jump have caused the uplift of the N. Alps. On the uplift mechanism of the N. Alps, Fukao and Yamaoka (1983) proposed the horizontal compression of plate tectonic origin on the bases of the gravity anomaly investigation. Ikeda (1990) proposed magmatic intrusion to the upper crust because the monogenetic volcanoes were active westward of the N. Alps region at 2.7–1.5 Ma (Shimizu and Itaya, 1993), implying the tensile stress field dominant in the central Japan then.

The N. Alps consist mainly of the marginal Mesozoic–Paleozoic marine sediments, and granitic rocks in the central region (Fig. 1). Based on geological and geochronologic evidences, the granitic batholith can be divided into marginal "older" (> 50 Ma) and central "younger" (< 10 Ma) parts (e.g., Uchiumi et al., 1995). According to the distribution of granitic conglomerates supplied from the N. Alps in the Northern Fossa Magna region (e.g., Hirabayashi, 1970), the N. Alps had already grown to a mountain range with considerable height at ~3 Ma (e.g., Ikeda, 1990). A high temperature zone (> 160°C) was found during a tunnel construction at the bottom of the Kurobe gorge with a depth of ~ 2000 m in the middle of "younger" part (e.g., Matsui and Yoshida, 1962), implying the residual heat of granitic body and that this granitic body is a hot dry rock (Nishimura and Mogi, 1986). The high temperature zone may be related to the existence of low P–wave velocity zone (e.g., Hirahara et al., 1989), strong P–wave attenuation (e.g., Katsumata et al., 1995), and seismic–aseismic boundary at a considerably shallow zone in the crust of the N. Alps region (e.g., Wada et al., 1990).

Fission track analysis has previously been applied in thermo–tectonic studies to constrain cooling and uplift patterns in various tectonic settings, e.g., the European Alps (Hurford, 1986), the Himalaya of northern Pakistan (Zeitler, 1985), the Transantarctic Mountains (Gleadow and Fitzgerald, 1987), the rifted continental margin in southeastern Australia (Moor et al., 1986), the northern England (Green, 1986), and the New Zealand Alps (Kamp and Tippett, 1993). Track length distribution shows the characteristic patterns according to the sample's thermal history because of the nature that FTs are shorten within a specific temperature range (partial annealing zone; PAZ), and that FTs remain their length after the system has cooled lower than the approximately middle of PAZ. These studies based the interpretation on analyses of track length pattern and apparent age, which approximate a duration passed since a system had cooled lower than the middle of PAZ. Brown et al. (1994) documented the potential of FT analysis for the estimation of denudation rate and implication for

long–term landscape development models by the use of track length distribution data to yield additional information about the cooling (denudational) history of a sample. In addition, modeling approach methods were developed to constrain further thermal histories from observed FT data, including age and track length distribution, by means of stochastic method to restrict the thermal histories compatible with observed data (e.g., Corrigan, 1991; Lutz and Omar, 1991; Gallagher 1995), applying the basic methodology (e.g., Duddy et al., 1988; Green et al., 1989ab) and annealing kinetics for apatite (e.g., Laslett et al., 1987, Crowley et al., 1991, Carlson, 1990).

This study provides new constraints on the Cenozoic orogenic history of the N. Alps by FT analysis, using mainly zircon. Apparent FT age distribution for relatively low temperature range around 250°C will reveal the landscape development later than plutonic intrusion. Modeling approach is also attempted to restrict possible thermal histories for some samples using recently reported annealing kinetic model (Yamada et al., 1995b). Analyses on the relationship between track length pattern and apparent age will constrain the vertical motion of rocks in terms of thermal histories of samples together with the variation in geothermal gradient. The information on the rock's vertical motion will give the estimate of the timing when the uplifting started, as well as the amount and rate of uplift.

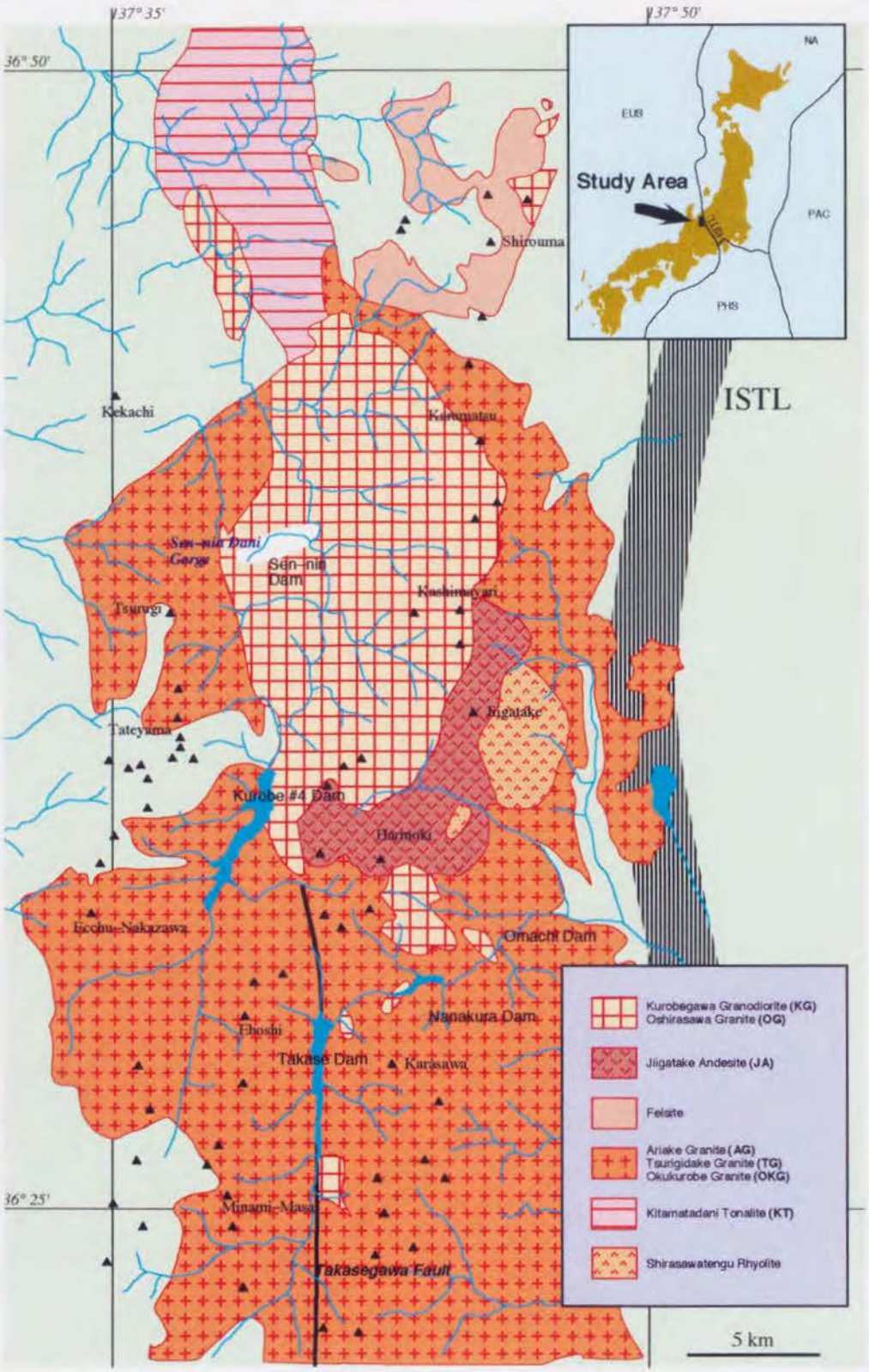

Fig. 1. Simplified geological map of study area, modified after Uchiumi et al. (1995) and Yamada et al. (1988). EUS: Eurasioan Plate, PHS: Philippine Sea Plate, PAC: Pacific Plate, NA: North–Americaa Plate, ISTL: Itoigawa-Shizuoka Tectonic Line. Solid triangles indicate summits with the levels > 2500 m.

2. Geological Setting

The Northern Alps, Central Japan, (i.e., Hida mountain range) consists mainly of two parts. The Mesozoic–Paleozoic marine sediments of the Hida Belt or Hida Marginal Belt distribute in the marginal region, and some granitic bodies of various periods intruded broadly in the central part (Fig. 1; modified after Uchiumi et al. (1995) and Yamada et al. (1988)). These granitic bodies have been roughly divided into older and younger groups so far (e.g., Uchiumi et al., 1995). The older group which constitute main parts of the N. Alps, consists of Late Cretaceous–Paleogene granites, named Ariake Granite (AG), Okukurobe Granite (OKG), Tsurugidake Granite (TG), and Kitamatadani Tonalite (KT). The younger group consists of Kurobegawa Granodiorite (KG) and Oshirasawa Granite (OG). KG distributes along the middle reach of the Kurobegawa river around the central part of the Late Cretaceous–Paleogene granites. There is a high temperature zone near the Sen–nin Dam in the central part of KG (Fig. 1). Highest temperature over 160 °C was recorded during the tunnel construction for the Kurobegawa No. 3 Hydro Power Plant of Kansai Electric Power Co., Inc. (Matsui and Yoshida, 1962). Yuhara (1981) reported the observation of heat discharge from rock surface of high temperature zone in the KG, and found that 98% of heat was conductivity transferred to air. The rock body of KG was considered as "hot dry rock" because hot springs and fumaroles were not so many in the tunnel and along the Kurobe River near the Sen–nin Dam (Yuhara , 1981; Nishimura and Mogi, 1986). Volcanic rocks exist at the relatively higher parts such as Jiigatake Andesite (JA), which can be classified as "younger" group. There are many northward trending faults in this area with the large vertical displacement (Harayama et al., 1991). The Takasegawa Fault, along which the Takase dam was constructed, is the one of those with clear displaced landform.

On the present–day state beneath this region, seismic analyses of the recent microearthquake observation indicated the existence of low–P wave velocity zone in the crust below the N. Alps (e.g., Hirahara et al., 1989) and strong attenuation of P–wave (e.g., Katsumata et al., 1995). The seismic–aseismic boundary of the N. Alps region is 8 km, whilst that of the Atotsugawa Fault, located in the 20 km west of the N. Alps, is 14 km (e.g., Wada et al., 1990, 1994). These seismological investigations imply that hot material may exist beneath the N. Alps region at the relatively shallow zone of about 10 km.

The geothermal gradient can be roughly estimated by the seismic–aseismic boundary temperature: Ito (1990) estimated the temperature at seismic–aseismic boundary as 300–400°C, based on the inversely proportional correlation between the surface heat–flow and the depth of the boundary. This relation can give the estimated mean geothermal gradient in the upper crust as ~ 50 °C/km for the central N. Alps area, and ~ 30 °C/km for the surrounding area. The geothermal gradient determined using deep wells are 40–60 °C/km for the central N. Alps area

(e.g., Nishimura et al., 1986), and ~ 40 °C/km for the surrounding region (e.g., Fujii et al., 1992). According to the distribution map of terrestrial heat–flow, the regional geothermal gradient of the Central Japan can roughly be assessed as 30–40 °C/km (e.g., Furukawa, 1995). The correspondence among the data above gives the estimates of geothermal gradients in and around the central N. Alps as 50–60 °C/km and 30–40 °C/km, respectively.

The compilation map of radiometric age data of this area reported previously is shown in Fig. 2. Most of them were obtained by K–Ar method. The ages of each bodies do not necessary indicate the timing of their activity because of the slow cooling of plutonic rocks and the secondary heating by the later intrusion. Many of the "older" group ages are older than 50 Ma. Some of them having younger ages seem to have been affected by the secondary heating of later intrusions. Most of the ages of KG or OG distribute younger than 10 Ma. Nishimura and Mogi (1986) found that the K–Ar whole rock ages (0.7–6 Ma) of granitic rocks around high temperature zone have a close relation to the altitude (700–2100 m) of sampling sites. In the about 20 km southern part of the study area, the Takidani Granodiorite was emplaced at 2 Ma and the rapid cooling began at 1.2 Ma, according to chronological study using various dating methods (Harayama, 1992).

In the Northern Fossa Magna, eastward region of the N. Alps, the supply of coarse conglomerates from the N. Alps had increased at Late Miocene or Early Pliocene time, and the most of the conglomerates were supplied from the N. Alps at Late Pliocene (3–1.7 Ma) (Hirabayashi, 1970). This indicates that the N. Alps had already started the uplift at Early Pliocene, and it had grown into high mountain range enough to supply an great amount of coarse conglomerate to surrounding region at Late Pliocene.

Two mechanisms were assumed for the uplift of the N. Alps region: One is the horizontal compression of plate tectonic origin (e.g., Fukao and Yamaoka, 1983). Fukao and Yamaoka (1983) proposed the horizontal compression based on the discussion that a crustal root beneath the mountain range should not be large enough to sustain isostatically the mountain topography, comparing with the negative Bouguer anomaly of ~-80 mgal around the N. Alps region suggested by gravity profiles (e.g., Yamamoto et al., 1982; Kono and Furuse, 1989). The other is the magmatic intrusion to the upper crust (e.g., Ikeda, 1990). Ikeda (1990) proposed magmatic intrusion to the upper crust because the monogenetic volcanoes were active westward of the N. Alps region at 2.7–1.5 Ma (Shimizu and Itaya, 1993), implying the tensile stress field dominant in the central Japan then.

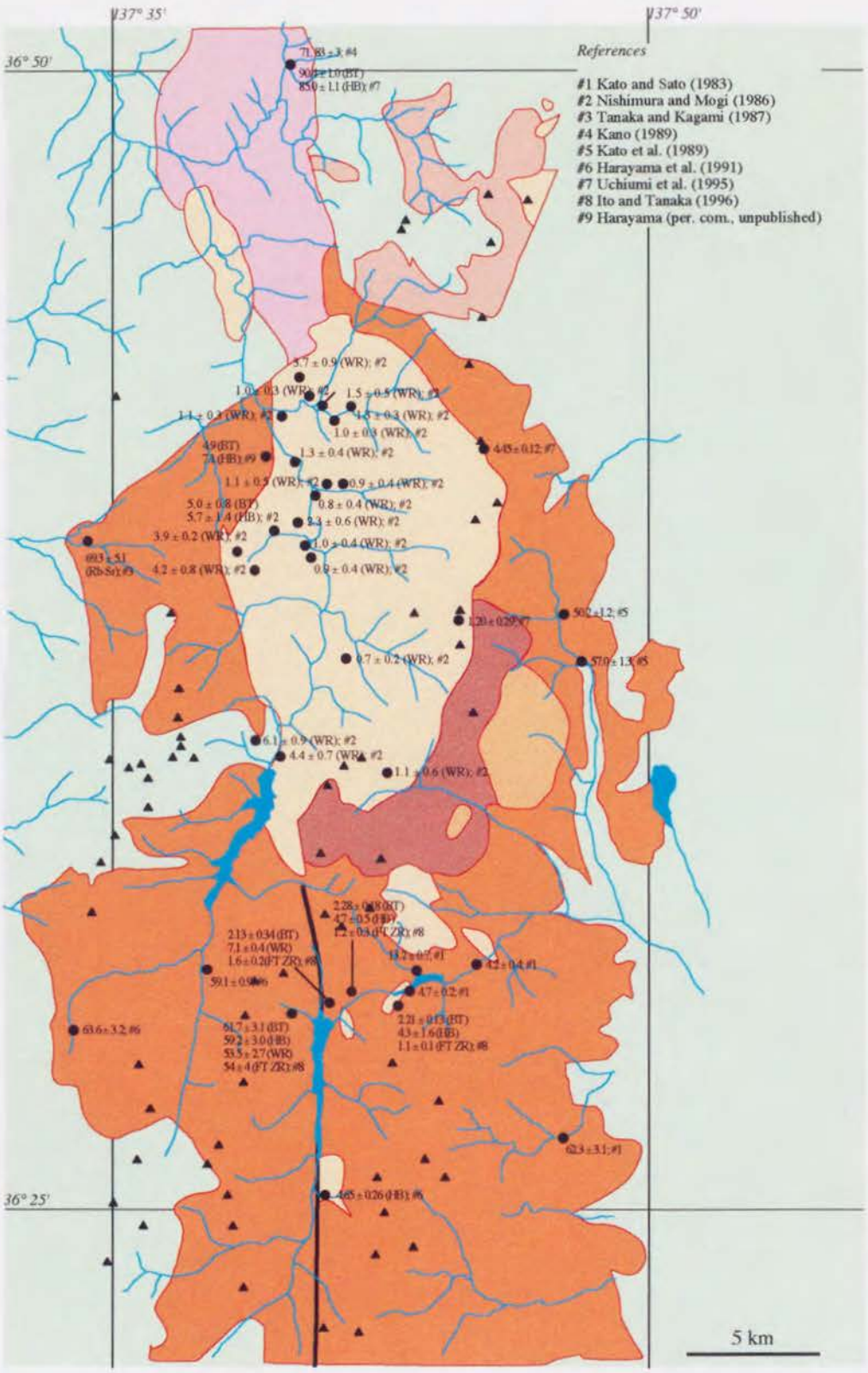

Fig. 2. Compilation map of radiometric ages reported previously for the Northern Alps area. Cited data were fundamentally determined by K-Ar method using biotite samples, otherwise used methods and/or minerals were identified in the parentheses. BT = biotite, HB = hornblende, WR = whole rock, ZR = zircon.

3. Techniques

FT dating was performed for collected samples by external detector method using zircon and apatite, following fundamentally the procedure reported by Tagami et al. (1988). In order to give further constraints on thermal history, FT lengths were measured for eight samples using horizontal confined tracks (HCT), following the procedures of Yamada et al. (1995a).

3.1. Sample Collection

Rock samples were collected from the area of ~50 km x ~25 km, along four transects for the mapping of FT ages in this region, regardless of the difference in rock bodies (Fig. 3). Three sampling transects are set across northward trend of the N. Alps (A, B, C), and one transect along (D). The sectional relief of summit level is also drown by tracing the height represented as maximum height of each interval of 1 km (Fig. 4). Around the high temperature zone, samples were collected at various altitudes (~800–2100 m) along the route from a deep gorge of the Sen–nin Dani to Mt. Sen–nin Dake in order to investigate the age variation versus the sampling altitude, indicated as an white ellipse in the Fig. 1. OMC65, OMC12 and OMC13 were collected from the borehole core, which were used for terrestrial heat flow determination by Nishimura et al. (1986). They reported the present temperature at the collected depth of OMC65 and OMC13 as 35°C and 60°C, respectively. Eight samples except for those with the code of "KRG" or "OMC", and rock type identification of all samples were provided by Dr. Harayama at Geological Survey of Japan. Sampling altitude and the rock type description are summarized in Table 1.

Table 1. Descriptions of the Northern Alps Samples

Sample	Transect	Rock type		Altitude (m)	K-Ar age (Ma)	± 1σ	References
KRG01	A, D	BT granite	(KG marginal facies or dyke)	1140	WR; 2.3	0.6	#2
KRG02	A, D	BT granite	(TG)	1420	BT; 5.0 HB; 5.7	0.8 1.4	#2
KRG03	A, D	BT granite	(KG)	990			
KRG04	A, D	BT granite	(TG?)	860	WR; 0.9	0.4	#2
KRG05	A, D	BT granite	(KG?)	2130			
KRG06	A, D	BT granite	(KG?)	1880			
KRG07	A, D	HB BT granite	(TG)	1700			
KRG08	A, D	BT granite	(KG)	1350			
KRG09	A, D	BT granite	(KG)	1310	WR; 0.7	0.2	#2
KRG10	A, D	BT granite	(KG)	800			
KRG12	A, D	Granite porphyry	(KG marginal facies or dyke)	1200			
KRG13	A, D	BT granite	(KG?)	2000			
KRG14	A, D	Felsite	(dyke?)	2050			
KRG15	A, D	Aplite or xenolith?	(dyke?)	2050			
KRG16	A, D	Thermally metamorphosed granite	(TG?)	2060	WR; 3.9	0.2	#2
KRG19	A	BT granite	(TG)	980			
KRG21	B, D	Graphic porphyry	(KG)	1400	WR; 4.4	0.7	#2
KRG22	B, D	Porphirytic granite (altered)	(OKG)	1450			
KRG23	B, D	Granite porphyry	(dyke)	1500			
KRG24	B, D	BT granite	(OKG)	1500			
KRG31	C, D	Tonalitic mylonite	(recrystalized)	1200			
KRG32	C, D	Thermally metamorphosed mylonitic BT granite	(OG)	1100	BT; 2.28 HB; 4.7 WR; 4.4 (FT ZR) 1.2	0.18 0.5 0.4 0.3	#5
KRG33	C	Thermally metamorphosed mylonitic BT granite	(OG)	1080	BT; 2.21 HB; 4.3 (FT ZR) 1.1	0.13 1.6 0.1	#5
					BT; 4.7	0.2	#1
KRG34	C	HB BT granite	(OG)	1070	BT; 13.2	0.7	#1
KRG35	C	BT granite	(OG)	1060			
KRG36	C	BT granite	(AG)	900	BT; 4.2	0.4	#1
KRG37	C	BT granite	(AG)	950			
KRG38	C	HB BT granite	(AG)	840			
KRG39	B	BT granite	(KG)	1400	WR; 1.1	0.6	#2
KRG40	B	Thermally metamorphosed ryolitic welded tuff	(JA)	1340			
KRG41	B	Lapilli tuff	(JA)	1150			
KRG42	C, D	HB BT granite	(AG)	1360	BT; 61.7 HB; 59.2	3.1 3.0	#5
					WR; 53.5 (FT ZR) 54	2.7 4	#5
KRG43	C, D	BT granite	(AG)	1300			
KRG44	C, D	Thermally metamorphosed BT granite	(OG)	1300			
KRG45	C, D	BT granite (partly cataclastic)	(KG)	1300	BT; 2.13 WR; 7.1 (FT ZR) 1.6	0.34 0.4 0.2	#5
KRG51	D	Porphyritic BT granite	(AG?)	650	WR; 1.1	0.3	#2
KRG52	D	Thermally metamorphosed mylonite	(xenolith?)	470			
KRG53	D	HB-BT Granodiorite	(KT)	320			
KRG54	D	BT Granite	(AG?)	450			
KRG55	D	HB-BT Granodiorite	(KT)	540			
OMC65	B, C	BT granite	(AG)	230			
OMC12	B, C	HB BT granite	(AG)	-320			
OMC13	B, C	HB BT granite	(AG)	-420			
73102	D	PX-HB-BT granodiorite	(KG, branch)	1560	HB; 4.65	0.26	#3
92910-4	A	Tonalite	(KG)	2615	BT; 4.45	0.12	#4
92913-3	A	Granite porphyry	(KG)	2889	BT; 1.20	0.29	#4
94914-3	D	HB-BT granodiorite	(KG, branch?)	380			
94917-1	A, D	HB BT granite	(TG?)	960	BT; 4.9 HB; 7.1		#6
YH126	B, D	Granite porphyry	(dyke)	1440			
YH347	C, D	HB BT granite	(OKG)	1510	BT; 59.1	1.30	#3
HT54	D	HB-BT Granodiorite	(KT)	660	BT; 90.4 HB; 85.0	1.0 1.1	#4

Abbreviation of rock types: BT = biotite, HB = hornblende, PX = pyroxene, WR = whole rock, ZR; zircon, KG = Korobegawa Granodiorite, AG = Ariake Granite, TG = Turugidake Granite, OG = Oshirasawa Granite, JA = Jiigatake Andesite, KT = Kitamatadani Tonalite, OKG = Okukurobe Granite. References for K-Ar ages: #1 = Kato and Sato (1983), #2 = Nishimura and Mogi (1986), #3 = Harayama et al. (1991), #4 = Uchiumi et al. (1995), #5= Ito and Tanaka (1996), #6 = Harayama (per. com., unpublished.)

3.2. Fission Track Analysis

For age determination, zircon and apatite concentrates were separated from 3–5 kg whole rock samples using conventional magnetic and heavy liquid techniques. Zircon separates are mounted in polytetrafluorethylene–perfluoroalkoxyethlene (PFA) Teflon® sheets at 300°C, and apatite separates are mounted in epoxy resin. Both are ground to reveal internal surfaces, and polished using 15 μm and 2.5 μm of diamond paste. After polishing, the crystals are etched KOH–NaOH eutectic etchant at 214°C for zircon, and in 0.6% HNO_3 at 32°C, until FTs appear well etched under the microscope. Low–uranium mica external detectors are sealed in intimate contact with the mount after etching. Mounts with detectors are then irradiated at the Thermal Column Pneumatic Tube facility (TC–Pn) of Kyoto University Research Reactor (KUR) during 30 min. for zircon, and 4 h for apatite, respectively. After irradiation, the mica detectors were etched in 46% HF for 4 min. at 32°C. FT density determinations are undertaken with Nikon Biophot and FXA optical microscope, using 100x dry objectives with 10x eyepieces at actual magnification of 925x. FT ages reported here are determined by using the zeta calibration approach (Hurford and Green, 1983). Statistical error on FT ages are given by the "conventional analysis" (Green, 1981). Personal calibration of FT density measurements is carried out on international age standards (Hurford and Green, 1983; Green 1985; Hurford and Watkins, 1987), the results of which are presented in Table 2. Mean weighted zeta value of 373.3 ± 10.8 (1σ) is adopted for zircon.

For track length measurement of some zircon samples, sample preparation procedures used are almost the same as those for age determinations. Zircon grains are mounted in a PFA Teflon® sheet and their external prismatic surfaces are ground and polished. Mounts are etched in KOH–NaOH eutectic etchant at rather higher temperature of 248 ± 1°C, until the width of the surface tracks perpendicular to *c*–axes become 2 μm (cf. Yamada et al., 1995a). Track lengths are measured for horizontal confined tracks (HCTs) throughout this study, including both track–in–track and track–in–cleavages (TINT's and TINCLE's, respectively; e.g., Lal et al., 1969). HCT's with the widths of 1 ± 0.5 μm are selectively measured to minimize the overetching bias (Yamada et al., 1993, 1995a).

It is difficult to measure the HCT lengths in zircon samples with low ρ_s. Some experimental techniques were investigated for increasing the detection efficiency of HCT's in low track density samples by making artificial tracks or cleavages (e.g., Yamada et al., 1996). Of the techniques examined by Yamada et al. (1996), two techniques are applied in this study, named 'heavy ion irradiation using a tandem accelerator' (HIT) and 'artificial cracking method' (ACM), respectively. For the HIT, $^{58}Ni^{11+}$ ions are accelerated using a tandem accelerator at the Tandem Accelerator Laboratory of Kyushu University, and irradiated to the samples in order to form artificial tracks (Fig. 5a). For the ACM, zircon samples are artificially cracked

based on the property that zircon crystals tend to crack along a direction parallel to crystallographic *c*–axis (Fig. 5b). It has been confirmed that these experimental techniques do not yield significant bias for track length measurement (e.g., Yamada et al., 1996).

Table 2. Specimen Table of Zircon Age Standard Analysis for System Calibration by the Zeta Approch

International age standards	Mineral	Etching time (h)	No. of crystals	Spontaneous ρ_s	Spontaneous N_s	Induced ρ_i	Induced N_i	$P(\chi^2)$ (%)	Glass	Dosimeter ρ_d	Dosimeter N_d	ζ	±	1σ
Buluk Member Tuff	zircon	50	8	0.868	233	0.954	256	99	612	0.099	2159	362.4		34.0
Buluk Member Tuff	zircon	60	16	1.018	473	1.061	493	99	612	0.097	2600	349.3		23.9
Fish Canyon Tuff	zircon	25	13	4.208	978	2.844	661	98	612	0.100	2205	375.9		20.6
Fish Canyon Tuff	zircon	25	7	5.294	609	3.860	444	19	612	0.093	2167	434.2		28.7
Mount Dromedary Banatite	zircon	20	9	15.36	2321	2.734	413	13	612	0.097	2600	361.1		20.7
											Mean zircon ζ :	373.3		10.8

(1) Analyses by external detector method; track densities (ρ) are as measured and are $x10^6$ cm^{-2}; numbers of tracks counted (N) shown; $4\pi/2\pi$ geometry correction factor = 0.5.

(2) $P(\chi^2)$ is probability of obtaining χ^2 = value for ν degrees of freedom where ν = (number of crystals - 1).

(3) Independent ages used are: Bulk Member Tuff = 16.3 ± 0.1 Ma (1σ), Fish Canyon Tuff = 27.77 ± 0.04Ma, Mount Dromedary Banatite = 98.7 ± 0.3 Ma (Tagami, 1987).

(4) An uncertainty component from independent age is included in the error on each ζ -value; mean ζ and its error weighted according to uncertainties on individual ζ -values.

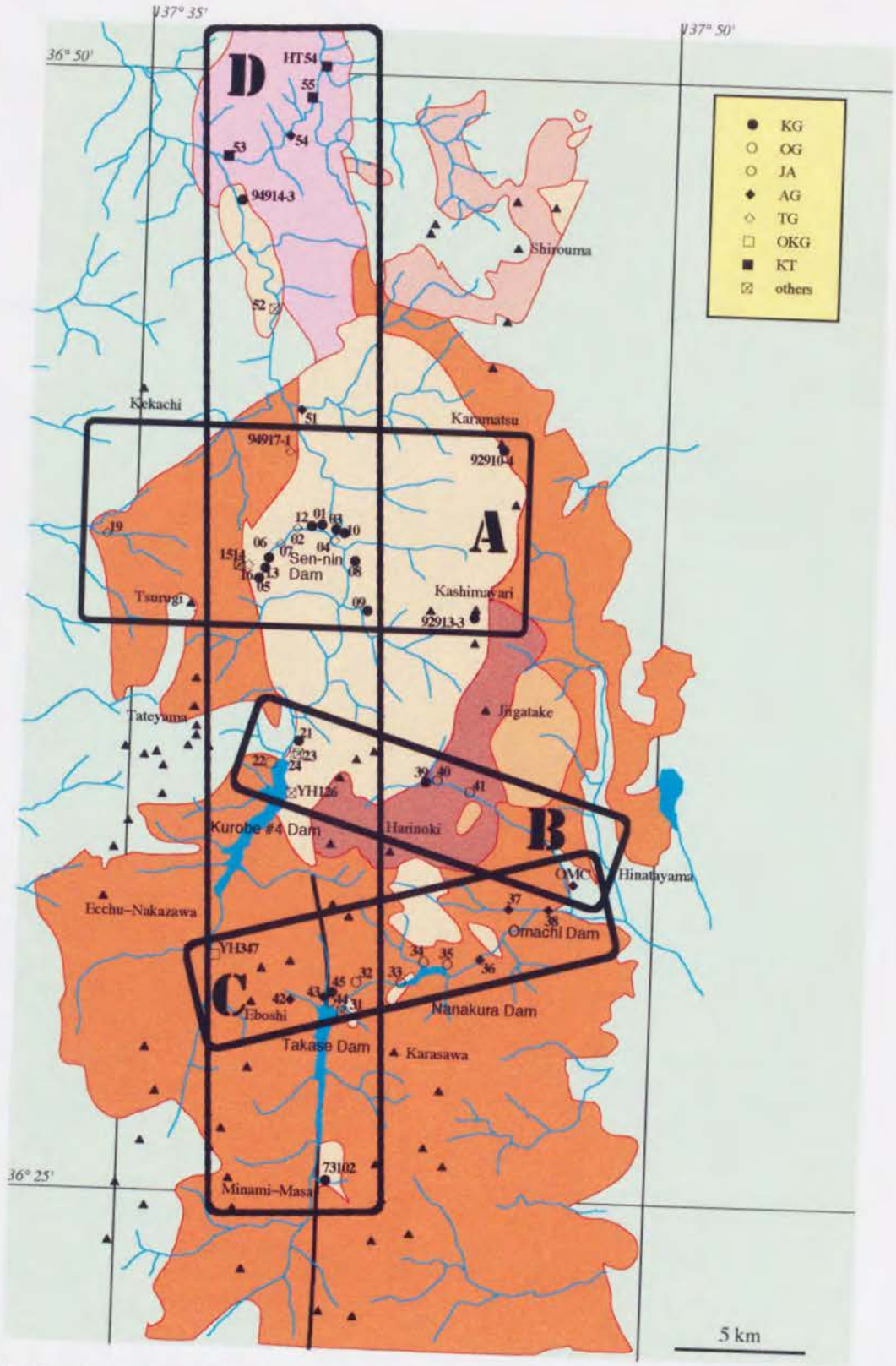

Fig. 3. Sampling locality map with the extent of four transects. All samples belongs to at least one of these transects. Sample code of KRG is omitted for samples expressed by two digits. Core samples of OMC were collected at the three different depths. Rock types are also indicated by various symbols in the legend, based on the rock type identification by Harayama (per. com.; see Table 1).

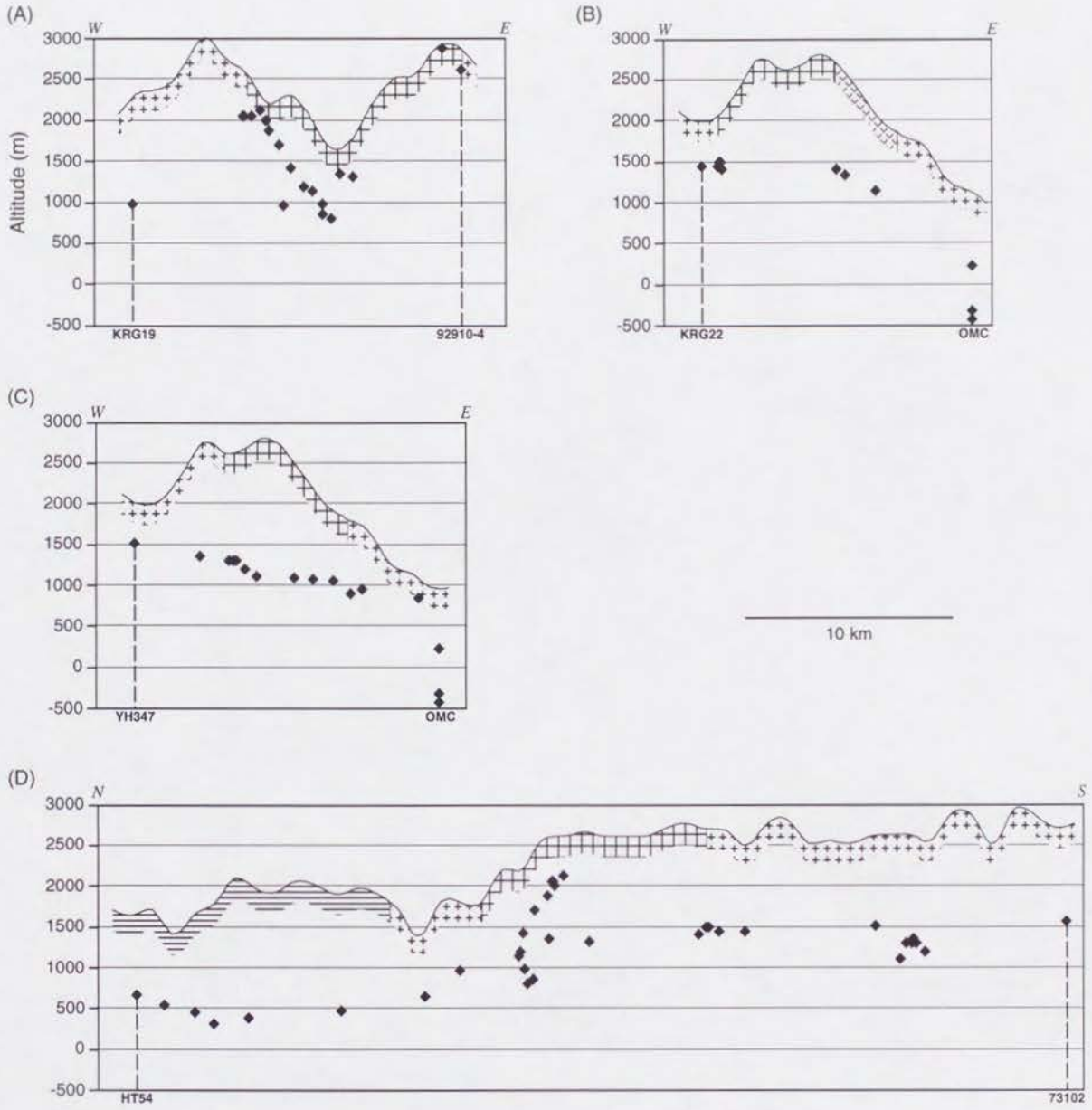

Fig. 4. Sampling localities of each transects with the sectional map of the summit level for each transects indicated in the Fig. 3. Summit level maps are drown by tracing the altitude represented as the topographically highest points of each segments formed by dividing the belt–shaped transects by 1 km interval along. Samples are collected along the riversides except for the core samples (OMC).

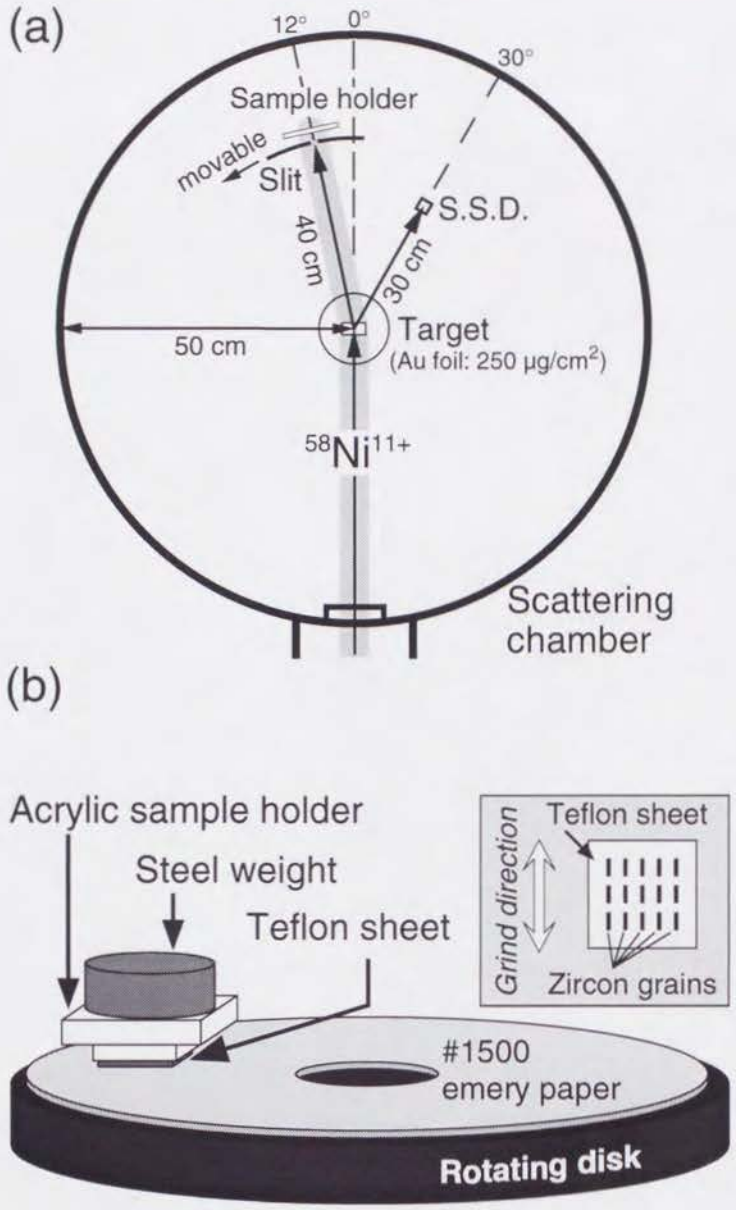

Fig. 5. Schematic configuration of techniques for enhancing detection efficiency of confined fission tracks in minerals: (a) Interior schema of scattering chamber set for heavy ion irradiation by a tandem accelerator. The chamber is evacuated to ~10^{-7} torr. $^{58}Ni^{11+}$ ions are accelerated to collide with a gold target, which is set at the center of the chamber for the Rutherford scattering. Some of scattered ions are caught by a silicon semi-conductor detector (S.S.D.) for fluence measurement. Some other pass through the slit to be injected into the target samples set at the movable sample holder, which is remote–controlled outside the chamber; (b) Setting of the artificial cracking method. A Teflon sheet, in which zircon grains are mounted, is pasted on the acrylic sample holder. A sample holder is placed on the wetted #1500 emery paper pasted on a rotating disk of an automatic grinding and polishing machine, and a steel weight (740 g) is put on the sample holder. Rotation speed is ~2 rps and the relative grinding speed of a sample to the rotating disk is ~1 m/s. The sketches of (a) and (b) are modified after Yamada et al., (1996).

3.3. Thermal History Modeling

In order to constrain thermal histories from the FT data, I use the annealing kinetic function (AKF) of the "fanning model with infinite critical temperature", proposed by Yamada et al. (1995b), and the basic methodology described by Duddy et al. (1988) and Green et al. (1989ab) to predict fission track age and track length distribution for a given thermal history. The modeling follows the conventional methods where individual tracks are formed at regular intervals over the total thermal history, and the length reduction for a particular FT is calculated over that portion of the total thermal history experienced by the track. Rather than specify a particular thermal history a priori, I adopt a stochastic approach similar to that used by Corrigan (1991). A thermal history is represented by a certain number of time–temperature points in this study, whilst Corrigan (1991) approximated a thermal history by a weighted sum of Chebyshev polynomials. The random Monte Carlo method is used to select thermal history compatible with observed FT data. A simulated annealing algorithm (Metropolis et al., 1953) is used for effective optimization in the stochastic process. The detailed modeling procedure is described in the Appendix A.

The sensitive temperature range of the modeling differs according to the AKF used. The sensitive temperature range of the AKF applied in this study is approximately 200–350°C for the geological time scale (i.e., heating duration of 10^6 y). The sensitivity and analytical resolution for the modeling procedure used in this study have been previously examined by analyzing predicted FT data for the synthetic thermal histories (Yamada, 1996). It is revealed by testing the reproducibility of various synthetic thermal histories, that the sensitivity for the variation of heating duration is less than that for temperature because of the FT annealing behavior itself, and that this modeling procedure has the bias to reproduce the slower cooling rate (~50–100%) than original synthetic one in the cooling phase of a thermal history. Therefore, information about time for cooling phase in a thermal history should be considered younger than that presented in analytical results.

4. Results and Interpretation

4.1. FT Age Data

FT analytical results are summarized in Table 3, including their FT ages and confined track length measurements. 49 zircon FT ages could be obtained from 51 samples. Two samples could not be counted, because of many inclusions in zircon crystals of KRG37, and small amount of grains separated from KRG44. These two are classified as "younger group" (i.e., < 10 Ma), based on the etching time. Two samples of KRG54 and YH347, which are identified as older group granites, yields low $P(\chi^2)$ values because of a broad range of single grain ages. Their surfaces after etching present the mixture of very short tracks with 'dot' shapes and relatively longer tracks (Fig. 6). This mixture causes the broad range of single grain ages, indicating that these samples might be experienced the secondary heating after intrusion of the rock bodies.

Apatite ages for three samples (KRG42, OMC65, OMC13) have been determined as zero age because almost no spontaneous tracks could be found, although induced tracks have been counted. Their apatite FT ages are totally reset whilst the zircon ages are not. It means that these samples may have recently experienced the temperature between apatite closure temperature (~100°C; e.g., Wagner and Van den haute, 1992) and zircon closure temperature (~260°C; e.g., Tagami and Shimada, 1996).

Table 3. Fission Track Data for Northern Alps Samples (continued)

Sample	Mineral	Etching time	No. of crystals	Spontaneous ρ_s	Spontaneous N_s	Induced ρ_i	Induced N_i	$P(\chi^2)$ (%)	$\overline{\rho_i/\rho_s} \pm 1\sigma$		Dosimeter ρ_d	Dosimeter N_d	Age ± 1σ (Ma)	
KRG01	Zircon	80 h	8	0.116	34	2.905	854	30			0.100	2205	0.74	0.13
KRG02	Zircon	80 h	12	0.245	57	2.500	581	54			0.100	2205	1.83	0.26
KRG03	Zircon	80 h	8	0.108	21	2.602	508	82			0.100	2205	0.77	0.17
KRG04	Zircon	80 h	8	0.159	20	2.335	293	66			0.102	2070	1.30	0.31
KRG05	Zircon	60 h	7	2.289	258	6.317	712	68			0.102	2070	6.93	0.56
KRG06	Zircon	75 h	12	1.440	313	5.730	1245	10			0.098	2609	4.62	0.33
KRG07	Zircon	75 h	12	0.475	85	2.174	389	99			0.098	2609	4.02	0.50
KRG08	Zircon	75 h	13	0.112	28	2.105	526	50			0.100	2205	0.99	0.20
KRG09	Zircon	75 h	15	0.205	44	2.410	518	35			0.100	2205	1.58	0.26
KRG10	Zircon	80 h	10	0.091	20	2.378	525	76			0.100	2205	0.71	0.16
KRG12	Zircon	60 h	14	0.066	40	1.501	907	32			0.111	2217	0.91	0.15
KRG13	Zircon	40 h	11	1.193	273	4.609	1055	20			0.111	2217	5.36	0.41
KRG14	Zircon	60 h	12	0.894	188	3.447	725	9			0.111	2217	5.37	0.48
KRG15	Zircon	60 h	3	0.269	20	2.138	159	19			0.111	2217	2.60	0.62
KRG16	Zircon	50 h	13	0.828	203	2.602	638	51			0.111	2217	6.59	0.58
KRG19	Zircon	23 h	10	5.569	1372	2.354	580	7			0.109	2183	48.2	3.0
KRG21	Zircon	60 h	9	0.289	52	3.964	714	7			0.111	2217	1.51	0.22
KRG22	Zircon	60 h	8	0.273	81	2.524	748	27			0.111	2217	2.24	0.27
KRG23	Zircon	55 h	2	0.086	2	1.850	43	54			0.111	2217	0.96	0.70
KRG24	Zircon	55 h	10	0.201	46	3.766	862	54			0.111	2217	1.10	0.17
KRG31	Zircon	40 h	9	0.384	103	3.662	983	18			0.111	2217	2.17	0.24
KRG32	Zircon	55 h	6	0.498	59	3.485	413	84			0.111	2217	2.96	0.43
KRG33	Zircon	50 h	4	0.585	34	5.232	304	94			0.109	2277	2.27	0.42
KRG34	Zircon	55 h	9	0.311	77	2.448	606	54			0.109	2277	2.58	0.33
KRG35	Zircon	55 h	7	0.297	49	1.745	288	73			0.109	2277	3.46	0.55
KRG36	Zircon	55 h	11	1.196	207	5.776	1000	9			0.109	2277	4.21	0.35
KRG37	Zircon	(50 h)												
KRG38	Zircon	30 h	8	5.351	572	1.918	205	32			0.109	2277	56.7	5.0
KRG39	Zircon	40 h	8	0.372	66	5.022	887	21			0.109	2277	1.51	0.20
KRG40	Zircon	55 h	6	0.190	40	2.420	509	40			0.109	2277	1.60	0.27
KRG41	Zircon	55 h	2	0.478	20	5.952	249	33			0.109	2277	1.63	0.38
KRG42	Zircon	30 h	14	5.622	1385	2.095	516	9			0.109	2277	54.6	3.4
	Apatite	1 min	4	0.000	0	(0.225)	(150)				0.743	2762	0.00	
KRG43	Zircon	25 h	11	11.121	1680	3.892	588	15			0.109	2277	58.1	3.5
KRG44	Zircon	(55 h)												
KRG45	Zircon	60 h	5	0.183	20	2.289	250	94			0.109	2183	1.63	0.38
KRG51	Zircon	41 h	18	0.534	160	9.283	2783	20			0.097	2600	1.04	0.09
KRG52	Zircon	50 h	3	0.194	7	2.360	85	81			0.097	2600	1.50	0.59
KRG53	Zircon	30 h	15	7.022	1991	1.859	527	40			0.097	2600	68.6	4.1
KRG54	Zircon	60 h	15	2.734	896	2.151	705	< 0.1	1.177	0.139	0.097	2600	23.1	1.4
KRG55	Zircon	60 h	16	9.901	3647	2.077	765	7			0.097	2600	86.6	4.6
OMC65	Zircon	35 h	10	5.775	1369	1.607	381	60			0.098	2609	66.0	4.5
	Apatite	1 min	1	0.000	0	(0.069)	(4)				0.743	2762	0.00	
OMC12	Zircon	35 h	8	6.907	923	2.260	302	92			0.098	2609	56.2	4.2
OMC13	Zircon	35 h	9	5.864	845	1.874	270	6			0.098	2609	57.5	4.5
	Apatite	1 min	3	0.000	0	(0.445)	(55)				0.743	2762	0.00	
73102	Zircon	61 h	13	0.195	58	1.489	443	78			0.097	2600	2.38	0.34
92910-4	Zircon	50 h	13	0.165	36	1.117	244	26			0.097	2600	2.68	0.49
92913-3	Zircon	41 h	7	0.191	20	1.826	191	44			0.097	2600	1.90	0.45
94914-3	Zircon	50 h	12	0.235	50	2.027	431	23			0.097	2600	2.11	0.32
94917-1	Zircon	60 h	19	0.222	110	2.749	1361	96			0.097	2600	1.47	0.15
YH126	Zircon	50 h	17	0.122	112	2.198	2010	17			0.097	2600	1.01	0.10
YH347	Zircon	41 h	10	9.089	2239	3.751	924	< 0.1	2.403	0.163	0.097	2600	44.0	2.3
HT54	Zircon	30 h	14	9.860	2177	2.120	468	19			0.097	2600	84.5	5.2

Track densities (ρ) are x10^6 cm^{-2}. All analyses by external detector method using 0.5 for the $4\pi/2\pi$ geometry correction factor. Zircon ages calculated using dosimeter glass SRM 612 and the zeta-value = 373.3 ± 10.8 (1σ). N is number of tracks counted. $P(\chi^2)$ is the probability of obtaining χ^2 value for ν degrees of freedom where ν = (number of crystals - 1) [Galbraith, 1981]; pooled ρ_i/ρ_s ratio used to calculate age and uncertainty where $P(\chi^2) > 5\%$; mean ρ_i/ρ_s ratio is used to calculate age and uncertainty where $P(\chi^2) < 5\%$ [Green, 1981].

Table 3. (continued)

Sample	Mean track length (μm)	± 1σ	Standard deviation	Number of lengths
KRG01	8.61	0.58	2.52	26
KRG02	6.84	0.40	2.67	45
KRG03				
KRG04				
KRG05	9.58	0.16	1.79	122
KRG06	150	0.15	1.83	150
KRG07	7.72	0.18	2.01	121
KRG08				
KRG09				
KRG10				
KRG12				
KRG13				
KRG14				
KRG15				
KRG16				
KRG19				
KRG21				
KRG22				
KRG23				
KRG24				
KRG31				
KRG32				
KRG33				
KRG34	10.64	0.14	0.91	43
KRG35	10.13	0.15	1.25	69
KRG36	8.84	0.32	2.32	52
KRG37				
KRG38				
KRG39				
KRG40				
KRG41				
KRG42				
KRG43				
KRG44				
KRG45				
KRG51				
KRG52				
KRG53				
KRG54				
KRG55				
OMC65				
OMC12				
OMC13				
73102				
92910-4				
92913-3				
94914-3				
94917-1				
YH126				
YH347				
HT54				

Overetching factor (Yamada et al., 1993) and length bais (Laslett et al., 1982) are not caliblated for track lengths data.

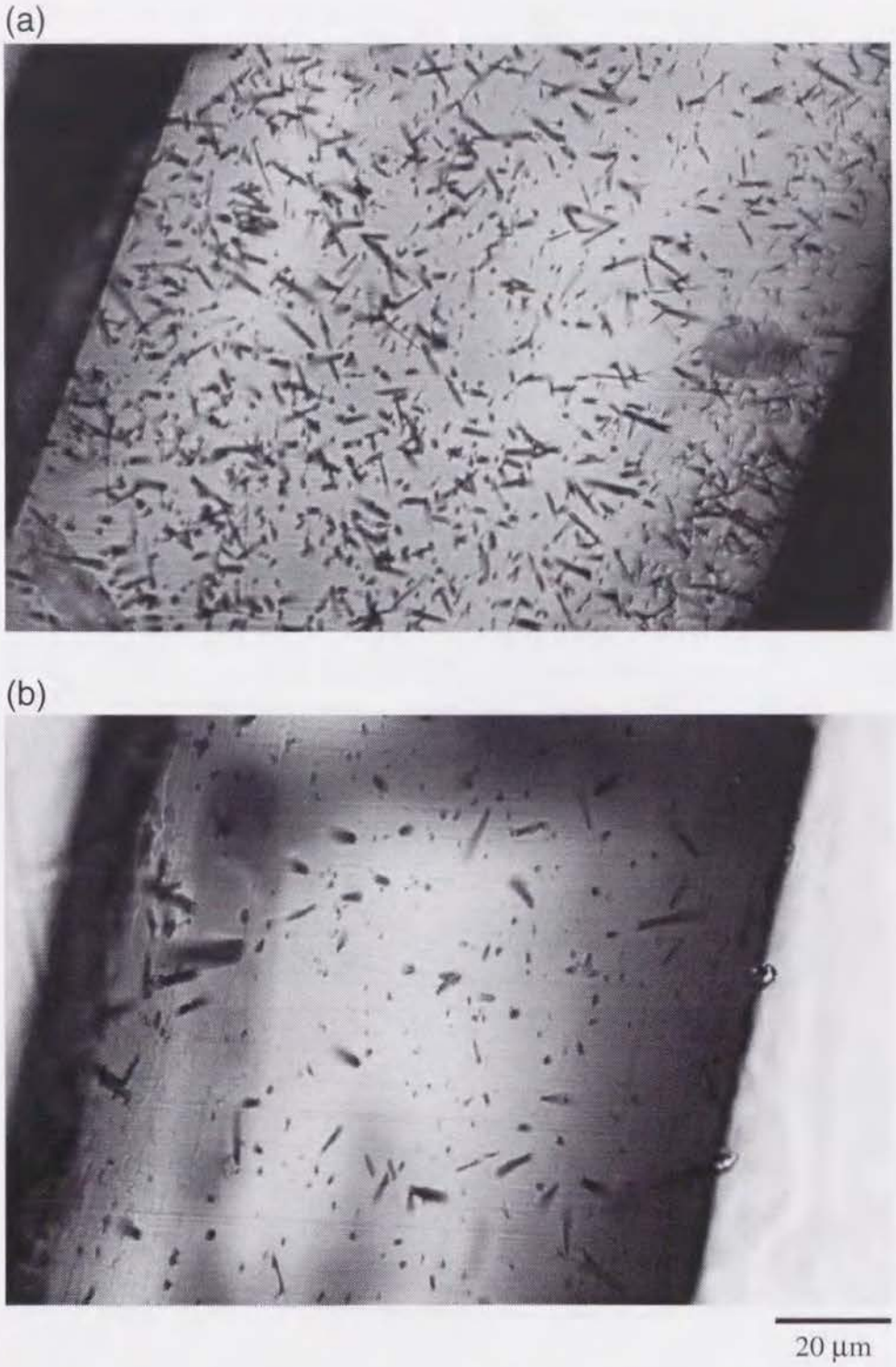

Fig. 6. Photographs of representative zircon samples of (a) YH347 and (b) KRG54 after etching, yielding low $P(\chi^2)$ values. These figures show the mixture of dot–shaped tracks shortened extremely by thermal annealing and relatively longer tracks formed after cooled below ZPAZ.

4.2. The Spatial Distribution of FT Ages

FT age distribution for each rock bodies are shown in Fig. 9, together with the reference ages of K–Ar method. The "younger" FT ages of TG and AG may be caused by the reheating of later intrusion of "younger" plutons of KG or OG, or dikes. One sample of KT (KRG53; 68.6 ± 4.1 Ma (1σ)), which occupies most northern part of studied area, may have suffered secondary heating by the northern TG or AG, indicating that the intrusion of AG and TG were significantly later than that of KT.

The spatial distribution of zircon FT age in the N. Alps is shown in Fig. 7. As a general, most of the samples from "younger" rock bodies are < 10 Ma, and "older" one, which encompass the "younger" bodies, are > 50 Ma. According to the spatial age distribution, rock bodies in the studied area can be roughly divided into three parts as follows; [KT] (> 65 Ma), [AG, TG, OKG] (10–65 Ma), and [KG, OG, JA] (< 10 Ma). The "younger" age samples are distributed in the central part of study area within ~10 km width with northward trend. The zircon FT age distribution along four transects are shown in Fig. 8. As a whole, the older age data are scattered in the marginal zone, and younger ones in the middle in each transect. The positive correlation is recognized between the topography and FT zircon age for the "younger" ages of Transect A, whilst the negative one for Transect C. Some of the "older" rock samples have "younger" age, which are located at middle part along the Transect C. Obvious gaps between "older" (> 50 Ma) and "younger" ages (< 10 Ma) are recognized at some parts. These gaps do not necessarily correspond to the rock body boundaries. Between KRG43 and KRG45, the Takasegawa Fault, which is located within the distance of 200 m, may relate the age gap between these two samples (Fig. 8C).

Along the Transect C, the horizontal age variation is recognized that the apparent zircon FT age varies horizontally becomes younger from 4.2 to 1.6 Ma westward. On the other hand, the vertical variation is recognized along the Transect A. FT zircon age distribution versus sampling altitude along the Sen–nin Dani gorge is shown in Fig. 10, together with K–Ar, whole rock age data of Nishimura and Mogi (1986). Data for dike samples are excluded. Apparent age reduces from 6.9 to 0.7 Ma as the sampling altitude decreases from 2100 m to 1100 m, whilst ages are almost constant at ~ 1 Ma at lower than 1100 m. The positive correlation between age and altitude implies the conductive heat transfer in vertical direction such as cooling from the surface or heating from the bottom. Because KG is consist of hot dry rock (Yuhara, 1981; Nishimura and Mogi, 1986), it seems reasonable to suppose conductive heat transfer in this high temperature zone.

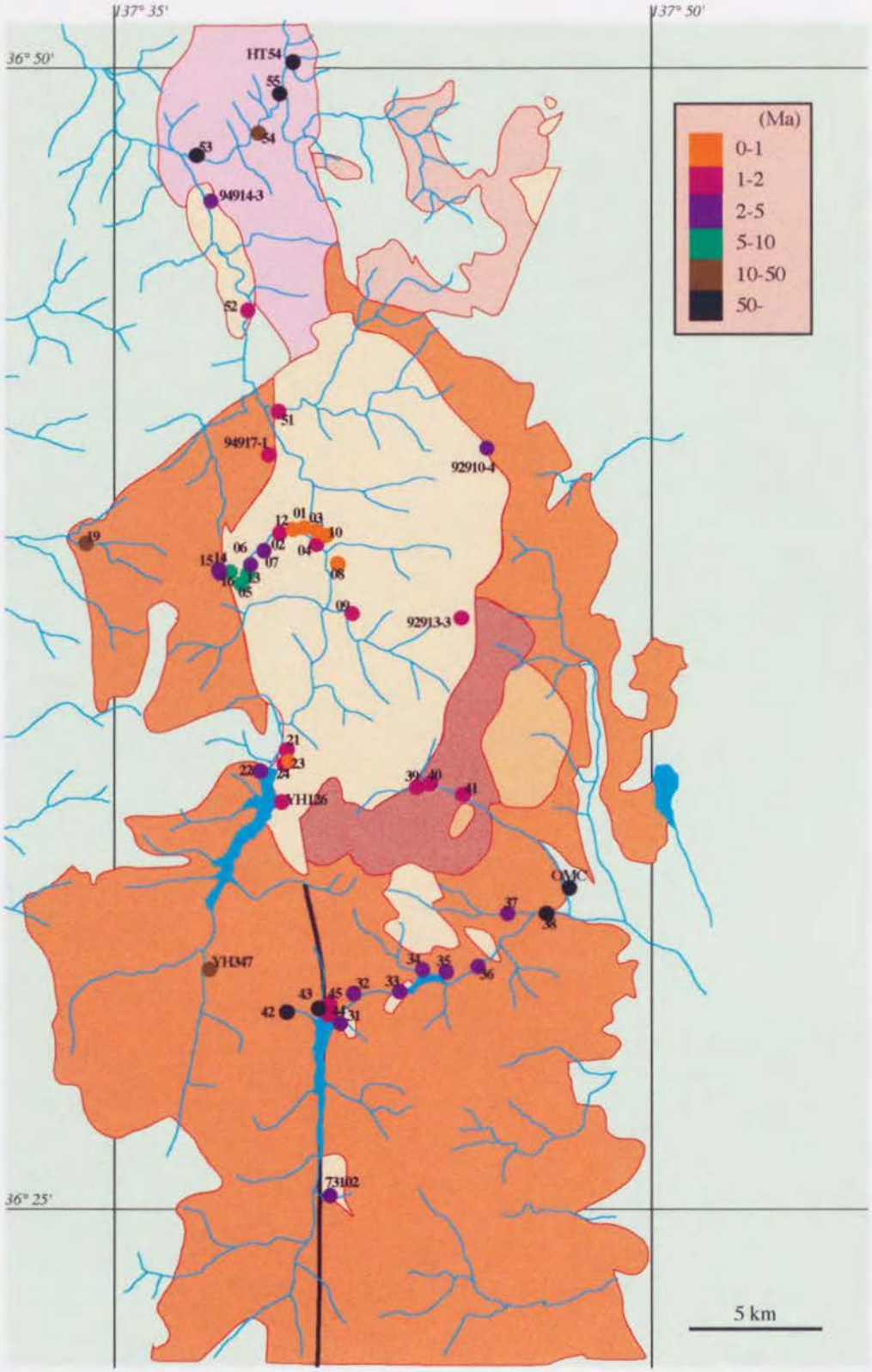

Fig. 7. Zircon FT age distribution with sampling localities. Dating results are represented by different symbols as indicated in the legend.

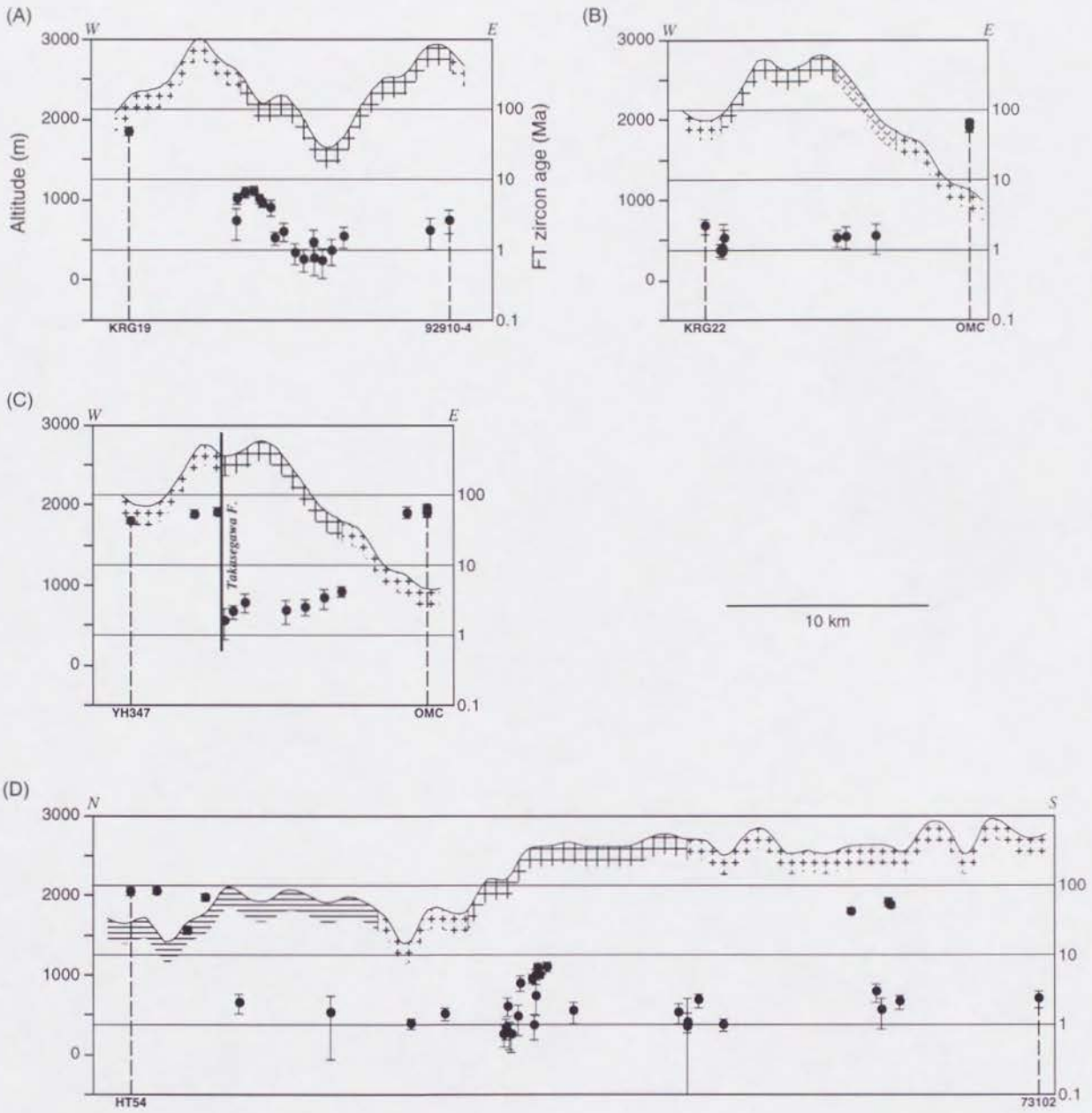

Fig. 8. Zircon FT age distribution along the sectional map of the summit level for each transects. Ages are plotted for logarithmic scale.

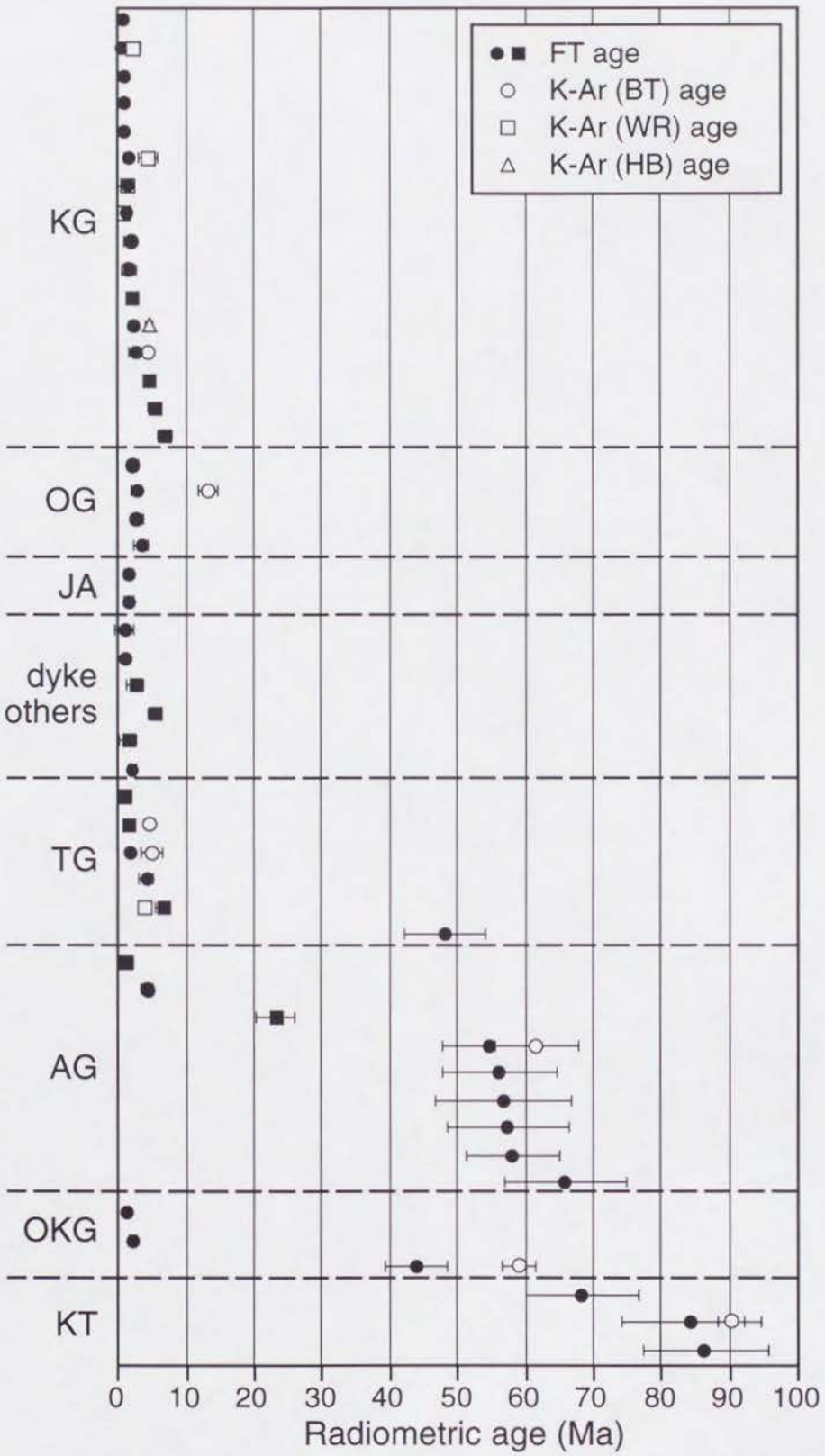

Fig. 9. Zircon FT age distribution for each rock bodies. The FT ages determined are indicated as solid symbols. Circles are of the samples whose rock types are confidently identified, whilst squares less confidently (See the columns of rock type in Table 1). Open ones are of previously reported in the reference titles as listed in the Table 1. *Errors* are 2σ.

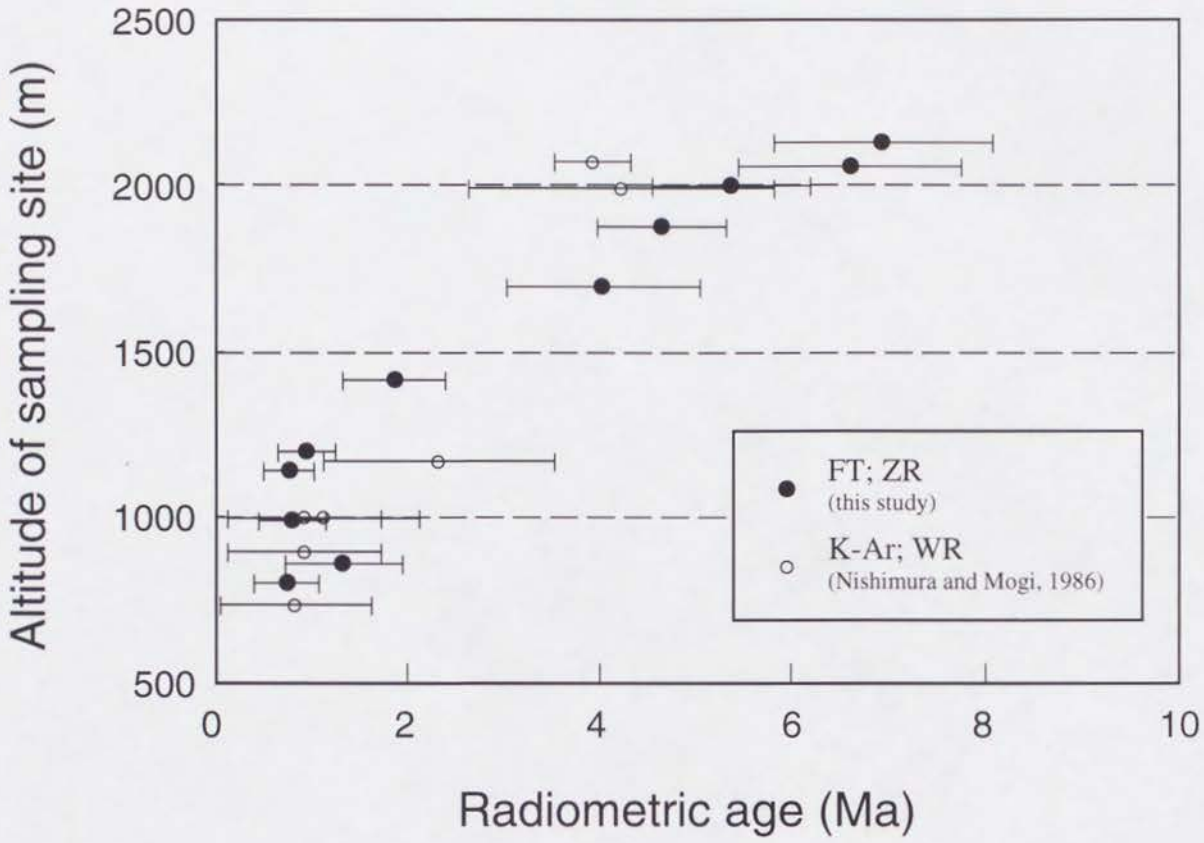

Fig. 10. Zircon FT age variation versus sampling altitude along the Sen–nin Dani Gorge (solid circles). K–Ar (whole rock) ages of Nishimura and Mogi (1986) are also plotted (open circles). *Errors* are 2σ.

4.3. FT Length Data

In order to clarify the meaning of the systematical variation of apparent ages along the Transect C and Transect A, track length measurements are performed for samples collected along these two transects. Measured samples are KRG01, KRG02, KRG07, KRG06, and KRG05 for the samples along the Transect A (Fig. 11), and KRG34, KRG35 and KRG36 for the Transect C, respectively (Fig. 12). In order to increase the number of measurable HCT, ACM is applied for KRG07, KRG02 and KRG01, and HIT for KRG02. Track length can not be measured for the samples corrected at lower than 1100 m along Transect A, because of low track density. Mean track length of all samples are shorter than those of unannealed samples (~10.5 μm; e.g., Hasebe et al., 1994), indicating that these samples were geologically annealed before denudation.

Track length distribution patterns can be recognized by the two components mixture; (a) preexisting tracks shortened to various degrees according to paleotemperature within the bounds of zircon PAZ (ZPAZ) and (b) unannealed tracks with original, long lengths accumulated after cooling down to total stability zone (TSZ).

For the samples along Transect C, where the horizontal age variation is recognized, track length distribution pattern of KRG36 shows the mixture of two components of (a) and (b). This mixture pattern suggests that this sample had long experienced temperatures within ZPAZ. On the other hand, the length distribution of KRG34 and KRG35 show skewed pattern with a tail to shorter lengths of ~ 6 μm, referred as "cooling pattern" of Gleadow et al. (1983). This skewed pattern can be recognized to have been formed during the sample was passing the temperature range of ZPAZ. It implies that KRG34 and KRG35 was placed at total annealing zone (TAZ) and then began to move and passed PAZ at approximately their apparent ages.

For the samples along Transect A, where the vertical age variation is recognized, the mean length reduces with the lower sampling altitude from 2100 m (KRG05) to 1400 m (KRG02), whereas it becomes longer again for the sample at 1100 m (KRG01). The reduction in mean length from KRG05 to KRG02 with lower sampling altitude is explainable by the systematical decrease in mean length of dominant component (a). As for KRG02 and KRG01, mean length and number of tracks of component (a) reduced significantly to make relative ratio of component (b) increase, thus the mean length of KRG01 became longer than KRG02. The mean length of component (a) may have reduced with the higher paleotemperature. This change in distribution pattern of these samples implies the increase in temperature as sampling altitude becomes lower. The existence of shorter tracks (< 10 μm) in KRG05 means that the accumulation of FT started before apparent ages of 6.9 Ma, and that the rock body of KG, from which this sample was collocated, should have intruded and emplaced before 6.9 Ma (maybe >

10 Ma).

For the samples along the Transect A, mean track length and standard deviation of length distribution are plotted against apparent FT age in Fig. 13. With lower sampling altitude, both the mean age and length first show systematic reduction due to the rise in paleotemperature. The mean length decreases to ~ 6 μm (KRG02), then increases again (KRG01), whilst the mean age reduces monotonously to 1 Ma. As a result, plotted data points form a characteristic convex downward trend. Standard deviation has reverse relationship with the case of mean track length, that is concave upward. It may show a part of the course of the process that the narrow distribution became wide, then narrow again as the paleotemperature increased.

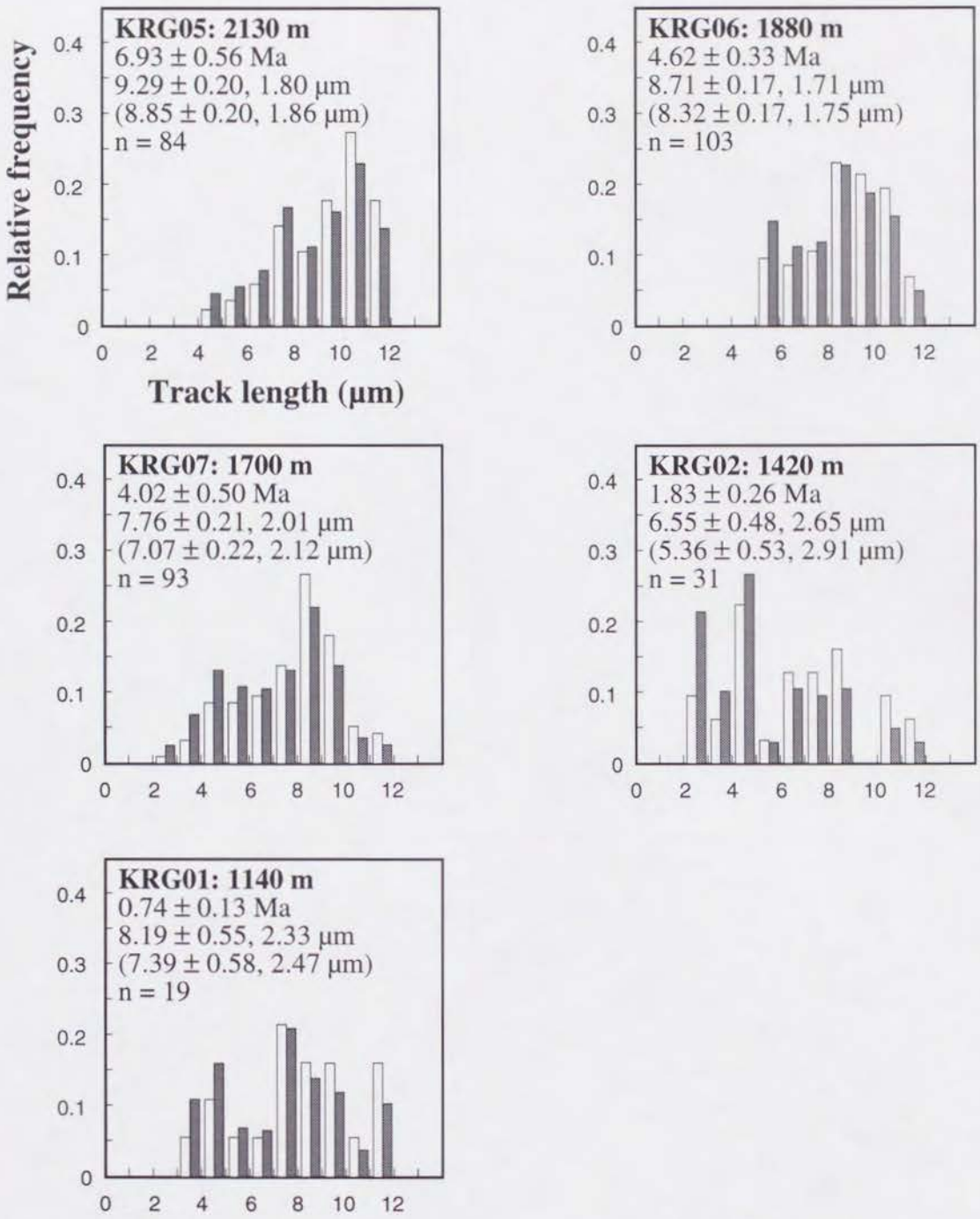

Fig. 11. Confined FT length distribution of zircon samples along the Transect A. The elevations of samples are also shown next to the sample codes. Length distributions are of tracks with angles > 60° to the crystallographic *c*-axis. Zircon FT age, mean track length and standard deviation are also shown (1σ). *n* = the number of tracks measured (> 60°). Shaded bins and values in parentheses are of the distributions for which sampling bias (Laslett et al., 1982) is corrected.

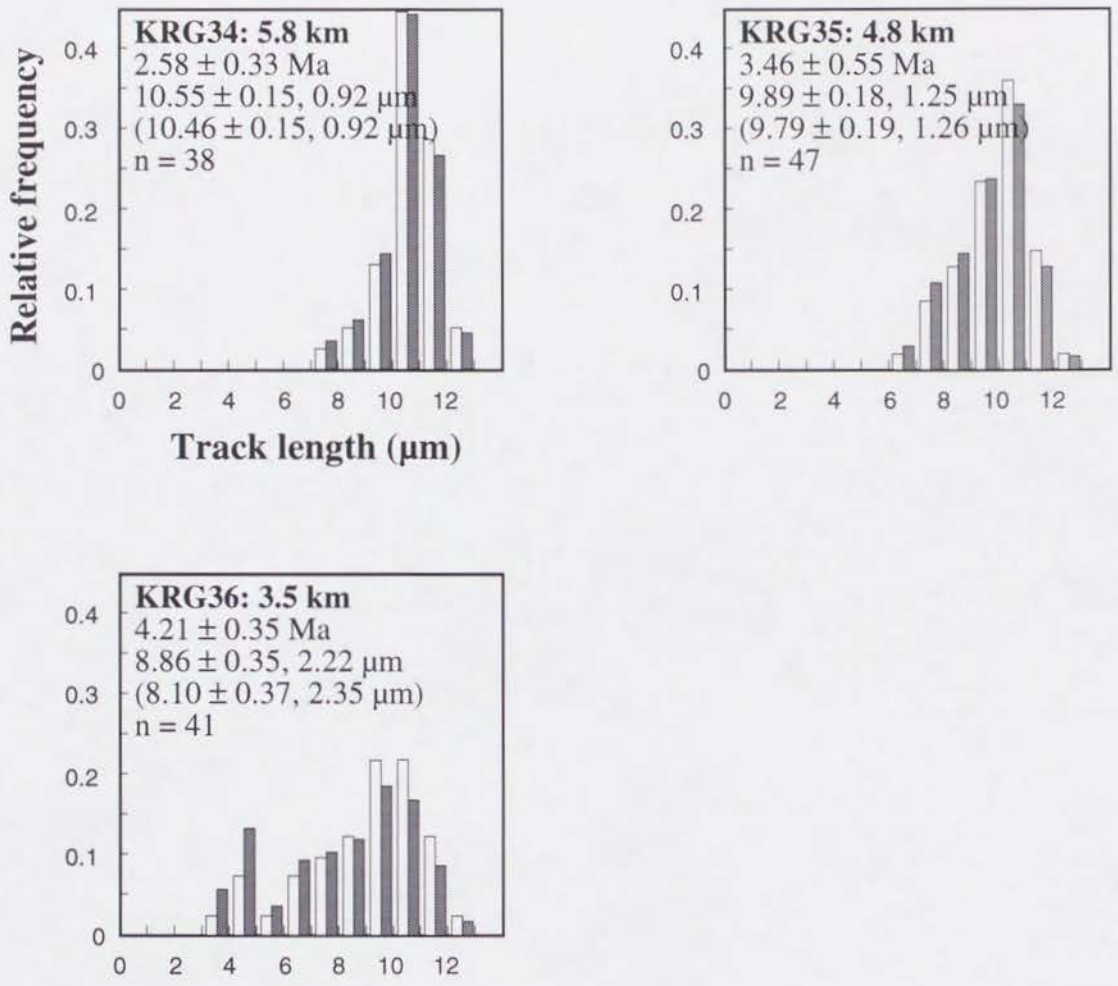

Fig. 12. Confined FT length distribution of zircon samples along the transect C. The distance of samples from the Omachi dam are shown next to the sample codes.

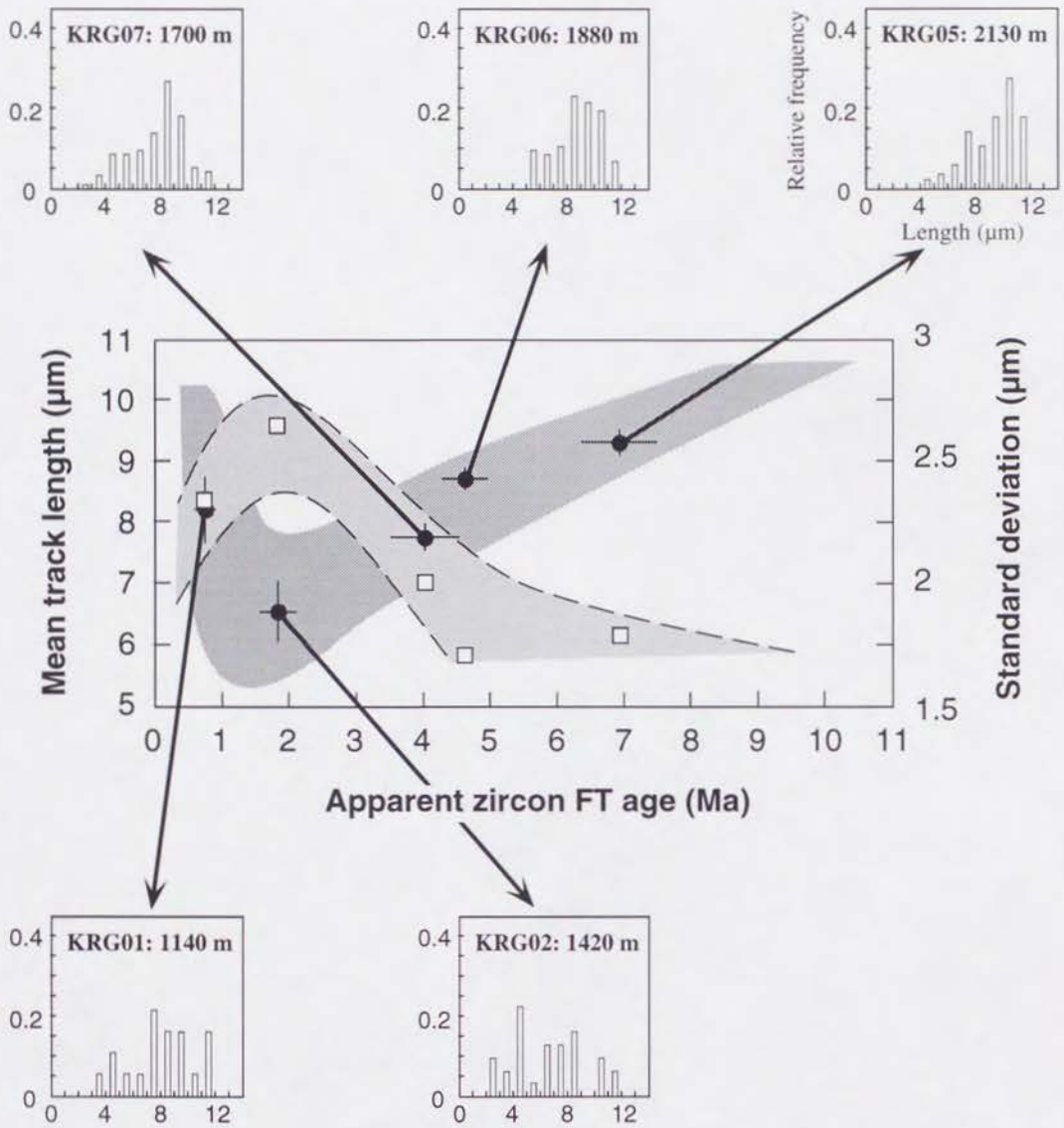

Fig. 13. Mean track length and its standard deviation versus zircon FT age. Plotted data are of the same samples as Fig. 11, collected from relatively higher part along the Sen–nin Dani Gorge. Track length patterns are also shown (bias uncorrected). Solid circles and open squares indicate mean track length and standard deviation, respectively. *Errors* are 1σ of standard errors.

4.4. Thermal History Modeling

Possible thermal histories inferred to yield compatible FT data for samples along the Transect A (Fig. 11) and Transect C (Fig. 12) are shown in Figs. 14 and 15, respectively, using the modeling procedure described in the Section 3.3 and the Appendix A. FT length distribution for modeling is composed of HCTs having the orientation angles > 60° to crystallographic *c*–axis, where the length bias is not collected. Present–day temperature is not given as a constraint for thermal history generation because the significantly higher temperature around ZPAZ is guessed for these samples until recent (e.g., KRG02) based on the qualitative interpretation for track length distribution. The top panels in each figures of Fig. 14 and 15 show the possible thermal histories (200 models) for FT data set of each samples. Thermal histories are approximated by 5 points models. Graphical display of the bottom panel displays the degree of concentration of possible thermal histories. The concentration is expressed as the relative density of models passing in a segment block, which is formed by dividing the temperature axis by 5°C interval and the time axis by the number of steps to approximate a thermal history for forward modeling (100 steps in this study). The density is weighted by the goodness of fit of each model ($E(\mathbf{m})$ in Eq. (I–17)).

The analytical results for the samples of Transect A (Fig. 14) indicate that the temperature of these samples may have decreased to the bound of ZPAZ since 5–4 Ma [4–3 Ma; after the reproductive bias correction (see the Section 3.3)]; In the result for KRG06, the marked bending of cooling rate from 30 °C/m.y. to 100 °C/m.y. is recognized at 1.5 Ma [1 Ma]. The results for KRG07 and KRG02 suggest that the paleotemperature of these samples may have been higher than 200°C until recent (~0.1 Ma). Samples of Transect C were analyzed to have experienced monotonic cooling within the bounds of ZPAZ (Fig. 15). The result for KRG34 suggests the cooling had possibly finished before 1 Ma; this cannot, however, be stated clearly because analysis below the sensitive range is uncertain. Analytical results give the estimate of the cooling rate of 160, 90 and 60 °C/m.y [240, 140 and 90 °C/m.y.] for KRG34, KRG35 and KRG36, respectively.

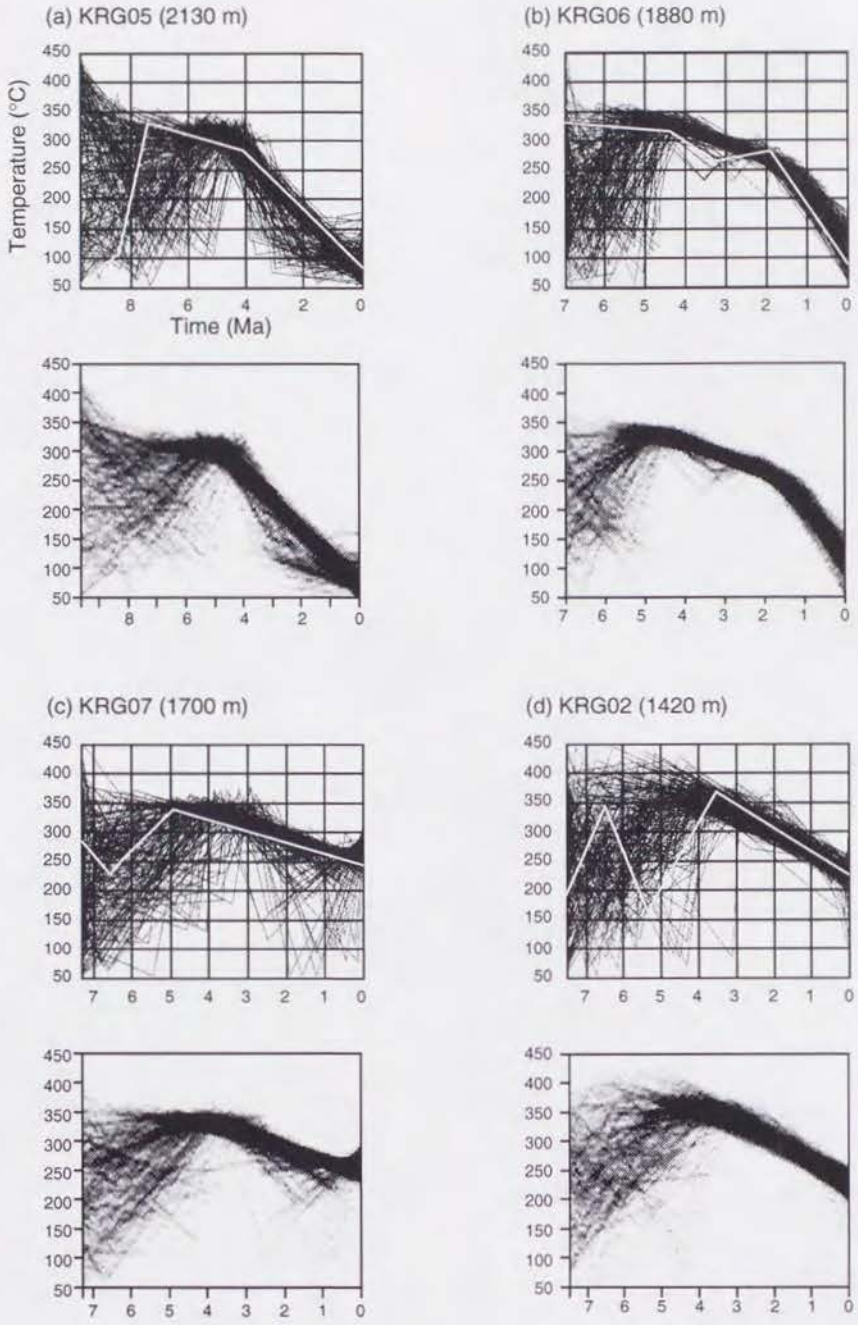

Fig. 14. Thermal histories inferred by the quantitative modeling for some samples of the Transect A. Each thin line with five endpoints is an acceptable model to predict the compatible FT data with the observed ones. 200 models are drown in the upper panel. A white line indicates the best fit bodel in terms of the goodness of fit. The bottom panels display graphically the degree of the concentration of thermal history models yielding compatible data with observed ones. The concentration is expressed as the relative density of models passing in a segment block, which is formed by dividing the temperature axis by 5°C interval and the time axis by the number of steps to approximate a thermal history for forward modeling (100 steps in this study). The density is weighted by the goodness of fit. The index for model density is given in Fig. 15.

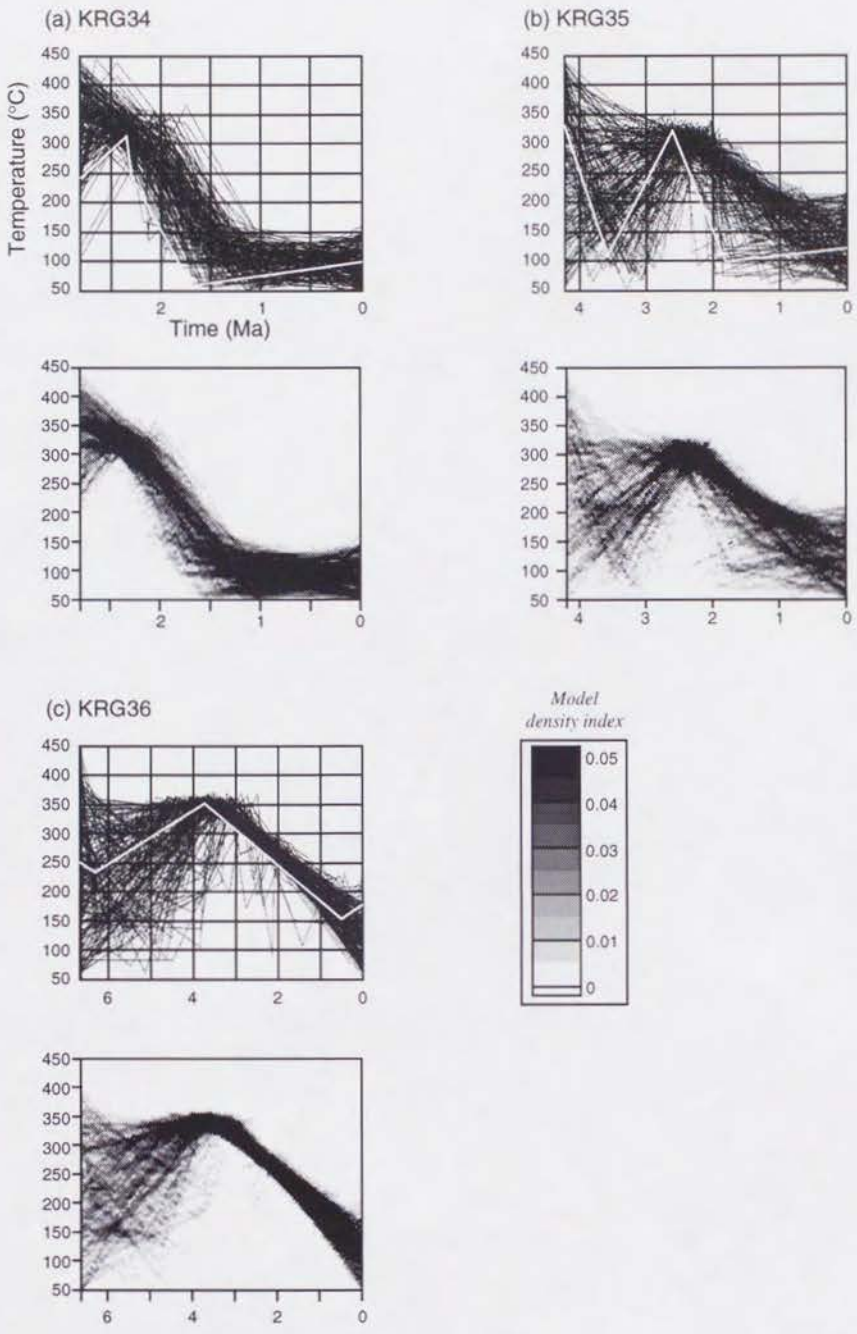

Fig. 15. Thermal histories inferred by the quantitative modeling for some samples of the Transect C.

4.5. Paleotemperature Estimate

4.5.1. Horizontal Variation

Because an apparent zircon FT age approximates the time passed since the sample has been cooled below the middle of ZPAZ, the horizontal variation in the apparent age indicate the variation in the mean cooling rates of a series of samples along the Transact C. In addition, track length histograms of KRG34, KRG35 and KRG36 give the constraints on the past position of these samples in terms of ZPAZ as shown in Fig. 16A. The broader distribution pattern for KRG36 indicates that this sample should have been located within ZPAZ. The skewed pattern for KRG35 with relatively small ratio of shorter track component indicates that this sample was located TAZ before cooling started, and it has passed the middle of ZPAZ at ~ 3.5 Ma, which approximates the timing when remaining tracks had begun to accumulate. Based on the information about the past position of these samples in terms of ZPAZ and apparent FT ages, the cooling of the samples along the Transect C is interpreted to have begin at ~ 4 Ma.

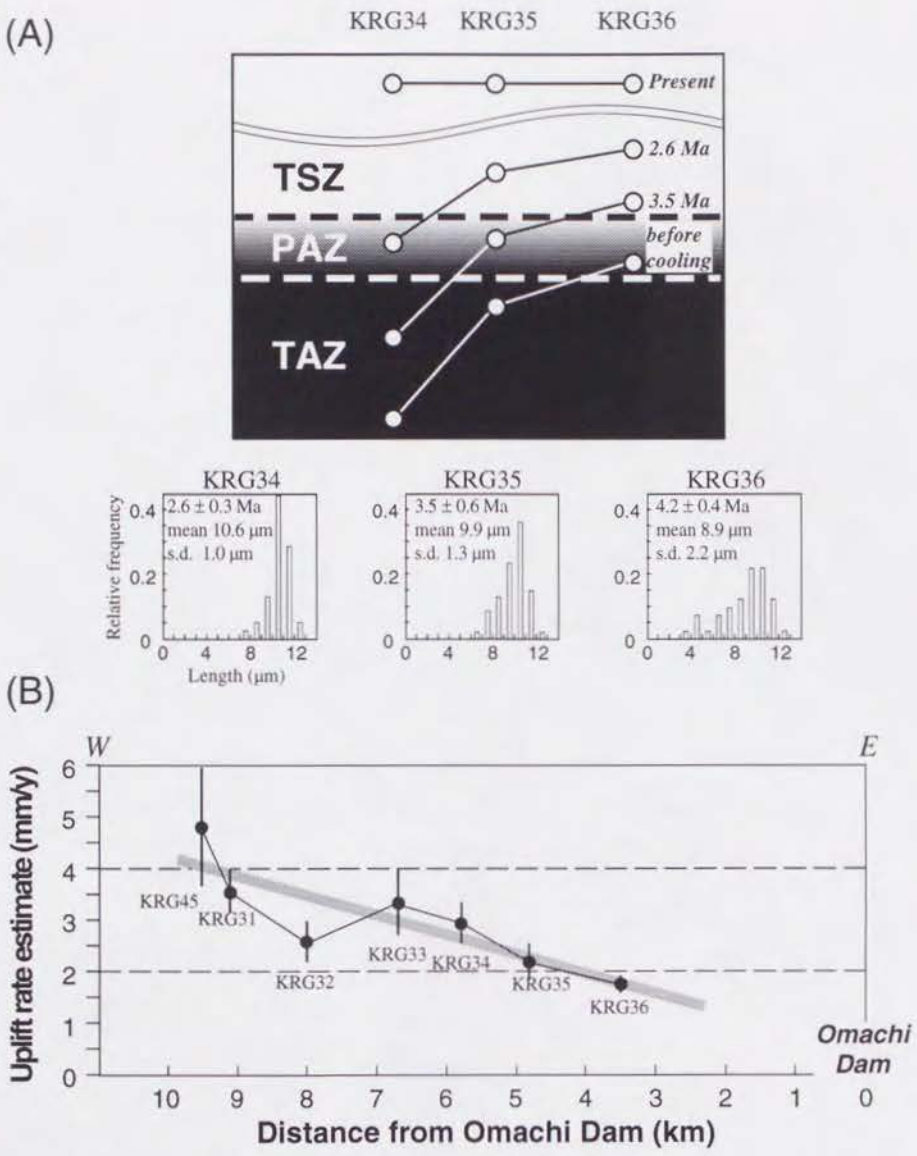

Fig. 16. (A) Schematic diagram of past position of samples of KRG34, KRG35 and KRG36 in terms of PAZ, together with the track length histograms. Apparent age (1σ), mean track length and the standard deviation (*s.d.*, 1σ) are given. The histogram of KRG36 with many shorter tracks indicates that this sample should have suffered the temperature within the bounds of PAZ before uplifting. The skewed pattern of KRG34 and KRG35 indicate that these samples were located in TAZ before uplifting and passed PAZ at a certain rate after uplift started. (B) First order estimates of uplift rate of samples with "younger" ages along Transect C where initial geothermal gradient was assumed 40 °C/km. Uplift rates of each samples were obtained by dividing the depths which correspond to the middle of ZPAZ by their apparent ages, indicating the minimum estimates. Horizontal axis is the distance from the Omachi Dam. A shaded line was drown to approximate the relation between uplift rate and the distance, suggesting the tilted uplift eastward. The tilting axis can be given by the extrapolation of this line to uplift rate = 0 mm/y, which corresponds roughly the location of Omachi Dam, where the boundary between "younger" and "older" age samples was recognized in the neighborhood. *Errors* are 1σ.

4.5.2. Vertical Variation

In order to explain the systematical variation of the apparent age recognized in the central part of KG, the plot of mean track length versus apparent age, together with track length distribution patterns, is compared with that of a previous study with different geological setting (Fig. 17). The diagram in the Fig. 17 shows the variation of apparent zircon FT ages and length histogram of the Cretaceous sandstone samples which suffered secondary heating by the plutonic intrusion at 15 Ma (Tagami and Shimada, 1996). The similarity of plot pattern with convex downward is recognized between Fig. 13 and Fig. 17, suggesting that samples in Fig. 13 existed at variable temperatures within ZPAZ. The track length histograms of KRG05, KRG06, KRG07 and KRG02 correspond roughly SMTZ54, SMTZ44, SMTZ19 (or SMTZ23) and SMTZ12, respectively. These correspondence are characterized by the variation of length histogram from the unimodal skewed pattern with longer mean length (SMTZ54, KRG05) to the broad one with rather shorter (SMTZ12, KRG02). KRG01 may correspond the pattern between SMTZ12 and SMTZ07 because the ratio of component (1) to (2) for KRG01 may correspond to the middle of those for SMTZ12 and SMTZ07.

Although no length data set could be collected to exactly indicate the top or bottom of ZPAZ, the apparent ages correspond to the top or bottom can be approximated as follows (Fig. 18). The bottom of ZPAZ is given by the apparent age of 1 Ma because zircon FT ages of the samples corrected at lower altitude than 1100 m are concordant around 1 Ma. The top of ZPAZ is given by the apparent age approximated as 9.1 ± 1.1 Ma (1σ), by extrapolating the regression line for the four older samples (Fig. 18) to the mean length of 10.5 μm, which value is expected for samples located in the TSZ of FT (e.g., Hasebe et al., 1994). Comparison of two diagrams (i.e., Fig. 17 and Fig. 18) can give the explanation for the concordant of FT ages of ~ 1 Ma. Samples with present altitude higher than 1100 m were located at the altitude corresponding to ZPAZ. This fact indicates that KG with these samples have cooled rapidly at ~1 Ma. The rapid cooling at 1 Ma is also suggested by the marked bending of cooling rate in the thermal history analysis for KRG06.

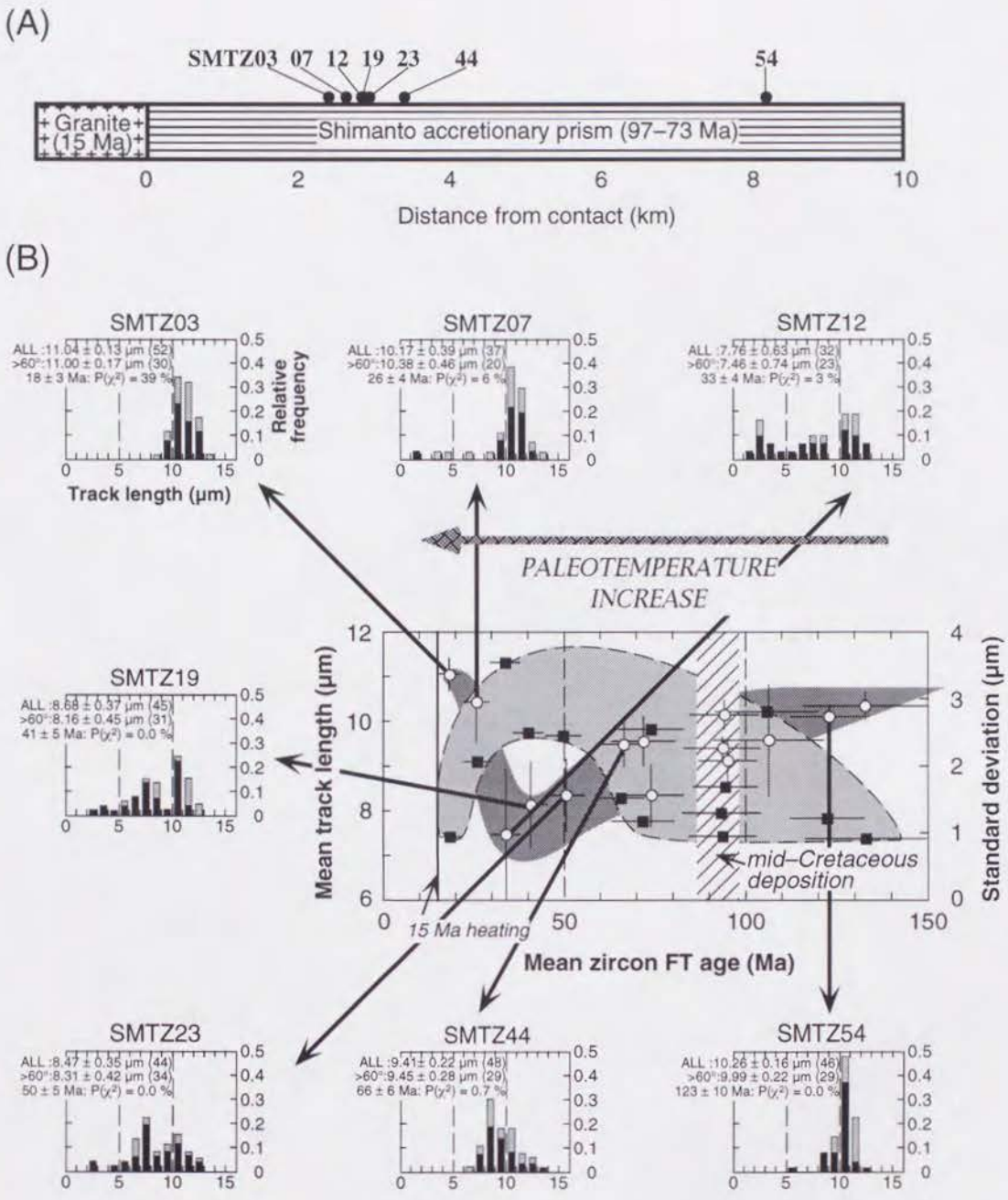

Fig. 17. Mean zircon FT age versus mean track length for the Cretaceous sedimentary rocks reheated by 15 Ma granitic intrusion, modified after Tagami and Shimada (1996). (A) Sample location from the intrusion contact. Zircon samples were collected from sandstone beds of coherent units of the Shimanto Belt. (B) The variation in relationship between FT age and mean track length (open circles) or its standard deviation (solid squares). Track length plots are added to show the variation in length distribution pattern according to the distance from the intrusion contact. Plotted data of mean track length present a characteristic trends convex downward, with its right end predating deposition and the left one coincident with the time of granite intrusion, whilst those of standard deviation a characteristic trends convex upward. *Errors* are 2σ.

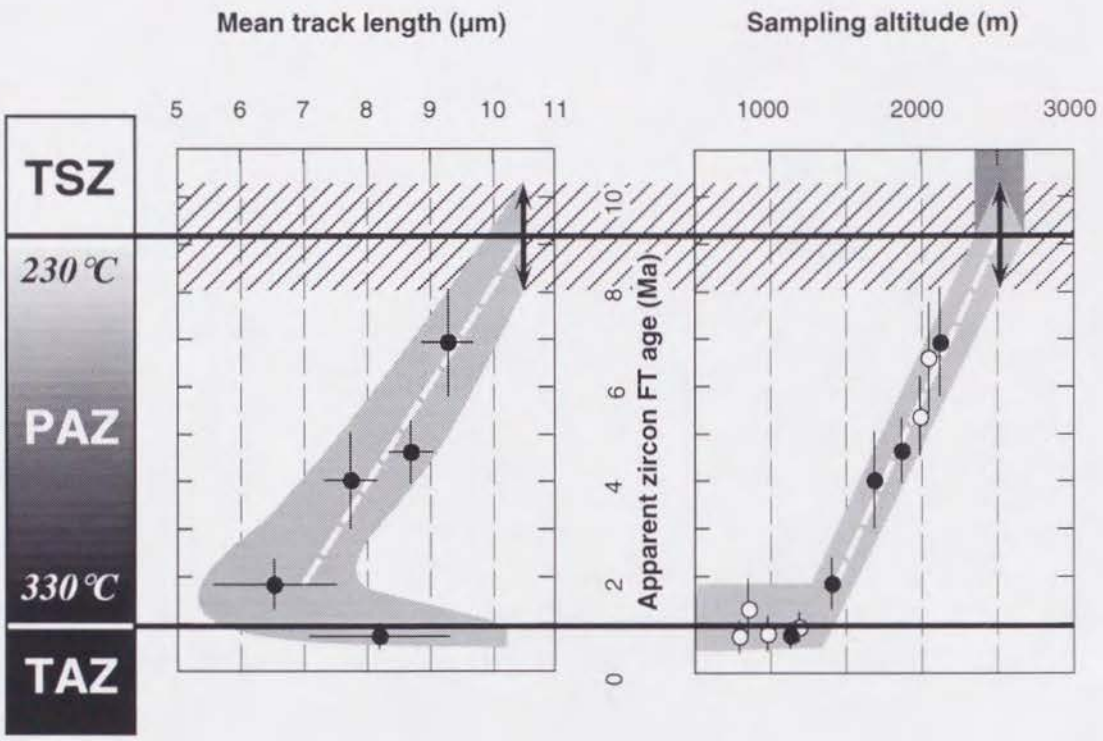

Fig. 18. The relationship among mean track length, sampling altitude, apparent zircon FT age, and fossil zircon partial annealing zone. The left panel shows the temperature scale in terms of the partial annealing zone. TSZ = total stability zone; PAZ = partial annealing zone; TAZ = total annealing zone. Solid circles in the right and central panels are the same data as Fig. 13. Open circles are of data without length measurements. The bottom of PAZ was estimated to correspond to the apparent ages of 1 Ma. The top of PAZ was estimated as 9.1 ± 1.1 Ma (1σ; striped zone) by extrapolating the regression line for the four older samples (white dotted line in the middle panel; correlation coefficient = 0.96) to the mean track length of 10.5 μm. The sampling altitude corresponding to the top of PAZ can be obtained as 2500 ± 200 m by extrapolating the regression line for the data of samples collected at > 1100 m (white dotted line in the right panel; correlation coefficient = 0.98) to the corresponding apparent age zone. *Errors* are 2σ.

4.6. Paleo–Geothermal Gradient

The estimates of temperature and altitude range of ZPAZ allow the evaluation of the geothermal gradient when the rapid cooling began in the central part of KG. By comparing the sampling altitude–apparent age plot (Fig. 10) and the mean track length–apparent age plot (Fig. 13), the present altitude corresponding to the bottom and the top of ZPAZ can be obtained as 1100 m (sampling altitude of KRG01) and 2500 ± 200 m (1σ), respectively (Fig. 18). Laboratory annealing experiments give the temperature range of ZPAZ as 200–350°C for the heating duration of 10^6 y (Yamada et al., 1995b). This temperature range varies according to the range of track length reduction defined for ZPAZ. With constraints from geological evidences, Tagami and Shimada (1996) proposed the estimation of ZPAZ as 230–330°C for the heating duration of 10^6 y. Geothermal gradient at the beginning of rapid cooling at 1 Ma are evaluated using the ZPAZ range of 230–330°C and 200–350°C as 70 ± 10 °C/km and 110 ± 15 °C/km, respectively (1σ). They are significantly higher than that of 40 °C/km, which is observed for the surrounding region of the N. Alps at the present time. However, these high geothermal gradients are concordant with the present–day geothermal gradient in the central part of KG, which can be estimated as ~ 80 °C/km by dividing the present temperature of the high temperature zone (~ 160 °C; e.g., Matsui and Yoshida, 1962) by the depth of the Kurobe Gorge (~ 2000 m). These estimates of the geothermal gradient suggest that the high geotherm area may have locally existed in the central part of KG since 1 Ma in the central part of KG.

5. Uplift History of Rock Bodies in the Northern Alps

5.1. Thermo–Tectonic History

5.1.1. Across the Mountain Range

In the low temperature range of FT retention, tectonic uplift is the most important geological process causing rock cooling. As the rock column is lifted towards the surface, it cools continuously, provided the surface layers are equally removed by denudation and the geothermal gradient stays constant (i.e., the track retention isotherm stays at constant depth). Then the mean uplift rate can be calculated from the cooling rate according to

uplift rate = cooling rate / geothermal gradient.

For the cooling ages with the horizontal variation recognized for the samples along the Transect C at the almost constant altitude, two different geological scenarios can be given to produce such variation (c.f., Wagner, 1990): (a) The different uplift rates of the samples, assuming a regionally equal geothermal gradient. (b) The inclination of the isotherms assuming a horizontal thermogradient within the crust. In this situation, a horizontal geothermal gradient within the local area of 10 km width (from the Omachi–dam to the Takasegawa Fault) is geologically unrealistic assumption, therefore the former explanation is more plausible. Because the apparent ages become younger westward along this transect, the uplift rate of western part may have been greater than that of eastern part (Fig. 16B). This systematical difference in the uplift rate implies the uplifting tilted eastward.

The first order estimates of mean uplift rate of samples with "younger" ages along the Transect C as shown in Fig. 16B. The regionally equal geothermal gradient is assumed as 40 °C/km while uplifting, the altitude of mountain height as mean sea level (0 m), and the middle of ZPAZ (260°C) as -6.5 km then. Uplift rates of each samples are obtained by dividing the depth which corresponds to the middle of ZPAZ (-6.5 km) by their apparent ages, indicating the minimum estimates for each samples. A shaded line, which was drown to approximate the relation between uplift rate and the horizontal position, suggests the tilted uplift (or differential uplifting) eastward as a whole. Tilted uplift is previously reported for the Takidani Granodiorite distributed to 20 km south of the N. Alps (Harayama, 1992; Fig. 1C). The tilting axis can be given by the extrapolation of this line to uplift rate = 0 mm/y (Fig. 16B). It corresponds roughly the location of Omachi Dam, where the apparent gap of FT age is recognized. If all of samples located from the Omachi–dam to the Takasegawa Fault uplifted simultaneously, uplifting may have lasted until at least 1.6 Ma (apparent age of KRG45). These estimates imply that the uplifting with tilting eastward started at 4 Ma, which is indicated by the initiation of cooling of KRG36, and the uplifting stopped at < 1.6 Ma. The estimate of the initiation timing of uplifting is concordant with the results of the thermal history analysis that

KTG05 and KRG06 were in cooling phase at ~3 Ma, implying the uplift was already started then. The termination timing is also concordant with the results that cooling of samples along Transect C ended at ~ 1 Ma (Fig. 15).

The amount of the vertical motion of KRG43, located by the west side of the Takasegawa Fault, can be estimated according to the thermochronologic constraints that its apatite FT age (closure temperature of ~ 100 °C) was reset, whilst the zircon FT age (~ 260 °C) not (Table 3). The vertical motion of this sample can be restricted within the range between 2.5 and 6.5 km compared to the present position, because closure temperatures of apatite and zircon FT system can be converted to 2.5 km and 6.5 km, respectively, assuming the geothermal gradient = 40 °C/km, the surface temperature = 0°C, and the mountain height = 0 m.

5.1.2. Central Part of the "Younger" Granite

In the age–depth profile for the samples of the central area of KG (Fig. 10), zircon FT ages increase systematically with altitude, but the pattern is marked by a significant "break in slope" (c.f., Fitzgerald et al., 1986) at 1 Ma. The upper (older) part has a shallow gradient, whilst the lower (younger) has an extremely steeper gradient. The "break" has been interpreted as the base of a ZPAZ that has been uplifted to its present position (Gleadow and Fitzgerald, 1987). The "break in slope" therefore approximates the time at which uplift of this area began. The extremely steeper gradient suggest the rapid uplift rate of this region.

Correlation between the depth and ZPAZ when uplift of Stage II started can provide the assessment of the uplift amount of RUZ, assuming the monotonic geothermal gradient for any depth. The first order estimates of the uplift amount during the Stage II are summarized in Table 4. Factors which affect the estimation of paleo–altitude corresponding to ZPAZ are height of the mountain range and geothermal gradient at the beginning of Stage II. Assuming the mountain height of 1500 m and the monotonic geothermal gradient at any depth, the paleo–altitude of ZPAZ bottom at the beginning of Stage II is calculated as -3.1 ± 0.6 (-1.8 ± 0.5) km for the ZPAZ range of 230 – 330°C (200 – 350°C). The amount of uplift is evaluated as 4.2 ± 0.6 (2.9 ± 0.5) km by subtracting these estimates from the present–day altitude of 1.1 km for KRG01, which correspond to the bottom of ZPAZ.

5.1.3. Two–Stage Uplift

The initiation timing of the uplift of the rapidly uplifted zone (RUZ) is significantly different from that of the samples along Transect C estimated as 4 Ma. This difference implies that the uplifting of the N. Alps is divided at least two stages in terms of timing as; Stage I: started at 4 Ma, finished before ~1 Ma; Stage II: rapid uplift at 1 Ma. Whether uplift had paused between Stage I and II cannot be verified because it is too much detailed discussion for the age determination error. The uplift prior to 1 Ma uplifting of RUZ is assumed previously (e.g., Ikeda, 1990) based on the geological evidence of the distribution of granitic conglomerates supplied from the N. Alps in the Northern Fossa Magna area (e.g., Hirabayashi, 1970). Because this stage was accompanied with tilting across the mountain range, whole region of the N. Alps may have uplifted then.

Table 4. Estimates of Paleo–Geothermal Gradient at 1 Ma and Subsequent Uplift Amount

ZPAZ range (10^6 m.y.)	Present altitude of ZPAZ top (km)	Present altitude range of ZPAZ (km)	Geothermal grad. (at 1 Ma) (°C/km)	Paleoaltitude of ZPAZ bottom (km)	Amount of uplift (km)
230–330°C	2.5 ± 0.2	1.4 ± 0.2	71 ± 10	-3.1 ± 0.6	4.2 ± 0.6
200–350°C	2.5 ± 0.2	1.4 ± 0.2	107 ± 15	-1.8 ± 0.5	2.9 ± 0.5

Paleoaltitude was given assuming the mountain range height of 1500 m and the constant geothermal gradient for any depth at 1 Ma. *Errors* are 1σ.

5.2. Quantitative Assessment of Uplift Parameters

High geothermal gradient at the beginning of Stage II should have been caused by the previous uplifting of Stage I. For more plausible evaluation of amount and rate of uplifting for Stage II, the vertical temperature distribution should be described at the end of Stage I, because the geothermal gradient should not be vertically constant in the case of rapid uplifting, which causes the compaction of geothermal gradient (c.f., Stüwe et al., 1994; Fukahata, 1995). In order to obtain temperature distribution at the end of Stage I, the variation of mountain height and underground temperature distribution (below the surface) is modeled in terms of a given uplift rate history and the consequent denudation. A term of "denudation" is defined here as the process of erosion associated with the rise in mountain surface by uplifting. "Uplift" is referred here as the displacement of rocks with respect to the mean sea level. Therefore the change in mountain height differs from the amount of rock uplift, by the amount of erosion (i.e., "exhumation"). The detailed modeling procedure is described in the Appendix B.

The model setting is as follows: (1) Before the Stage I, a steady state is assumed, with the height of mountain surface of sea level (= 0 m) and underground temperature distribution controlled by an initial geothermal gradient. (2) Uplift starts suddenly at a constant rate and lasts during a certain duration. (3) Mountain height varies according to rock uplifting and consequent denudation with the erosion rate in proportion to the mountain height. (4) Temperature distribution varies according to heat transfer by advection (rock movement) and heat conduction.

The driving forces of uplifting proposed previously are the horizontal compression of plate tectonic origin (e.g., Fukao and Yamaoka, 1983) or magmatic intrusion to the upper crust (e.g., Ikeda, 1990). If the uplift was accompanied and caused by a magmatic intrusion, it should have acted as a heat source to increase the geothermal gradient. Therefore, two types of boundary conditions were assumed; A: without heat source, B: with heat source at the bottom of the upper crust.

A geological constraint for uplift rate was given by the Jurassic to Cretaceous Tetori Group found to rest on the western marginal area of the N. Alps granites at the altitude ~2600 m (Harayama et al., 1991). Because the maximum thickness around the N. Alps region is ~1000 m, the amount of Stage I uplift should not so much greater than 4000 m. Therefore the uplift amount at the central part of the N. Alps, which was possibly greater than that at the marginal area, was assumed at most 8 km.

In the case of uplifting without heat source, the mountain height and the geothermal gradient at the end of Stage I obtained by modeling are plotted for various cases in Fig. 19A. The mountain height is represented as the mean altitude of the whole mountain range of the N.

Alps. The input parameters here are initial geothermal gradient, constant uplift rate, and uplifting duration; the output parameters are height of mountain and geothermal gradients at the temperature range of ZPAZ. Some of input parameters were restricted as follows; Initial geothermal gradient of 30, 40, 50 or 60 °C/km, and uplifting duration of 2 or 3 m.y. (c.f., discussion on the tilted uplifting). As a result, mean altitudes are almost proportional to uplift rates regardless of other factors. Estimated geothermal gradient increases according to the higher initial gradient, longer uplift duration, and higher uplift rate. The dominant factor is uplift rate. According to the geological constraint on the uplift amount, uplift rates < 4 mm/y or < 3 mm/y are expected for the uplift duration of 2 or 3 m.y, respectively. Fig. 19A shows that the resultant geothermal gradient of 70 °C/km (ZPAZ of 230–330°C) require the combination of initial geothermal gradient and uplift rate of (60 °C/km, 3 mm/y) for 2 m.y. Geothermal gradient of 110 °C/km may not be realized under any condition.

Fig. 19B shows the results in the case of uplifting with heat source. As a heat source, magma of 700 or 800°C was assumed to have intruded directly under the upper crust at 15 km depth, implied by the seismic–aseismic boundary around the N. Alps region (e.g., Wada et al., 1990). It is assumed that the intruded magma also uplifts at the same rate, raising up the existing upper part (see the Appendix B). As a result, geothermal gradient at the end of Stage I increases according to the higher intrusion temperature, longer uplift duration, and higher uplift rate. The effect of initial geothermal gradient is little. In order to realize the consequent geothermal gradient of 70 °C/km, uplift rates are required as 3 mm/y for the duration of 2 m.y. or 2 mm/y for 3 m.y. with the heat source of 700 °C, and 2–3 mm/y for 2 m.y. or 2 mm/y for 3 m.y. with 800 °C. Geothermal gradient of 110 °C/km may not be realized under any condition.

These modeling results and a geological constraint deny the possibility that uplifting without heat source during 2–3 m.y. caused the compaction of geothermal gradient from 30 or 40 °C/km to 70 °C/km. If the geothermal gradient at the end of Stage I was 50 °C/km, the temperature at 15 km depth was estimated as 750 °C. They suggest that the geothermal gradient at the beginning of Stage I was significantly higher than that of surrounding area of RUZ at present, or Stage I uplift was accompanied with heat source; anyway the stage I may be related with magmatic intrusion. Based on the modeling results, one of the example set of presumable parameter for the uplifting with heat source is assumed as follows; heat source temperature of 800°C, uplift duration of 3 m.y., and uplift rate of 1.5 mm/y. For these parameters, Fig. 20 shows the temperature distribution and the vertical motion path of samples located at certain present altitude, according to the calculation by the procedures descried in the Appendix B. The assumed uplift rate history in the Fig. 20A are decided as follows; uplift rate during Stage I is chosen to derive the total uplift amount preferred by a geologic constraint on the Tetori Group, and RUZ uplifts within a shorter duration (assumed as 0.5 m.y. here) at the Stage II. The

resultant diagram (Fig. 20B) suggests the existence of high geothermal gradient zone beneath the central part of the N. Alps. This suggestion is concordant with the existence of hot material at the relatively shallower zone of about 10 km (e.g., Hirahara et al., 1989; Wada et al., 1990, 1994; Katsumata et al., 1995). This diagram gives the estimates of geothermal gradient for the temperature range of ZPAZ at 4 Ma, 1Ma and present as approximately 40, 70, and 70 °C/km, respectively. It implies that the estimated geothermal gradient remains almost constant after it became approximately 70 °C/km at the end of the Stage I, although the mountain height has varied during Stage II. The calculation result is consistent with the present estimate of geothermal gradient around the high temperature zone of KG of ~ 80 °C/km (see the Section 4.6).

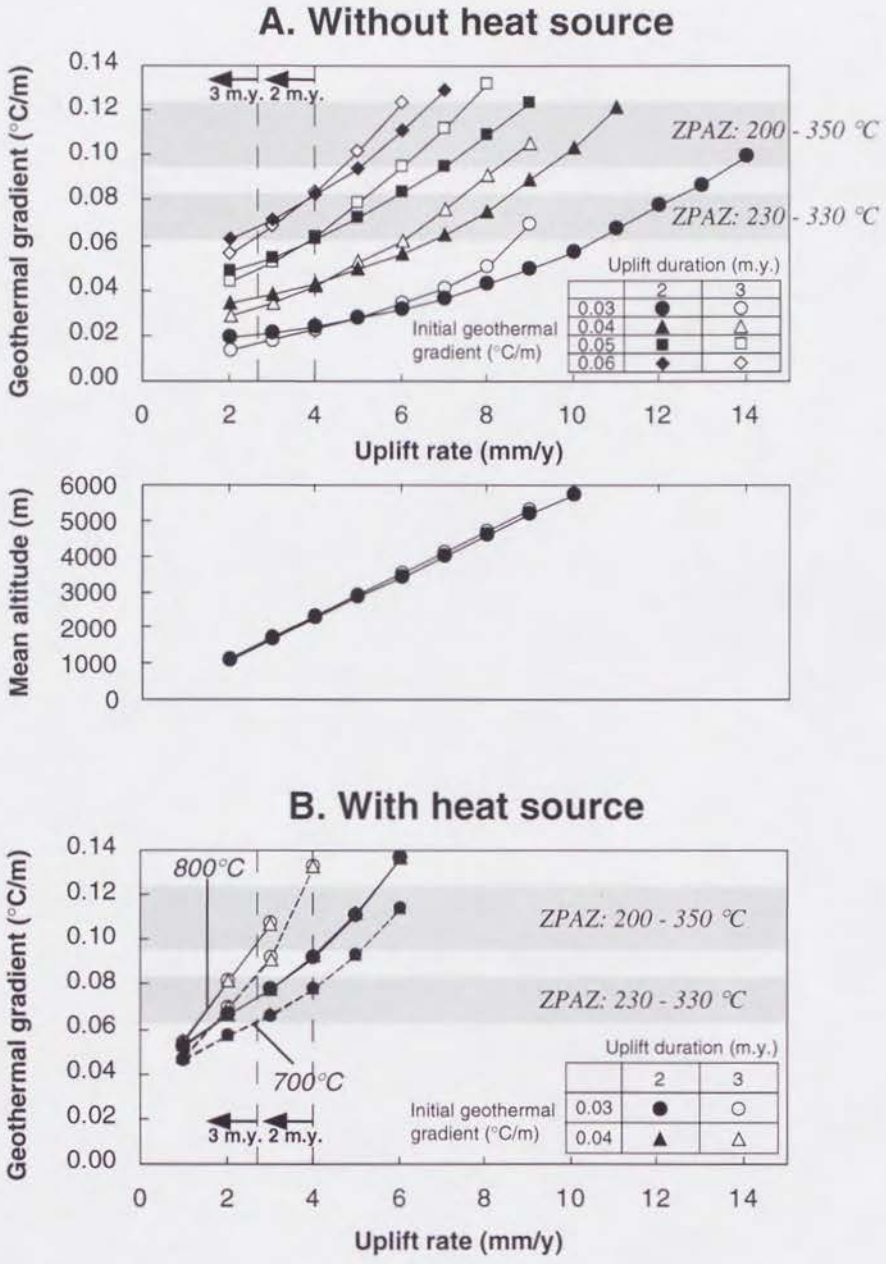

Fig. 19. The variation in geothermal gradient and resultant mean altitude of the summit level according to uplifting with various conditions, obtained by model calculations. A: uplift without heat source; B: uplift with heat source. Constant uplift rates are given in the horizontal axes. The effect of initial geothermal gradient before uplifting and the uplifting duration are indicated with different symbols, as shown in the legend. Dotted lines indicate the maximum uplift rate for the duration of 2 m.y. or 3 m.y., suggested by a geological constraint of the distribution of the Tetori group (see text). Resultant mean altitude of summit level are independent of other factors than uplift rate, because the rate of uplift and erosion are in equilibrium for the duration of a m.y. order.

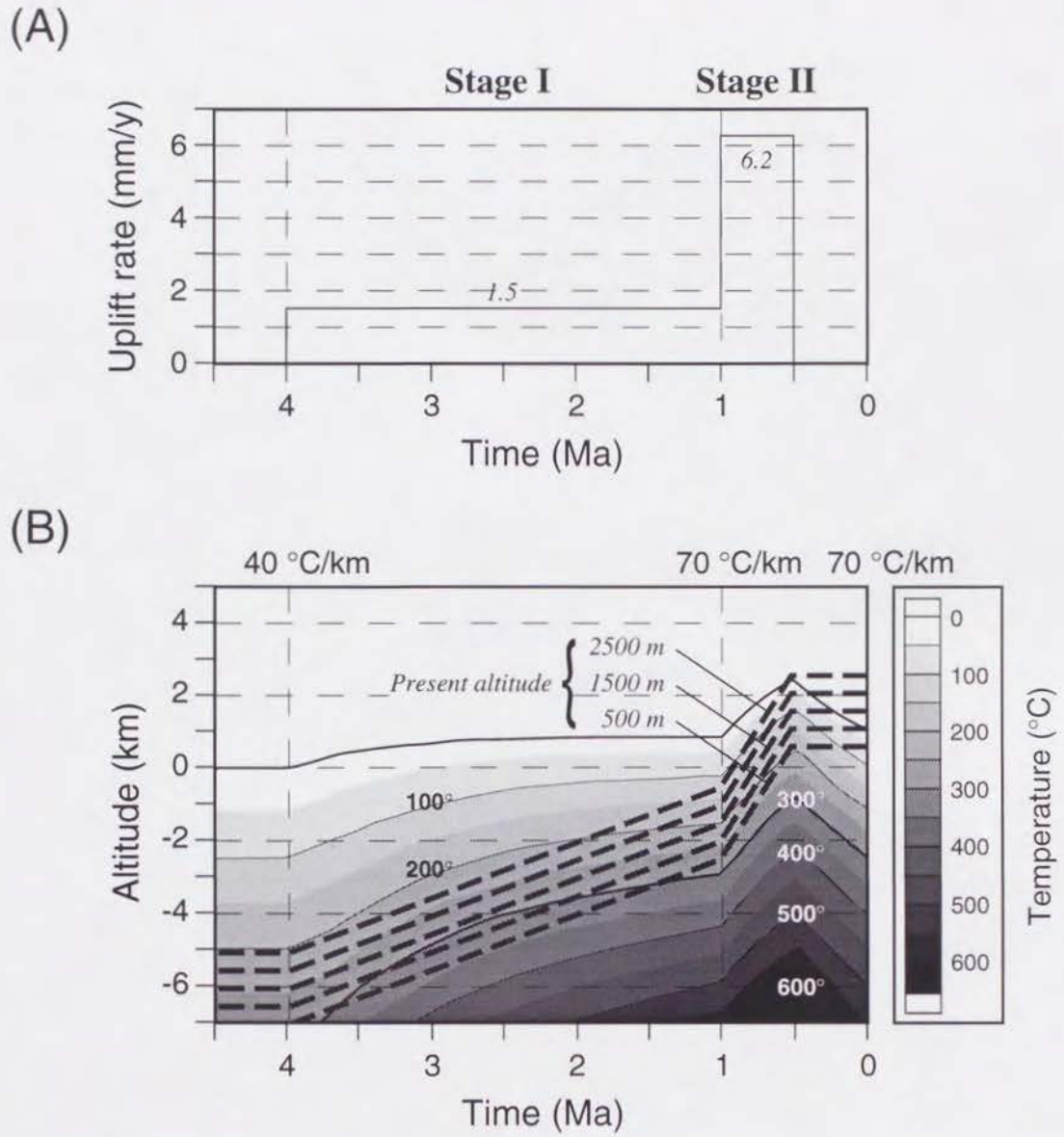

Fig. 20. The variation of calculated temperature distribution and the vertical motion path of samples located at certain present altitude. (A): A presumed uplift rate history according to the modeling results and a geological constraint on the distribution of Tetori Group. Two events were assumed to change the uplift rate at 4 Ma and 1 Ma. (B): Variation in the underground temperature distribution and the paths of samples for the given uplift rate history. Solid line indicates the change in mean altitude. The sample paths are indicated by dotted lines. Note that there are some cases where the altitude of a sample becomes higher than mean altitude. Estimates of geothermal gradient are also shown at 4 Ma, 1Ma, and present for the temperature range of ZPAZ (i.e., 230–330°C).

6. Tectonic Implication on the Orogenic History of the Northern Alps

Based on the FT thermochronologic analysis, two stages of uplifting since 4 Ma are summarized below (Fig.22).

Stage I is characterized as the uplift of the whole region of the N. Alps started ~ 4 Ma, finished before ~1 Ma (Fig. 22A). Magmatic intrusion likely have accompanied with this stage to increase geothermal gradient from 40 to 70 (or 110) °C/km. Eastward tilting is recognized in this stage. The west side of tilted area is limited by N–S trending faults (e.g., Takasegawa Fault), across which the apparent gap of FT age is recognized. Based on the parameters given by the modeling, uplift of Stage I can be described as follows; in the upper crust with an initial geothermal gradient of 40 °C/km, RUZ started uplifting at 4 Ma accompanied with a heat source of 800°C. Uplift had lasted until 1 Ma at the rate of 1.5 mm/y. Consequent mean altitude of mountain range and geothermal gradient at the end of Stage I were 0.9 km and 70 °C/km at the temperature range of ZPAZ. The altitudes corresponding to ZPAZ of 230–330 °C are estimated as -3.4–-2.0 km.

This stage of uplifting might be also characterized as domal uplift of the area of ~50 km width (Fig. 22A). Based on the survey of Tetori Group which is considered as fluvial deposit and distributed in the western part of the N. Alps, many blocks were recognized divided by many normal faults dipping eastward steeply (Harayama et al., 1991). The height of distribution area of Tetori Group increases eastward up to ~2600 m (Fig. 21). This inclined distribution should have been brought by the later tectogenesis of westward tilting due to the uplifting of the central part of the N. Alps. The timing of this tilting has not been clarified yet, but if the westward tilting at the western part of the central part of the N. Alps synchronized with the eastward tilting at the east side, the same cause could be assumed. In that case, domal uplifting of the central N. Alps might have been derived by magmatic intrusion. Consequently, there may have existed the high geothermal gradient zone beneath the central part of domal uplifting in the shallower zone. According to the model calculation result in Fig. 20, the temperature at the depth of 5 km at 1 Ma is approximately 400°C, which corresponds to the temperature of brittle–ductile boundary (Ito, 1990). The domal uplifting derived by a magmatic intrusion may have caused the locally tensile stress field in the shallow zone of the mountain range. This tensile field might have induced the activity of the monogenic volcanoes at around 2.7–1.6 Ma in the southern part of the N. Alps region, which were reported by Shimizu and Itaya (1993).

Stage II is characterized as the uplift of RUZ at around 1 Ma (Fig. 22 B). The geothermal gradient had already increased to relatively high (70 or 110 °C/km) at the beginning

of this stage. Mean uplift rate since 1 Ma was estimated as 4.2 ± 0.7 mm/y (1σ; 70 °C/km) or 2.9 ± 0.5 mm/y (110 °C/km). Given the parameters by the modeling, total amount of uplift of Stage II can be assessed as 4.6 km by subtracting these estimates of past altitude from present altitude of ZPAZ (Table 4). The minimum estimate of the uplift rate of Stage II can be given by dividing total amount of uplift by uplift duration (from 1 Ma to present time) as 4.6 mm/y. Rather higher uplift rate is expected to achieve the present mean altitude of ~ 2000 m; an expected rate may be > 4 mm/y (see the bottom panel of Fig. 19A), assuming the erosion time constant adopted here (0.6 m.y.; see Appendix B). The uplifted zone may correspond the particularly high geothermal gradient zone, which had appeared at the end of Stage I. This ductile zone may have been pressed and lifted by horizontal compression of plate tectonic origin (e.g., Fukao and Yamaoka, 1983) at the Stage II. The northern edge of the uplifted zone may correspond to the boundary between KRG53 and 94914–3, where apparent age gap was recognized (Fig. 8D). It is suggested that the southern edge may correspond to the part that the Takasegawa Fault becomes unclear, based on the supposition that the later uplift of ductile part at the Stage II may have made indistinct the topography of the northern part of Takasegawa Fault, which may have behaved as the western limit of the tilting while Stage I. Therefore the extent of RUZ at the Stage II may correspond the "younger" part of the N. Alps with the ages of ~1 Ma, or the distribution of KG (Fig. 3, 7; approximately northern part than Transect B).

On the uplifting mechanism, compressional stress field may have been prevalent at the Stage II (1 Ma), suggested by the rapid uplifting of ductile zone of KG. This compressional stress field may be related with and derived from the transition of the Eurasian–North American plate boundary from central Hokkaido to the eastern margin of the Japan Sea and the ISTL (e.g., Seno 1985). On the other hand, magmatic intrusion to the upper crust may be supposed for the Stage I according to the discussion on the tilting. Shimizu and Itaya (1993) explained the variation in the volcanism in the central Japan, which were dated as 5.0 – 0 Ma, by the change of the Philippine Sea Plate motion. Presently, it is difficult to reveal the cause of the magmatism in the N. Alps region at ~ 4 Ma, because of lack of studies. To reveal the origin of the magmatism in the Central Japan then is left for future works.

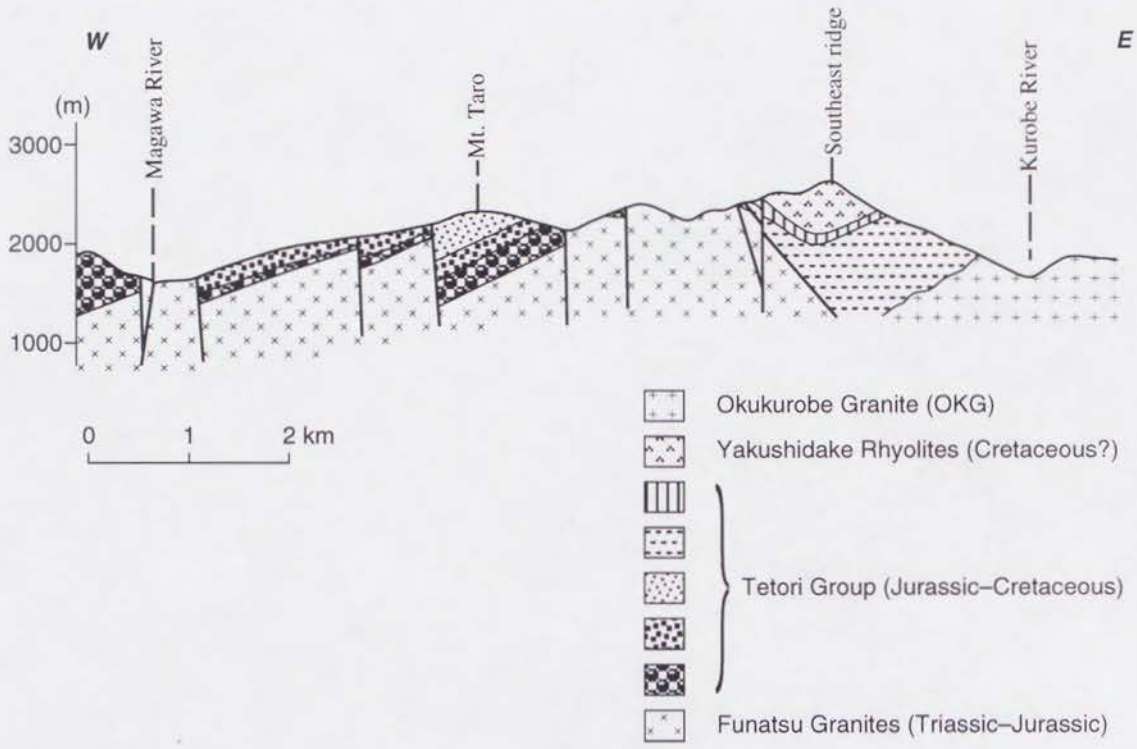

Fig. 21. Geological section map of the Tetori Group which distribute western part of the N. Alps, modified after Harayama et al. (1991). Tilted bedding of the Tetori Group divided and displaced by normal faults indicate the uplifting tilted westward.

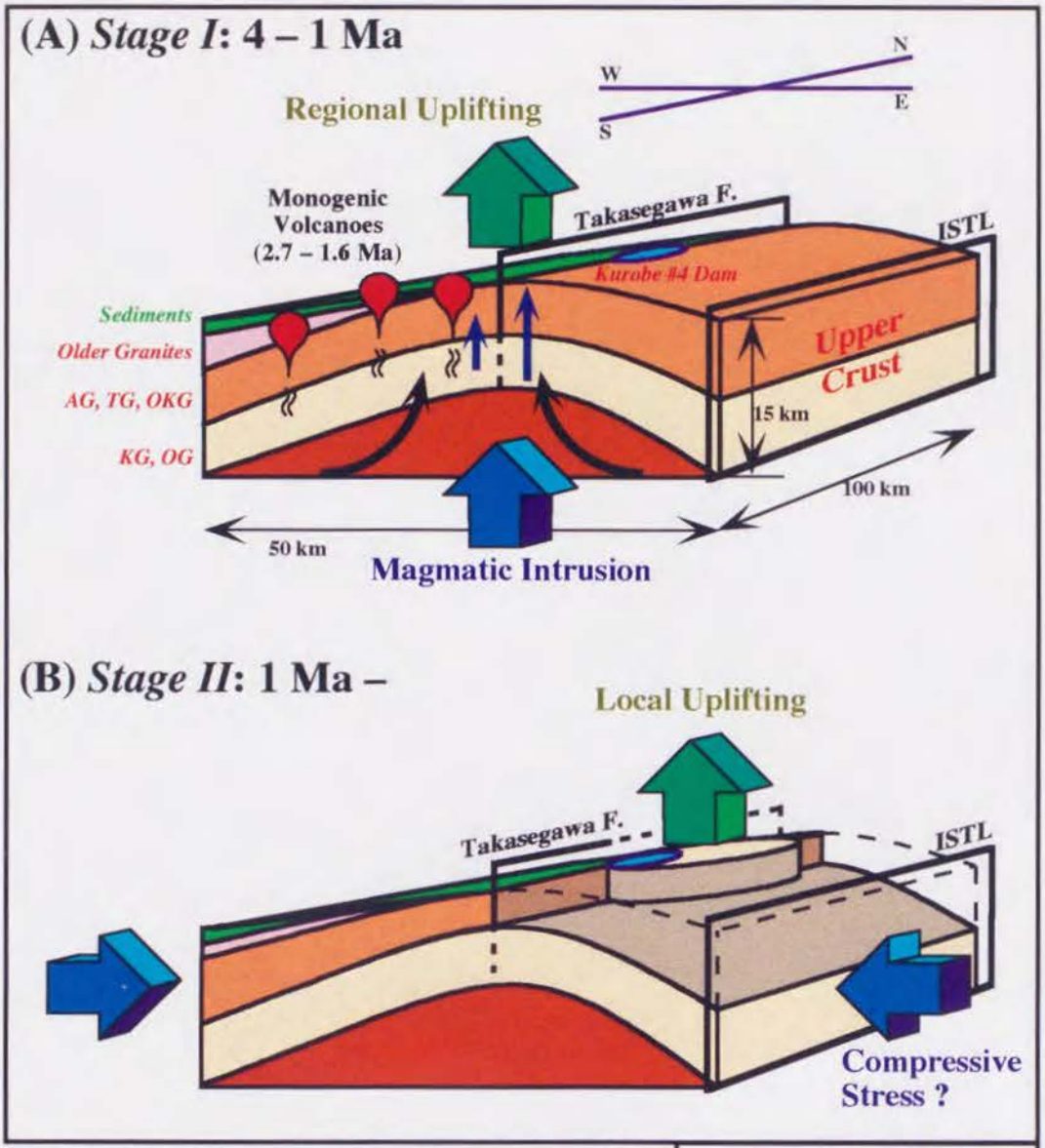

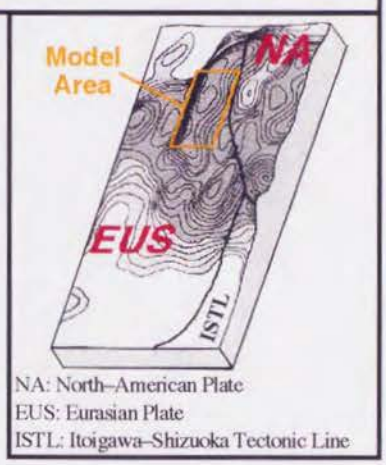

Fig. 22. Schematic model illustratation of the two–stage uplifting of the N. Alps. Model area is indicated in the summit level map (by 10 km x 10 km grids) of the lower panel. In the upper panel, the structure of the upper crust is approximated by the layer–shaped sediments and granites. The position of the Kurobe #4 Dam is shown in order to identify the location. The cause of uplift is symbolized with blue allows, and the resultant uplift with green allows. A; Stage I (4 – 1 Ma); the regional uplifting caused by the magmatic intrusion to the bottom of the upper crust with the thickness of ~ 15 km. In this stage, the N–S trending mountain range of the N. Alps uplifted at the different uplift rate with the maximum rate at the northward central axis, which is represented by the "*Takasegawa F.*" in this diagram. The consequent tilting was occurred both east and west side of the central axis. Uplift rates may have been significantly different between both sides of the fault. The activity of monogenic volcanoes from 2.7 – 1.6 Ma (Shimizu and Itaya, 1993) in the southern part of the N. Alps may be concordant with the *local* tensile stress field in the *shallow* level caused by the domal uplifting in this stage. At the end of this stage, the estimated geothermal gradient at the central area (close to the Kurobe #4 Dam) became relatively high value of 70 °C/km. B; Stage II (1 Ma –); the rapid uplift of relatively local area of the "younger" age granite. As the cause of uplifting in this stage, the compressive stress is assumed to "squeeze" the ductile portion produced by the Stage I uplifting. The compressive stress might have been originated by the transition of the Eurasian–North American plate boundary.

7. Conclusions

For the N. Alps considered to have rapidly uplifted during a couple of million years, thermochronologic study using FT method could reveal the cooling history of rock bodies and the uplift history of the mountain range as follows:

(1) FT age distribution of granitic rocks in the N. Alps is clearly divided into "younger" (< 10 Ma) and "older" (> 50 Ma) group in the N. Alps region. This distribution almost correspond to the distribution of "younger" and "older" rock bodies geologically recognized previously.

(2) Some samples of KG, which have been considered to have intruded at 4–5 Ma (e.g., Harayama et al., 1991), have zircon FT ages > 6 Ma and the track length distributions with shorter length component. This fact indicates that the intrusion timing of the KG should be significantly older than 7 Ma, probably than 10 Ma.

(3) The systematical variation of apparent zircon FT age and mean track length has been recognized according to the sampling altitude along a deep gorge of the Sen–nin Dani. Conductive heat transfer is implied to associate with the rapid uplifting of relatively narrow zone with the width of ~10 km at ~1 Ma.

(4) Paleotemperatures of the samples at the beginning of uplift is assessed based on the resultant relationship between apparent age and mean track length. The vertical geothermal gradient at the beginning of uplifting, which has been estimated by the correspondence of ZPAZ and sampling altitude, is estimated significantly higher (70 °C/km or 110 °C/km) than that of surrounding area at present (40 °C/km).

(5) Samples along Transect C show the systematical variation of track length histogram pattern and apparent zircon FT age (4.2–1.6 Ma) in westward trend. This result implies the eastward tilted uplift during 4–1 Ma.

(6) High geothermal gradient at 1 Ma suggests the precedent uplift of whole region of the N. Alps. The timing of the beginning of this stage can be estimated according to that of the eastward tilting at Transect C.

(7) Two stages of uplift were distinguished in terms of the timing and uplifted area, according to the cooling histories revealed in this study, together with the previous studies, as follows:

Stage I: uplift of the whole region of the N. Alps already started 4 Ma, lasted until 1 Ma. Magmatic intrusion might have accompanied this stage to increase geothermal gradient from 40 °C/km to 70 or 110 °C/km. This stage of uplifting may be characterized as domal uplift according to the eastward tilting in the eastern part and geologically recognized westward tilting

in the western part. The domal uplift may have been accompanied with the magmatic intrusion.

Stage II: uplift of relatively narrow zone, central part of the N. Alps, started and completed at ~1 Ma. According to the estimates of paleodepth of ZPAZ, mean uplift rate during 1 m.y. is assessed as 2–4 mm/y. The rate > 4 mm/y may be expected in order to achieve the present mean altitude of the mountain range of ~2000 m.

(8) On the uplift mechanism of the Stage I, magmatic intrusion to the upper crust (e.g., Ikeda, 1990) can be supported by the inference of domal uplift accompanied with a heat source for the Stage I. On the other hand, the Stage II uplift of ductile zone of KG may have caused by horizontal compression of plate tectonic origin.

Appendix

A. Thermal History Modeling of FT Data

A.1. Forward modeling

Annealing models describing track length reduction can be generalized as

$$l(t) = \mathbf{f}(l_0, T(t)) \qquad \text{Eq. (I–1)}$$

where $l(t)$ is the predicted mean etchable length of a track formed at time t, l_0 is the initial unannealed mean length of the track and, $T(t)$ is the thermal history experienced by that track. It is useful to define the preservation function as

$$r(t) = \frac{l(t)}{l_0} \qquad \text{Eq. (I–2)}$$

where $r(t)$ describes the normalized track reduction, and should vary between 1 and 0. The spontaneous track density per unit area for no annealing (ρ_0) is approximated by

$$\rho_0 = g \cdot l_0 \cdot {}^{238}U \cdot \lambda_f \cdot \int_{-t}^{0} \exp(-\lambda_d \cdot \tau) d\tau \qquad \text{Eq. (I–3)}$$

where g is the geometry factor (= 1 for 4π surface), ${}^{238}U$ is the atomic concentration of ^{238}U at time t, λ_f is the spontaneous fission decay constant for ^{238}U, and λ_d is the total decay constant for ^{238}U.

For t < ~500 Ma, Eq. (I–3) can be reduced to the approximation

$$\rho_0 \approx g \cdot l_0 \cdot {}^{238}U \cdot \lambda_f \cdot \int_{-t}^{0} d\tau. \qquad \text{Eq. (I–4)}$$

Eq. (I–4) indicates that spontaneous track density can be considered to increases in proportionate to the elapsed time.

The observed track density (ρ) will be less than ρ_0 as the result of track length reduction due to annealing. According to the experimental studies, the relationship between track length and density reduction is not 1 : 1 (e.g., Green, 1988; Tagami et al., 1990). The relationship between the reduction of track density and that of length should be obtained by approximating the experimental result to a certain functional form. Exponential function was supposed here to pass some specific points of (density reduction ratio: ρ/ρ_0, length reduction ratio: $\bar{l} / l_0$), as

$$\frac{\rho}{\rho_0} = c_1 \exp\left(\frac{\bar{l}}{l_0} - c_2\right) + c_3 \qquad \text{Eq. (I–5)}$$

where $\bar{l}$ is the mean track length, and c_1, c_2 and c_3 are definitive constants for the function. Because the partial annealing zone was defined in terms of normalized track length reduction r

as $0.4 \le r \le 0.95$ by Yamada et al. (1995b), this function is suppose to satisfy the density–length reduction combination of (0, 0.4) and (1, 0.95), with the condition beyond the range as

$$\begin{cases} 0 \le \bar{l}/l_0 < 0.4, & \rho/\rho_0 = 0 \\ 0.95 < \bar{l}/l_0 \le 1, & \rho/\rho_0 = 1 \end{cases}.$$

The constants were obtained by least square fitting to the experimental results of Tagami et al. (1990, Fig. 10) as

$$c_1 = 1.4,\ c_2 = 0.41 \text{ and } c_3 = -1.4. \qquad \text{Eq. (I–6)}$$

A generalized form of Eq. (I–5) can be written as

$$\frac{\rho}{\rho_0} = \mathbf{g}\left[\frac{\bar{l}}{l_0}\right]. \qquad \text{Eq. (I–7)}$$

Expressing this generalized form in terms of the Eq. (I–2) and accounting for the continuous production and subsequent annealing of tracks through time, the observed density is then approximated by

$$\rho \approx g \cdot l_0 \cdot {}^{238}U \cdot \lambda_f \cdot \int_{-t}^{0} \mathbf{g}[r(\tau)]d\tau. \qquad \text{Eq. (I–8)}$$

In terms of this formulation, the fission track age (t_{ft}) can then be written as

$$t_{ft} \approx t_0 \frac{\rho}{\rho_0} = \int_{-t_0}^{0} \mathbf{g}[r(\tau)]d\tau \qquad \text{Eq. (I–9)}$$

where t_0 is the model time considered.

Unannealed track lengths produced by spontaneous fission of ^{238}U in zircon are not constant but are normally distributed about the mean of ~11 μm with a standard deviation of ~0.7 μm (e.g., Hasebe et al., 1994). Length distribution of annealed tracks formed at t can be approximated by the Gaussian density function,

$$Y(l(t)) = \frac{1}{\sigma(t)\sqrt{2\pi}} \exp\left[-\frac{1}{2}\left(\frac{l(t)-\bar{l}}{\sigma(t)}\right)^2\right] \qquad \text{Eq. (I–10)}$$

where $\sigma(t)$ is the standard deviation of track length $l(t)$. The nonconstant standard deviation $\sigma(t)$ increases systematically as mean track length decreases (Yamada et al., 1995a; Fig. 10). The functional form of the relationship between $\sigma(t)$ and $r(t)$ is obtained by least square fitting of their experimental result to an exponential function,

$$\sigma(t) = 2.97 \cdot \exp(-1.62 \cdot r(t)) \qquad \text{Eq. (I–11)}$$

where the correlation coefficient is 0.82. The final track length distribution can be obtained by summing the length distributions at a certain time weighted by the preserved track density. The

yield ($\hat{Y}(L)$) of tracks of a given length (L) can be expressed in terms of the formulation presented here as

$$\hat{Y}(L) \approx \frac{g \cdot l_0 \cdot {}^{238}U \cdot \lambda_f}{\sqrt{2\pi}} \int_{-t_0}^{0} \frac{\mathbf{g}[r(\tau)]}{\sigma(\tau)} \exp\left[-\frac{1}{2}\left(\frac{L - l(\tau)}{\sigma(\tau)}\right)^2\right] d\tau. \qquad \text{Eq. (I–12)}$$

Track length distributions are generally presented in histogram form with a bin size Δl centered about $L_1, \ldots, L_M$; the normalized track length distribution is then given by

$$f_k = \frac{\int_{L_k - \frac{\Delta l}{2}}^{L_k + \frac{\Delta l}{2}} \hat{Y}(L) dL}{\int_{0}^{L_M + \frac{\Delta l}{2}} \hat{Y}(L) dL} \qquad \text{Eq. (I–13)}$$

where f_k is the relative frequency of tracks ($0 \leq f_k \leq 1$) in the kth bin for $k = 1, 2, \ldots, M$.

For any arbitrary thermal history ($T(t)$), the preservation function ($r(t)$) is calculated following the basic methodology described by Duddy et al. (1988) and Green et al., (1989b). A fission track age and track length distribution can be obtained by numerical integration of Eqs. (I–9) and (I–13).

A.2. Random Monte Carlo Method

A hybrid Monte Carlo optimization procedure, called simulated annealing method, was used in order to constrain the range of thermal histories compatible with observed FT data. Two advantages of this methods are that nonlinear inverse problems can be treated in fully nonlinear form, and a good initial guess is not required.

Optimization or inversion by simulated annealing is founded on the Metropolis algorithm (Metropolis et al., 1953). This simple but powerful algorithm is based on an analogy to the Boltzmann probability distribution, $P(E) \propto \exp(-E/kt)$, stating that a system in thermal equilibrium at temperature T has its energy probabilistatistically distribute among all possible energy states E, where k is Boltzmann's constant. Even at low temperature, there is a finite probability of a system being in a high energy state. Metropolis et al. (1953) incorporated these principles into numerical calculations by assuming that a thermodynamic system would change its configuration from energy E_a to energy E_b with probability P given by

$$P(\Delta E) \propto \exp\left[-\frac{E_b - E_a}{kT}\right]. \qquad \text{Eq. (I–14)}$$

For $E_b < E_a$, this probability is arbitrarily set to unity and the system always takes this option. For $E_b > E_a$, the system sometimes takes this option, where the conditional acceptance is implemented by choosing a random number uniformly distributed between 0 and 1. Metropolis algorithm requires a control parameter C_T (analogous to temperature) and an 'annealing schedule' which tells how this parameter is lowered from high to low values.

An arbitrary thermal history is described by segments of linear variation of temperature with time. The segments are specified by a set of temperature–time endpoints for this study (Fig. A–1). Two terminating endpoints are fixed for time and are free for temperature direction, and others are free for both. Therefore, if the thermal history is described by n endpoints, the model parameter (**m**) has $2n$-2 elements. In the random Monte Carlo approach, the variation of model parameters (Δ**m**) are decided by random vector **u** as,

$$\Delta\mathbf{m} = \mathbf{A}\cdot\mathbf{u} \qquad \text{Eq. (I–15)}$$

where **A** is the step distribution matrix. The maximum model time t_0 for a set of FT data can be obtained by the relationship

$$t_0 \approx \left(\frac{l_0}{\bar{l} - \sigma}\right)\cdot t_{ft} \qquad \text{Eq. (I–16)}$$

where $\bar{l}$ is the mean track length, σ is the standard deviation of the distribution, and t_{ft} is the observed fission track age (Corrigan, 1991). For a newly generated model by Eq. (I–15), FT age and length distribution are obtained by forward calculation. The objective function for optimization in the algorithm is the data misfit for a certain model (**m**), obtained as

$$E(\mathbf{m}) = w_1 \cdot E_1(\mathbf{m}) + w_2 \cdot E_2(\mathbf{m}) \qquad \text{Eq. (I–17)}$$

where

$$E_1(\mathbf{m}) = \frac{1}{M' - 1}\left\{\sum_k \frac{\left(N_k^{pred} - N_k^{obs}\right)^2}{N_k^{pred}}\right\} \qquad \text{Eq. (I–18)}$$

$$E_2(\mathbf{m}) = \frac{\left(age^{obs} - age^{pred}\right)^2}{\left(2\sigma_{age}^{obs}\right)^2} \qquad \text{Eq. (I–19)}$$

and w_1 and w_2 are weighting factors. In these Eqs, N_k^{pred} and N_k^{obs} are the number of tracks in kth bin for predicted FT data (by forward calculation), and that for observed, respectively. age^{obs}, age^{pred} and σ_{age}^{obs} are the FT age for predicted FT data, that for observed, and the standard error of the observed age, respectively. $E_1(\mathbf{m})$ is a reduced chi–square (χ_ν^2) value which serves as a logical norm for evaluating the goodness of fit between the observed and predicted track length distributions. M' is the degree of freedom defined by the number of bins that contain measurements ($\neq 0$). $E_2(\mathbf{m})$ is a penalty function that incorporates information about the duration in the track length distribution.

An objective function for a certain model is tested for different two criteria; Test 1: whether this model can yield predicted FT data compatible with observed one; Test 2: whether it is available as a component of pathways to minimize the objective function. For the Test 1, the acceptance is decided by two estimates $E_1(\mathbf{m})$ and $E_2(\mathbf{m})$. $E_1(\mathbf{m}) \leq 2.2$ is a conservative acceptance level for M' degree of freedom (~5). This level corresponds to about a $\geq 5\%$ probability that a random sampling of the predicted distribution would give a χ_ν^2 value equal to or greater than the observed value. $E_2(\mathbf{m}) \leq 1.0$ is a conservative acceptance level for this term. This level corresponds that a predicted age is acceptable if it is within the 2σ uncertainty of the observed age. For the Test 2, a new thermal history defined by some perturbation of the model parameter $\mathbf{m}$ is used to evaluate the change in the objective function

$$\Delta E = E(\mathbf{m} + \Delta\mathbf{m}) - E(\mathbf{m}). \qquad \text{Eq. (I–20)}$$

Rejection or acceptance of the new model is decided by consulting the Metropolis algorithm where ΔE is equated to the change in energy,

$$P(\Delta E) = \exp(-\Delta E / C_T) \qquad \text{Eq. (I–21)}$$

where C_T is a control parameter which is analogous to temperature, which replaces the denominator in the exponential of Eq. (I–14). The 'cooling' schedule of C_T is decided by the difference between the average of objective function for two successive perturbations at a constant value of C_T, and the standard deviation of the objective function.

After a certain number of models are generated at a constant C_T, the perturbations of models passed Test 2 are implemented to reconfigure the step distribution matrix **A** according to the procedure described by Corrigan (1991); the value of C_T is also recalculated at the same time. The goal here is to seek the range of parameters that satisfy the acceptance criterion (Test 1). In terms of this goal, the algorithm is run until a large number (e.g., 200) of acceptable thermal histories are collected for a particular set of data.

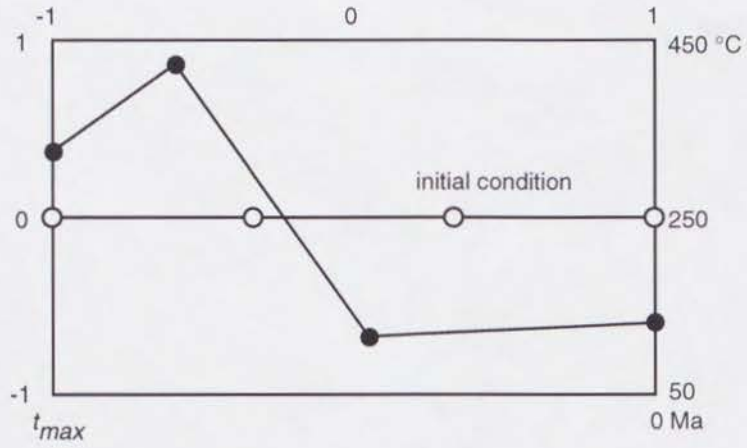

Fig. A–1. Model space configuration for thermal history analysis. An arbitrary thermal history is described by segments of linear variation of temperature with time. The segments are specified by a set of temperature–time endpoints. Two terminating endpoints are fixed for time and are free for temperature direction, and others are free for both. Therefore, if the thermal history is described by n endpoints, the model parameter has $2n$-2 elements. The axis for time is limited between t_{max} and 0 (Ma), and that temperature between 50 and 450 (°C). These range are converted to (-1, 1) for numerical calculation. Initial condition was set at even intervals with a constant temperature of 250°C, as indicated by open circles.

B. One–Dimensional Uplift Modeling

B.1. Methodology

The relationship between a mountain height ($H(t)$) and the erosion rate is empirically known as

$$\frac{\partial h}{\partial t} = -\tau^{-1} \cdot H(t), \qquad \text{Eq. (II–1)}$$

where τ is the erosion time constant, which is the time duration required to reduce the mean height to 1/e (e.g., Ahnert (1970); Pinet and Souriau (1988)). Ikeda (1990) calculated the erosion constant as 0.6 ± 0.4 m.y. for the mountain ranges in the Central Japan, based on the denudation rate data of Yoshikawa (1974) and Ohmori (1978). Given the uplift rate ($u(t)$), the function expressing the variation of a mountain height while uplifting is expressed as

$$\frac{\partial h}{\partial t} = u(t) - \tau^{-1} \cdot H(t). \qquad \text{Eq. (II–2)}$$

Vertical one dimensional heat transfer was assumed to approximate the change in temperature distribution caused by uplifting. The basic equation for one–dimensional heat transfer with uplift is

$$\frac{\partial T}{\partial t} = \alpha \cdot \frac{\partial^2 T}{\partial z^2} - u(t) \cdot \frac{\partial T}{\partial z} \qquad \text{Eq. (II–3)}$$

where α is the rock thermal diffusivity. Radioactive heat generation in the interior of granitic rocks are not considered here, because of its little effect to a change in the thermal condition of the system in ~10^6 y order. The model configuration is schematically illustrated in Fig. A–2. For the initial conditions of the model configuration, the stable state is supposed as follows; the initial mountain height $H(t = 0) = 0$, uplift rate = 0, and the geothermal gradient is constant. The boundary conditions for the mountain surface ($z = H(t)$) is the constant temperature (T_s) is assumed at the surface and the higher part than $H(t)$. At the bottom of a model space, two types of the boundary condition are supposed: (I) the geothermal gradient at the bottom decided by temperature distribution of surrounding area and (II) the constant temperature (T_p) within the hot material moving from the bottom. (I) is applied for the case without uplift of the intrusion. In this case, the rock body is simply cooled from the mountain surface. (II) is used for the case while uplifting accompanied by a plutonic intrusion with a constant temperature. In this case, the system is cooled from the surface and simultaneously heated from the bottom by the intrusion. The temperature distribution function ($T(t, z)$), which express the temperature at an arbitrary time and altitude, can be calculated by solving sequentially Eq. (II–3), together with initial and boundary conditions, following a numerical scheme described in the following section.

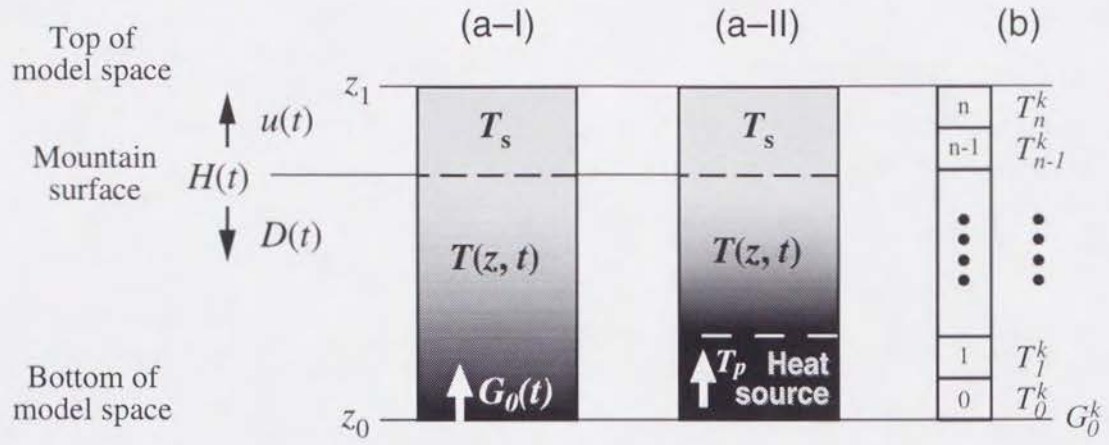

Fig. A–2. (a) A model configuration for one-dimensional heat transfer equation with uplift. The uplift rate $u(t)$ is given as the function of time. The mountain height $H(t)$ is decided by $u(t)$ and denudation rate $D(t)$, which is controlled by erosion time constant τ. In terms of temperature variation, temperature distribution $T(z, t)$ is calculated according to the heat transfer equation with the top boundary conditions of a constant surface temperature T_s, and two types of bottom boundary conditions. One is the geothermal gradient at the bottom $G_0(t)$ is decided by surrounding temperature distribution (a–I), and the other is the constant temperature (T_p) within the heat source rising up from the bottom (a–II). (b) A model configuration modified for numerical solution. The columnar model space of (a) is divided into (n+1) blocks. The temperature distribution function at a time step k (i.e., $t = k \cdot \Delta t$) is expressed as T_i^k, where i: $0 \leq i \leq n$.

B.2. The Numerical Scheme

The columnar model space is divided into (n+1) blocks along vertical direction. The continuous variable $T(t, z)$ is replaced by its discrete counterpart

$$T_i^k = T(k\Delta t, i\Delta z) \qquad \text{Eq. (II–4)}$$

where the subscript i and the superscript k indicate steps for depth and time; Δt and Δz are the time step size and the space increments of the finite difference mesh, respectively. The temperature at higher part than a mountain surface (H) is set to the surface temperature (T_s)

$$T_i^k = T_s \quad \left(i; i_0^k \le i \le n\right) \qquad \text{Eq. (II–5)}$$

where i_0^k is the minimum step of i which satisfies the following relationship at a certain time step k,

$$Z_i \ge H_k. \qquad \text{Eq. (II–6)}$$

The initial temperatures of blocks under the mountain surface are

$$T_i^0 = T_s - G_0 \cdot z_i^0 \qquad \text{Eq. (II–7)}$$

where G_0 is an initial geothermal gradient.

Two types of the boundary condition defined in the text are expressed by mathematical descriptions as follows

(I): $$G_0^{k+1} = G_0^k \qquad \text{Eq. (II–8)}$$

(II): $$T_i^k = T_p \left(i; z_0 \le z_i^k \le z_0 + \sum_{l=0}^{k} u(l \cdot \Delta t) \cdot \Delta t \right), \qquad \text{Eq. (II–9)}$$

where T_p and z_0 are a constant plutonic temperature and the bottom altitude of the upper crust, respectively.

The change in temperature of the bottom block ($i = 0$) between sequential steps is caused by the heat transfer to the block for the case of (II).

The heat transfer equation Eq. (II–3) is approximated by the finite difference equations according to the Crank–Nicolson method as

$$T_i^{k+1} - T_i^k = \frac{r_z}{2}\left\{\left(T_{i+1}^{k+1} - 2 \cdot T_i^{k+1} + T_{i-1}^{k+1}\right) + \left(T_{i+1}^k - 2 \cdot T_i^k + T_{i-1}^k\right)\right\}$$
$$- \frac{\Delta t \cdot u^k}{4 \cdot \Delta z}\left\{\left(T_{i+1}^{k+1} - T_{i-1}^{k+1}\right) + \left(T_{i+1}^k - T_{i-1}^k\right)\right\}$$

Eq. (II–10)

where $i: 1 \le i \le i_0^k$, $u^k = u(k\Delta t)$, and $r_z = \dfrac{\Delta t \cdot \alpha}{(\Delta z)^2}$. This can be arranged in terms of time step as

$$\left(-\frac{r_z}{2} + \frac{\Delta t \cdot u^k}{4 \cdot \Delta z}\right) \cdot T_{i+1}^{k+1} + (1 + r_z) \cdot T_i^{k+1} + \left(-\frac{r_z}{2} - \frac{\Delta t \cdot u^k}{4 \cdot \Delta z}\right) \cdot T_{i-1}^{k+1}$$
$$= -\left(-\frac{r_z}{2} + \frac{\Delta t \cdot u^k}{4 \cdot \Delta z}\right) \cdot T_{i+1}^{k} + (1 - r_z) \cdot T_i^k - \left(-\frac{r_z}{2} - \frac{\Delta t \cdot u^k}{4 \cdot \Delta z}\right) \cdot T_{i-1}^{k}.$$

Eq. (II–11)

This equation can further be simplified as

$$a \cdot T_{i-1}^{k+1} + b \cdot T_i^{k+1} + c \cdot T_{i+1}^{k+1} = (-a) \cdot T_{i-1}^{k} + (b - 2r_z) \cdot T_i^k + (-c) \cdot T_{i+1}^{k},$$

Eq. (II–12)

where

$$a = -\frac{r_z}{2} - \frac{\Delta t \cdot u^k}{4 \cdot \Delta z},\ b = 1 - r_z,\ c = -\frac{r_z}{2} + \frac{\Delta t \cdot u^k}{4 \cdot \Delta z}.$$ Eq. (II–13)

When calculating temperature distribution function at (k+1) step by Eq. (II–12), that of previous step (k) is known. Therefore Eq. (II–12) can be expressed using a tridiagonal matrix **P** as **P**·**x** = **y**, where vector **x** and **y** contain unknown parameters (T_i^{k+1}) and known ones of right–hand side of Eq. (II–12), respectively. Model parameters used here, including variables and constants for setting the model configuration, are summarized in Table A–1.

Table A–1. Parameters for Uplift Modeling

symbol	parameter	value	unit
	Variables		
t	time		ky
z	altitude		m
$u(t)$	uplift rate		m/ky
$H(t)$	mountain height		m
$D(t)$	denudation rate		m/ky
$T(z, t)$	temperature distribution		℃
	Constants		
t_0	starting time for calculation	-20000	ky
Δt	time increment size	1	ky
τ	erosion time constant	600	ky
z_0	top of the model space	10000	m
z_1	bottom of the model space	-15000	m
Δz	space increment size	100	m
α	rock thermal diffusivity	1.0^{-6}	m^2/s
T_s	surface temperature	0	℃
T_p	pluton temperature		℃
G_0	initial geothermal gradient		℃/m

Acknowledgment

I wish to express my gratitude to; Drs. T. Tagami, S. Harayama, H. Ito, A. Yamaji, A. Takeuchi, K. Takemura, M. Torii, Y. Furukawa, and Prof. A. Okada for the critical comments on the research; Emer. Prof. S. Nishimura, Prof. T. Matsuda, Dr. N. Hasebe, K. Narita, S. Kanazawa, A. Yamagiwa, and H. Tauchi for the help of sample collection along the extremely steep mountain paths of the N. Alps; Drs. K. Watanabe, H. Nakamura and H. Ohira for providing the occasion to utilize the facilities at the Tandem Accelerator Laboratory of Kyushu University; T. Yoshioka, K. Narita, S. Kanazawa, A. Yamagiwa, Y. Yoshimoto and O. Himeno for the experimental assistance. I greatly appreciate Emer. Prof. S. Nishimura and Dr. T. Tagami, for supervising this research.

Special thanks are due to Kansai Electric Power Co., Inc. for providing permission and convenience for sample collection, and Dr. S. Harayama at Geological Survey of Japan, for providing very important samples and rock type identification. This work has been performed using facilities of the Research Reactor Institute, Kyoto University.

References

Ahnert, F., Functional relationship between denudation, relief, and uplift in large mid–latitude drainage basins, *Am. J. Sci., 268*, 243–263, 1970.

Brown, R.W., M.A. Summerfield, and A.J.W. Gleadow, Apatite fission track analysis: its potential for the estimation of denudation rates and implications for models of long–term landscape development, in *Process models and theoretical geomorphology*, edited by M.J. Kirkby, pp. 23–53, John Wiley and Sons Ltd., 1994.

Carlson, W.D., Mechanisms and kinetics of apatite fission–track annealing, *Am. Mineral., 75*, 1120–1139, 1990.

Corrigan, J., Inversion of apatite fission track data for thermal history information, *J. Geophys. Res., 96*. 10,347–10,360, 1991.

Crowley, K.D., M. Cameron, and R.L. Schaeffer, Experimental studies of annealing of etched fission tracks in fluorapatite, *Geochim. Cosmochim. Acta, 55*, 1449–1465, 1991.

Duddy, I.R., P.F. Green, and G.M. Laslett, Thermal annealing of fission tracks in apatite, 3, Variable temperature behavior, *Chem. Geol., 73*, 25–38, 1988.

Fitzgerald, P.G., M. Sandiford, P.J. Barrett, and A.J.W. Gleadow, Asymmetric extension associated with uplift and subsidence in the Transantarctic Mountains and Ross Embayment, *Earth Planet. Sci. Lett., 81*, 67-78, 1986.

Fujii, S., K. Souma, M. Goto, T. Kamishima, M. Shimizu, K. Kaneko, Y. Kono, T. Ito, Y. Mizutani, K. Hirooka, I. Kawasaki, H. Okumura, A. Takeuchi, and Y. Muramoto, *Geological map of the Toyama Prefecture, Japan*: scale 1:100,000, 1992.

Fukahata, Y., Change in geotherm due to rapid erosion: evolution of thermal structure of subduction zones, MS., 34 pp., Univ. of Tokyo, 1995.

Fukao, Y., and K. Yamaoka, Stress estimate for the highest mountain system in Japan, *Tectonics, 2*, 453–471, 1983.

Furukawa, Y., Temperature structure in the crust of the Japan arc and the thermal effect of subduction, in *Terrestrial heat flow and geothermal energy in Asia*, edited by M.L. Gupta, and M. Yamamoto, 203–219, Oxford & IBH Pub. Co., New Delhi, India, 1995.

Galbraith, R.F., On statistical models for fission track counts, *Math. Geol., 13*, 471–478, 1981.

Gallagher, K., Evolving temperature histories from apatite fission–track data, *Earth Planet. Sci.*

Lett., 136, 421–435, 1995.

Gleadow, A.J.W., and P.G. Fitzgerald, Uplift history and structure of the Transantarctic Mountains: new evidence from fission track dating of basement apatites in the Dry Valleys area, southern Victoria Land, *Earth Planet. Sci. Lett., 82,* 1–14, 1987.

Gleadow, A.J.W., I.R. Duddy, and J.F. Lovering, Fission track analysis: a new tool for the evaluation of thermal histories and hydrocarbon potential, *Aust. Petrol. Explor. Assoc. J., 23,* 93–102, 1983.

Green, P.F., A new look at statistics in fission–track dating, *Nucl. Tracks, 5,* 77–86, 1981.

Green, P.F., Comparison of zeta calibration baselines for apatite, zircon and sphene, *Chem. Geol., 58*, 1–22, 1985.

Green, P.F., On the thermo–tectonic evolution of northern England: evidence from fission track analysis, *Geol. Mag., 123,* 493–506, 1986.

Green, P.F., The relationship between track shortening and fission track age reduction in apatite: combined influences of inherent instability, annealing anisotropy, length bias and system calibration, *Earth Planet. Sci. Lett., 89,* 335–352, 1988.

Green, P.F., I.R. Duddy, A.J.W. Gleadow, and J.F. Lovering, Apatite fission–track analysis as a paleotemperature indicator for hydrocarbon exploration, in *Thermal history of sedimentary basins. Methods and case histories,* edited by N.D. Naeser, and T.H. McCulloh, pp. 181–195, Springer–Verlag, New York, 1989a.

Green, P.F., I.R. Duddy, G.M. Laslett, K.A. Hegarty, A.J.W. Gleadow, and J.F. Lovering, Thermal annealing of fission tracks in apatite, 4, Quantitative modeling techniques and extension to geological timescales, *Chem. Geol., 79*, 155–182, 1989b.

Harayama, S., Youngest exposed granitoid pluton on earth: cooling and rapid uplift of the Pliocene–Quaternary Takidani granodiorite in the Japan Alps, Central Japan, *Geology, 20*, 657–660, 1992.

Harayama, S., M. Takeuchi, S. Nakao, T. Sato, and F. Takizawa, *Geology of the Yarigatake district*. With Geological Sheet Map at 1:50,000, 190 pp., Geol. Surv. Jpn., Tsukuba, 1991.

Hasebe, N., T. Tagami, and S. Nishimura, Towards zircon fission–track thermochronology: reference framework for confined track length measurements, *Chem. Geol., 112*, 169–178, 1994.

Hirabayashi, T., Neogene conglomerates and Cenozoic geohistory of the northern Fossa Magna in Central Japan (Parts I and II), *Earth Science, 4*, 79–92, 115–128, 1970.

Hirahara, K., A. Ikami, M. Ishida, and T. Mikumo, Three–dimensional P–wave velocity structure beneath Central Japan: low–velocity bodies in the wedge portion of the upper mantle above high–velocity subducting plates, *Tectonophysics, 163,* 63–73, 1989.

Hurford, A.J., Cooling and uplift patterns in the Lepontine Alps south central Switzerland and an age of vertical movement on the Insbruc fault line, *Contrib. Mineral. Petrol., 92,* 413–427, 1986.

Hurford, A.J., and P.F. Green, The zeta age calibration of fission–track dating, *Isotope Geosci., 1*, 285–317, 1983.

Hurford, A.J., and R.T. Watkins, Fission-track age of the tuffs of the Buluk Member, Bakate Formation, northern Kenya; a suitable fission-track age standard, *Chem. Geol., 66* , 209–216, 1987.

Ikeda, Y., Erosion and uplift: observational basis for modelling mountain building processes, *Zisin, 43*, 137–152, 1990.

Ito, K., Regional variations of the cutoff depth of seismicity in the crust and their relation to heat flow and large inland–earthquakes, *J. Phys. Earth, 38,* 223–250, 1990.

Ito, H., and K. Tanaka, New radiometric age determination on some granitic rocks in the Japan Alps, 1996 (in preparation).

Kamp, P.J.J., and J. M. Tippett, Dynamics of Pacific plate crust in the South Island (New Zealand) zone of oblique continent–continent convergence, *J. Geophys. Res., 98*, 16,105–16,118, 1993.

Kano, T., Southern extension of the Unazuki belt and the Hida marginal belt in the Kurobegawa area, Central Japan, estimated from the occurrence of xenoliths within granitic bodies, *Mem. Geol. Soc. Jpn, 33,* 11–20, 1989.

Kato, H., and T. Sato, *Geology of Shinanoikeda district.* With Geological Sheet Map at 1:50,000, 93 pp., Geol. Surv. Jpn., Tsukuba, 1983.

Kato, H., T. Sato, K. Mimura, and F. Takizawa, *Geology of the Omachi district.* With Geological Sheet Map at 1:50,000, 111 pp., Geol. Surv. Jpn., Tsukuba, 1989.

Katsumata K., T. Urabe, and M. Mizoue, Evidence for a seismic attenuation anomaly beneath the Hida Mountain Range, Central Honshu, Japan, *Geophys. J. Int., 120,* 237–246, 1995.

Kobayashi, Y., On the initiation of subduction of plates, *Earth Monthly, 5,* 510–514, 1983.

Kono, Y., and N. Furuse, 1:1 million scale gravity anomaly map in and around the Japanese

islands, University of Tokyo Press, 1989.

Lal, D., R.S. Rajan, and A.S. Tamhane, Chemical composition of nuclei of Z>22 in cosmic rays using meteoritic minerals as detectors, *Nature, 221*, 33–37, 1969.

Laslett, G.M., W.S. Kendall, A.J.W. Gleadow, and I.R. Duddy. Bias in measurement of fission–track length distributions. *Nucl. Tracks*, 6:79–85, 1982.

Laslett, G.M., P.F. Green, I.R. Duddy, and A.J.W. Gleadow, Thermal annealing of fission tracks in apatite, 2, A quantitative analysis, *Chem. Geol., 65,* 1–13, 1987.

Lutz, T.M., and G. Omar, An inverse method of modeling thermal histories from fission track data, *Earth Planet. Sci. Lett., 104,* 181–195, 1991.

Matsui, M., and M. Yoshida, On the making high temperature tunnel of New–Kurobe No. 3., *Hatsuden–Suiryoku, 59*, 59–68, 1962.

Metropolis, N., A. Rosenbluth, M. Rosenbluth, A. Teller, and E. Teller, Equation of state calculations by fast computing machines, *J. Chem. Phys., 21,* 1087–1092, 1953.

Moor, M.E., A.J.W., Gleadow, and J.F. Lovering, Thermal evolution of rifted continental margins: new evidence from fission tracks in basement apatites from southeastern Australia, *Earth Planet. Sci. Lett., 78*, 255–270, 1986.

Nakamura, K., Possible nascent trench along the eastern Japanese sea as the convergent boundary between Eurasian and North American plates, *Bull. Earthq. Res. Inst., 58,* 711–722, 1983.

Nishimura, S., and T. Mogi, The interpretation of discordant ages of some granitic bodies, *J. Geotherm. Res. Soc. Jpn., 8,* 145–164, 1986.

Nishimura, S., T. Mogi, and K. Katsura, Thermal gradients of deep wells and their terrestrial heat flows in Central and Southwest Japan, *J. Geotherm. Res. Soc. Jpn., 8*, 347–360, 1986.

Ohmori, H., Mean Quaternary uplift rates in the Central Japanese mountains estimated by means of geomorphological analysis, *Bull. Dept. Geogr., Univ. Tokyo*, 10, 31–85, 1978.

Pinet, P., and M. Souriau, Continental erosion and large scale relief, *Tectonics, 7,* 563–582, 1988.

Seno, T., "Northern Honshu microplate" hypothesis and tectonics in the surrounding region, —when did the plate boundary jump from Central Hokkaido to the eastern margin of the Japan Sea?, *J. Geod. Soc. Jpn, 31,* 106–123, 1985.

Shimizu, S., and T. Itaya, Plio–Pleistocene arc magmatism controlled by two overlapping subducted plates, Central Japan, *Tectonophysics, 225*, 139–154, 1993.

Stüwe, K., L. White, and R. Brown, The influence of eroding topography on steady–state isotherms. application to fission track analysis, *Earth Planet. Sci. Lett., 124,* 63–74, 1994.

Tagami, T., Determination of zeta calibration constant for fission track dating, *Nucl. Tracks Radiat. Meas., 13,* 127–130, 1987.

Tagami, T., and C. Shimada, Natural long–term annealing of the zircon fission track system around a granitic pluton, *J. Geophys. Res., 101*, 8245–8255, 1996.

Tagami, T., N. Lal, R.B. Sorkhabi, H. Ito, and S. Nishimura, Fission track dating using external detector method: A laboratory procedure, *Mem. Fac. Sci. Kyoto Univ., 53*, 14–30, 1988.

Tagami, T., H. Ito, and S. Nishimura, Thermal annealing characteristics of spontaneous fission tracks in zircon, *Chem. Geol., 80,* 159–169, 1990.

Tanaka, S., and H. Kagami, Rb–Sr isotopic ages of the granitic rocks in the Tsurugidake–Kekachiyama area, northern Japan Alps, *J. Geol. Soc. Jpn, 93*, 929–932, 1987.

Uchiumi, S., S. Harayama, and K. Uto, K–Ar dating on age–unknown rocks in the 1:200,000 quadrangle, Toyama, *Bull. Geol. Surv. Jpn, 46,* 375–381, 1995.

Wada, H., T. Mikumo, and M. Koizumi, Recent seismic activity in the northern Hida, Toyama Bay and Noto peninsula regions, Annuals, *Disas. Prev. Res. Inst., Kyoto Univ., 33*, 57–74, 1990.

Wada, H., K. Ito, and M. Koizumi, Seismic activity in the Hida Mountain range: the 1993 earthquake swarm near Mt. Yarigatake, Annuals, *Disas. Prev. Res. Inst., Kyoto Univ., 37,* 365–380, 1994.

Wagner, G.A., Apatite fission-track dating of the crystalline basement of middle Europe; concepts and results, *Nucl. Tracks Radiat. Meas., 17*, 277–282, 1990.

Wagner, G.A., and P. Van den haute, *Fission–Track Dating,* 285 pp., Kluwer Acad., 1992.

Yamada, N., T. Nozawa, S. Harayama, F. Takizawa, and H. Kato, 1:200,000 Geological Map of Takayama,. Geol. Surv. Jpn., Tsukuba, 1988.

Yamada, R., Random Monte–Carlo simulation for quantitative modeling of thermal history using fission track data, *Fission Track News Lett., 9,* 1–12, 1996.

Yamada, R., T. Tagami, and S. Nishimura, Assessment of overetching factor for confined

fission track length measurement in zircon, *Chem. Geol., 104*, 251–259, 1993.

Yamada, R., T. Tagami, and S. Nishimura, Confined fission–track length measurement of zircon: assessment of factors affecting the paleotemperature estimate, *Chem. Geol., 119,* 293–306, 1995a.

Yamada, R., T. Tagami, S. Nishimura, and H. Ito, Annealing kinetics of fission tracks in zircon: an experimental study, *Chem. Geol., 122*, 249–258, 1995b.

Yamada, R., T. Yoshioka, K. Watanabe, T. Tagami, H. Nakamura, T. Hashimoto, and S. Nishimura, Experimental techniques to enhance the detection efficiency of confined fission tracks in zircon, *Chem. Geol.* (Submitted).

Yamamoto, A., K. Nozaki, Y. Fukao, M. Furumoto, R. Shichi, and T. Ezaka, Gravity survey in the central ranges, Honshu, Japan, *J. Phys. Earth, 30*, 201–243, 1982.

Yoshikawa, T., Denudation and tectonic movement in contemporary Japan, *Bull. Dept. Geogr., Univ. Tokyo, 6*, 1–14, 1974.

Yuhara, K., Heat discharge from the Kurobe–Sennindani dry hot rock, Toyama prefecture, Japan, *Bull. Geol. Surv. Jpn, 32,* 227–239, 1981.

Zeitler, P.K., Cooling history of the NW Himalaya, Pakistan, *Tectonics, 4*, 127–151, 1985.